

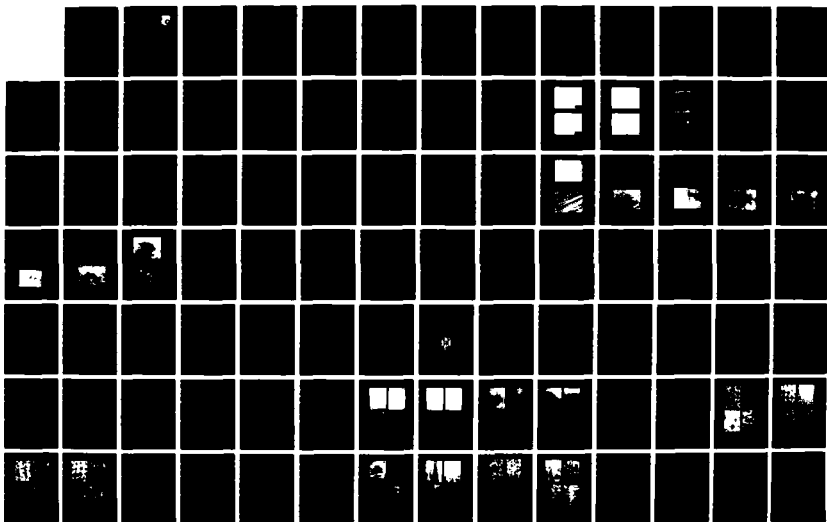
AD-A193 200

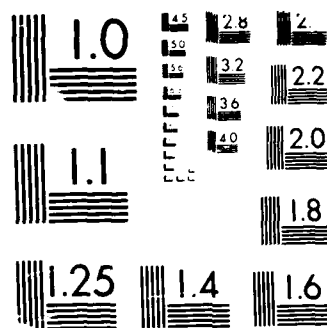
EFFECTS OF HAFNIUM ADDITIONS ON THE SOLIDIFICATION
BEHAVIOR OF DIRECTIONAL. (U) PITTSBURGH UNIV PA DEPT OF
METALLURGICAL AND MATERIALS ENGINE. H D BRODY ET AL.
OCT 81 SETEC-MME-81-043 AFMAL-TR-81-4123 F/G 11/6.2

1/2

UNCLASSIFIED

NL





MICROCOPY RESOLUTION TEST CHART

1963-A (ANSI Z39.48-1968)

AD-A193 288

DTIC FILE COPY

2

AFWAL-TR-81-4123



EFFECT OF HAFNIUM ADDITIONS ON THE SOLIDIFICATION BEHAVIOR OF
DIRECTIONALLY SOLIDIFIED SUPERALLOYS

Melting and Solidification Laboratory
Metallurgical and Materials Engineering
University of Pittsburgh
Pittsburgh, Pennsylvania 15261

October 1981

Final Report for Period 1 June 1975 - 31 August 1977

Approved for public release; distribution unlimited

DTIC
ELECTE
APR 01 1988
S H D

MATERIALS LABORATORY
AIR FORCE WRIGHT AERONAUTICAL LABORATORIES
AIR FORCE SYSTEMS COMMAND
WRIGHT-PATTERSON AIR FORCE BASE, OHIO 45433-6533

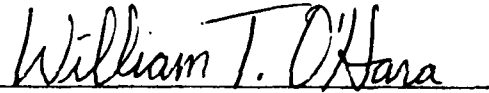
88 1 1 03 9

NOTICE

When Government drawings, specifications, or other data are used for any purpose other than in connection with a definitely related Government procurement operation, the United States Government thereby incurs no responsibility nor any obligation whatsoever; and the fact that the government may have formulated, furnished, or in any way supplied the said drawings, specifications, or other data, is not to be regarded by implication or otherwise as in any manner licensing the holder or any other person or corporation, or conveying any rights or permission to manufacture use, or sell any patented invention that may in any way be related thereto.

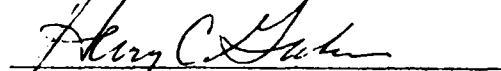
This report has been reviewed by the Office of Public Affairs (ASD/PA) and is releasable to the National Technical Information Service (NTIS). At NTIS, it will be available to the general public, including foreign nations.

This technical report has been review and is approved for publication.



WILLIAM T. O'HARA
Project Engineer

FOR THE COMMANDER



HENRY C. GRAHAM, Chief
Processing & High Temperature
Materials Branch
Metals & Ceramics Division

If your address has changed, if you wish to be removed from our mailing list, or if the addressee is no longer employed by your organization please notify AFWAL/MLLM, W-PAFB, OH 45433 to help us maintain a current mailing list.

Copies of this report should not be returned unless return is required by security considerations, contractual obligations, or notice on a specific document.

UNCLASSIFIED

SECURITY CLASSIFICATION OF THIS PAGE (When Data Entered)

REPORT DOCUMENTATION PAGE		READ INSTRUCTIONS BEFORE COMPLETING FORM
1. REPORT NUMBER AFWAL-TR-81-4123	2. GOVT ACCESSION NO.	3. RECIPIENT'S CATALOG NUMBER
4. TITLE (and Subtitle) EFFECT OF HAFNIUM ADDITIONS ON THE SOLIDIFICATION BEHAVIOR OF DIRECTIONALLY SOLIDIFIED SUPERALLOYS		5. TYPE OF REPORT & PERIOD COVERED Final Report 01 JUN 75 to 31 AUG 77
7. AUTHOR(s) Harold D. Brody and Anthony F. Giamei		6. PERFORMING ORG. REPORT NUMBER SETEC-MME-81-043
9. PERFORMING ORGANIZATION NAME AND ADDRESS University of Pittsburgh School of Engineering Pittsburgh, Pennsylvania 15261		8. CONTRACT OR GRANT NUMBER(s) F33615-75-C-5204
11. CONTROLLING OFFICE NAME AND ADDRESS Air Force Wright Aeronautical Laboratories Materials Laboratory (AFWAL/MLLM) Wright-Patterson AFB, Ohio 45433		10. PROGRAM ELEMENT, PROJECT, TASK AREA & WORK UNIT NUMBERS 61102F 2306P403
14. MONITORING AGENCY NAME & ADDRESS (if different from Controlling Office)		12. REPORT DATE October 1981
		13. NUMBER OF PAGES 175
		15. SECURITY CLASS. (of this report) Unclassified
		15a. DECLASSIFICATION/DOWNGRADING SCHEDULE
16. DISTRIBUTION STATEMENT (of this report) Approved for public release; distribution unlimited		
17. DISTRIBUTION STATEMENT (of the abstract entered in Block 20, if different from Report)		
18. SUPPLEMENTARY NOTES		
19. KEY WORDS (Continue on reverse side if necessary and identify by block number) Solidification, Vacuum metallurgy, Directional solidification, Macrosegregation, Hafnium, Investment casting, Microsegregation, Dendrite spacing, Process models, Nickel base alloys, Superalloys, Chill casting, Cast structure		
20. ABSTRACT (Continue on reverse side if necessary and identify by block number) A cooperative university/industry research program into the effect of hafnium additions on the solidification behavior of nickel base superalloys has been carried out under Air Force sponsorship at the University of Pittsburgh and Pratt and Whitney Aircraft Company. The research was aimed at gaining a fundamental understanding of the basic solidification characteristics, i.e., development of structure and segregation, of hafnium modified MAR-M200 over the normal range of casting conditions and for a reasonable variation in alloy content, especially hafnium content. Cooling rate sensitivity and macrosegregation were		

UNCLASSIFIED

SECURITY CLASSIFICATION OF THIS PAGE(When Data Entered)

investigated as suspected explanations for the microstructural variability in parts directionally cast from this type of alloy. In addition to a program of controlled laboratory experimentation, the as-cast microstructures of typical airfoil castings were assessed. The program was divided into five major tasks: (1) determination of basic alloy parameters, (2) controlled unidirectional solidification to study the individual and combined effects of casting parameters, (3) high cooling rate casting, (4) macrosegregation studies, and (5) continual correlation of provisional analyses with production results.

UNCLASSIFIED

SECURITY CLASSIFICATION OF THIS PAGE(When Data Entered)

FOREWARD

This Final Report covers all work performed under Contract F33615-75-C-5204 by the University of Pittsburgh from 1 June 1975 to 31 August 1977.

This contract was initiated under Project 2306, "Structure and Properties of Solids", Task 2306P4, "Correlation of Structure and Properties", Work Unit 2306P403. The work was monitored by William T. O'Hara of the Metals and Ceramics Division, Materials Laboratory, Air Force Wright Aeronautical Laboratories, Wright-Patterson Air Force Base, Ohio.

Dr. Harold D. Brody of the University of Pittsburgh and Dr. Anothony F. Giamei of the Pratt and Whitney Aircraft Group, United Technologies Corporation, served as principal investigators. Dr. Brody was assisted by S. Chandrasekaran, R. Sellamuthu and J. Gasper. Dr. Giamei was assisted by Walter F. Gustafson and Robert F. Doiron.



Accession For	
NTIS GRA&I	<input checked="checked" type="checkbox"/>
DTIC TAB	<input type="checkbox"/>
Unannounced	<input type="checkbox"/>
Justification	
By	
Distribution/	
Availability Codes	
Dist	Avail and/or Special
A-1	

TABLE OF CONTENTS

	Page
1.0 INTRODUCTION	1
1.1 Problem Definition	1
1.2 Overall Approach	3
1.3 General Background	3
1.4 References	11
Table	13
Figures	14
2.0 TASK I: BASIC ALLOY PARAMETERS	19
2.1 Purpose	19
2.2 Experimental Approach	19
2.3 Solidification Curves	21
2.4 Microsegregation	22
2.5 Dendrite Morphology	23
2.6 Carbides	23
2.7 Eutectic	23
2.8 References	24
Table	25
Figures	26
3.0 TASK II: CONTROLLED UNIDIRECTIONAL SOLIDIFICATION	43
3.1 Introduction	43
3.2 Experimental Procedure	43
3.3 Experimental Results	47
3.4 Discussion	50
Tables	52
Figures	56
4.0 TASK III: THIN PLATE CASTING	97
4.1 Purpose	97
4.2 Experimental Procedure	97
4.3 Results	99
4.4 Summary	99
4.5 References	99
Tables	100
Figures	103
5.0 TASK IV: MACROSEGREGATION STUDIES	109
5.1 Background and Approach	109
5.2 Experimental Procedure	109
5.3 Results	110
5.4 Summary	111
5.5 References	111
Figures	112

6.0	TASK V: CORRLEATION OF ANALYSES WITH ENGINEERING RESULTS .	125
6.1	Purpose	125
6.2	Approach	125
6.3	Results	125
6.4	Discussion	127
6.5	References	127
	Tables	128
	Figures	131
7.0	GENERAL DISCUSSION AND RECOMMENDATIONS	149
7.1	General	149
7.2	Processing - Microstructure Relations	150
7.3	Recommendations	154
7.4	References	155
	Table	156
	Figures	157

1.0 INTRODUCTION

1.1 Problem Definition

The class of materials generally known as nickel-base superalloys is extensively used in modern gas turbine engines. Advanced Ni-base superalloys are generally used in the high turbine portion of the engine and can be used for rotating or static hardware. These alloys contain a high volume fraction of the precipitation hardening γ' phase and are used frequently as castings due to the lack of workability and the need for complex internal cooling configurations. The ever increasing need for components with increased resistance to grain boundary cavitation and thermal fatigue led to the development of the directional solidification process for air foil shapes(1,2). This process results in long columnar grains with the cube axes of the individual grains essentially parallel to the long axis of a rotating part, which is the direction along with the centrifugal stress and the maximum thermal stress are normally encountered. The low elastic modulus in the cube direction results in lower thermal stresses for a given imposed thermal strain and therefore longer lives(3).

One alloy particularly well suited for the directional solidification process is Mar-M200.* Directionally solidified Mar-M200 is not without its problems, however. The alloy has inherently low transverse ductility in tension and in creep rupture at low to intermediate temperatures. Furthermore, as increasingly complex part design began to appear in the late sixties, the cooling passageways in blades became so complex that two types of intergranular failure started to occur with increasing frequency. The first type was in the form of longitudinal cracks in the original castings. This could have been classic hot tearings or possibly a failure which occurred on cooling through intermediate temperatures as the differential thermal expansion between metal and ceramic core developed large hoop stresses in the superalloy. The second type occurred during initial application and was attributable to substantially larger transverse stresses than were present in blades with simpler cooling schemes.

At that point Hf additions to superalloys were introduced. It was shown that substantial increases in transverse stress rupture life could be obtained at intermediate temperatures in columnar-grained superalloys(4). The dependence of 760°C creep elongation to Hf content is illustrated in Figure 1.1. The level of 2 wt% can be considered a nominal target and is obtained by making a late addition to a Mar-M200 melt. The typical effect of the Hf addition on microstructure is shown in Figure 1.2.

The critically needed solution to the ductility problem led to a group of irritating problems related to the high reactivity of Hf. These included shortened melt crucible life, increased rates of metal/mold and metal/core reaction, higher incidence of dross (inclusions),

* Mar-M200: 12.5W-10Co-9Cr-5Al-2Ti-1Nb-0.15C-0.05Zr-0.015B-bal. Ni

and difficulties with final composition control. The high rate solidification process using radiation cooling minimized many of these problems arising from hafnium's reactivity(5). Hf was also an expensive alloying addition, but the price per kg has been minimized (1) by defining the least expensive grade of material which will produce the desired increase in ductility and (2) by more effective utilization of Hf-producing facilities. Additionally, the component cost has been sufficiently large in those parts requiring complex cores and controlled grain structure and the wt% Hf so low that the raw materials cost for the Hf was only a minor consideration.

There was, however, one nagging problem which remained. There was a certain variability in solidification microstructure which could occur, particularly in certain part geometries, and which could lead to undesirable creep properties. An example of the extremes of microstructure which can result at equivalent locations from nominally the same process by the same producer is shown in Figure 1.3. The original addition of Hf nominally increased the amount of eutectic for equivalent solidification conditions, and this was at least partially responsible for the enhancement in intermediate temperature ductility. However, it would appear that there was an uncontrolled variable in the solidification process which led to a variation in the amount of eutectic γ' .

The eutectic microconstituent appears as kidney shaped pools of $\gamma + \gamma'$ containing only thin webs of the disordered γ phase in the as-cast condition. Upon exposure to high temperature, these pools begin to disappear after a few hours by first converting to pure γ' and finally by a gradual dissolution process. The volume percent of eutectic in the cast structure of the base MAR-M200 alloy is normally about 2 to 4%. No substantial variability in the amount of as-cast eutectic microconstituent has been reported as a function of process variations in either laboratory or pilot plant operations. In the case of MAR-M200 + Hf, there is a wide scatter in the observed volume percent eutectic; namely, from 1 to 25%. The range 10 to 15% might be considered normal and could be the basis of the improved properties which have already been discussed. It is anticipated, and there is preliminary data to suggest, that the structures with excessive eutectic, if undetected, will have poor transverse and even longitudinal creep properties. This is due to the lack of creep resistance in single phase γ' . On the other end of the spectrum, the structures with unusually low levels of eutectic might be expected to show unusually good longitudinal creep properties due to an enhancement in homogeneity within the matrix after heat treatment. It has clearly been established that Hf is essentially insoluble in the γ phase and that it is a potent strengthener of γ' . There also may be no significant loss in transverse ductility at the point where only a small amount of eutectic is formed(6). We were, therefore, faced with a double edged dilemma: An incomplete understanding of the segregation dynamics of Hf-modified superalloys prevented either the elimination of undesirable microstructures or the synthesis of new and potentially more useful distributions of alloying elements.

It is possible that a better understanding of the interrelationship between solidification processing and the detailed aspects of segregation will have a bearing on some of the earlier problems which have been

mentioned with respect to Hf bearing superalloys. For example, the ductilization effect which Hf produces in the Ni base superalloys is highly localized phenomenon, i.e. its influence is on the grain boundary regions. It should be possible to obtain structures with equivalent 800°C creep rupture elongation at lower total Hf levels if the distribution of Hf can be more precisely controlled. Also, it is probable that a smaller amount of eutectic microconstituent would lead to lower rates of dross formation and, therefore, fewer dross quality control problems.

It may be important to define the proper Hf level for different applications. For example, there is an increasing tendency for cracking of blade castings with massive internal cores as the metal thickness is decreased, particularly in the absence of Hf. It would seem logical that particularly difficult blade geometries might require more Hf for good castability than parts with lower hoop stresses (which arise due to differential thermal contraction). It would be desirable to keep the Hf in the casting at the lowest useful level, but knowledge is lacking concerning its role in improving castability.

1.2 Overall Approach

The main effort of this program has been carried out with the aim of understanding the basis of microstructural variability in hafnium modified MAR-M200 with emphasis on the two prime suspected causes, cooling rate sensitivity and macrosegregation. To follow this approach the program was divided into five major tasks.

- Task I: Determination of basic alloy parameters
- Task II: Controlled unidirectional solidification to study the effect of individual parameters and controlled transients
- Task III: Thin plate casting to determine the effect of high cooling rates
- Task IV: Macrosegregation studies that will evaluate transients in fluid flow due to shrinkage and convection
- Task V: Continual correlation of provisional analyses with production results.

The procedure and results of each of these tasks are described in Chapters 2-5. The chemical analyses of master alloys used in Tasks I-IV are listed in Table 1.1. The more important results are summarized in Chapter 7. The remainder of this chapter is devoted to a review of solidification principles relevant to this study.

1.3 General Background

In the study of the behavior of alloys in solidification processes, the important interrelated parameters are

casting parameters

basic alloy properties

structure

segregation

These four aspects of solidification are totally interwoven. There is not a single cause-effect chain of events. However, as a first approximation that allows us to get started on a complex problem, we may assume that casting parameters and basic alloy properties (primarily phase relations) are the independent variables and that structure and segregation are determined by the first two. Further, we may assume that within the range of casting conditions wherein the mode of solidification is dendritic, the distribution and spacing of segregation are determined by the dendrite structure. Once this first chain of events is understood, it becomes profitable to map in detail the complex effects of structure and segregation on casting parameters and alloy behavior.

1.3.1. Casting Parameters

For directional solidification processes, the casting parameters of prime interest are

thermal gradients, G ($^{\circ}\text{C}/\text{cm}$)

rates of isotherm advance, R (cm/sec)

cooling rates, ϵ ($^{\circ}\text{C}/\text{sec}$)

transients in the above

geometry

convection

These parameters are of importance as they apply to a particular location in the casting at a given time or for a steady state condition as they apply to a particular isotherm. In many casting situations, G , R and T are coupled, i.e. they cannot be controlled independently. In the more advanced directional solidification processes G and R can be controlled independently. It is important to note first that some solidification phenomena depend primarily on G , some on R , and some on ϵ . Further, keeping in mind the definitions of G , R , and ϵ

$$G = \left. \frac{\partial T}{\partial X} \right|_{T,t} \quad R = \left. \frac{\partial X}{\partial t} \right|_{T,t} \quad \epsilon = \left. \frac{\partial T}{\partial t} \right|_{X,t} \quad (1-1)$$

one may compute ϵ as the product of G and R for steady state conditions

$$\epsilon = G \cdot R \quad (1-2)$$

The local solidification time is defined as the time for a given location in the casting to pass through the freezing range, i.e. the time to cool from liquidus to effective solidus temperature. For constant conditions the local solidification time is given by:

$$t_f = \frac{\Delta T_f}{R \cdot G} = \frac{T_L - T_S}{\epsilon} \quad (1-3)$$

The freezing range, ΔT_f , is the temperature difference between the liquidus temperature, T_L , and the effective solidus temperature, T_S , i.e. the temperature when freezing is actually completed under the local solidification conditions. Transients in the heat flow situation or variations in shape and/or cross section of the mold change the parameters G , R , and ϵ and also are important as they change fluid flow conditions within the mold. Fluid flow of interest is bulk flow of solute enriched liquid through the mushy zone as a result of solidification shrinkage and convection. Convection may be externally generated as by pouring turbulence or vibration or may be generated internally by radial and inverted temperature gradients or by solute gradients.

1.3.2. Investment Casting Techniques for Superalloys

The directional solidification of superalloys has been accomplished in practice by several techniques. The two commercial processes that have been dominant, power down and withdrawal, are shown schematically in Figure 1.4. The thermal gradient during power down has been measured to vary from 15 to 3°C/cm at distances of from 5 to 20 cm. from the chill, respectively. The thermal gradient at the 10 cm level is 10°C/cm. The growth rates normally employed are 8 to 12 cm/hr. In the case of withdrawal (high rate solidification) there is less variation in growth conditions with distance from the chill plate. At the 10 cm level, the thermal gradient would normally be about 40°C/cm with growth rates of 20 to 30 cm/hr.

Perhaps the most versatile directional solidification technique with respect to thermal control is the liquid metal cooling (LMC) process. Figure 1.5 compares the thermal gradients achieved in the three processes. Note the high thermal gradient of the liquid metal cooling process and the ability of the process to maintain a relatively constant thermal gradient over the widest range of growth rates.

1.3.3. Basic Alloy Parameters

The basic alloy parameters of most interest to the type of study pursued herein are the partition ratios for each component ($k_i = C_{Si}/C_{Li}$, the ratio of the solid and liquid compositions in equilibrium at a

particular temperature), the temperatures at which phases should begin to freeze and finish freezing, the difficulty in nucleating various phases, the interfacial energies between solid and liquid phases, and the diffusion coefficients of alloy elements in the solid phases. For complex, multicomponent systems such as the nickel base superalloys (Mar-M200 modified by hafnium has ten components), it is unlikely we could find values for all of these parameters for each of the components and at all of the temperatures of interest. Fortunately, a properly annotated solidification curve provides sufficient information for most analyses of the solidification of complex alloys. The solidification curve is a plot of temperature versus fraction solidified in the freezing range. The curve should be labeled to show the temperatures for first appearance (and disappearance) of the various phases and the compositions of the phases. The solidification curve can be determined by a combination of thermal, metallographic, and microprobe data(7-10).

1.3.4. Dendrite Morphology

There are several elements of structure in cast alloys that are readily observable in metallographic examination and that play an important part in determining the behavior of a cast material in further processing operations and in service. An attempt is not made herein to present a comprehensive list. The primary areas of concern to the current problem are dendrite morphology, segregation, and secondary particles. Dendrite morphology is discussed in this section and the other two aspects of structure are discussed in the sections that follow.

Dendrites are the most significant element of structure in alloy solidification. Because they determine the interface between solid and liquid during freezing, they strongly influence the spacing and distribution of particles, porosity, and alloy elements in the as-cast structure. Dendrite arms are much more numerous than grains in the casting, often by a factor of three to four orders of magnitude.

The spacing of the dendrite arms for a particular alloy has been shown, repeatedly, to be a function of the local solidification time. The local solidification time is the time between the passing of the liquidus and solidus isotherms at a particular position in the casting. It is inversely related to the local cooling rate, note equation (1-3). Knowledge of the relation between dendrite arm spacing and local solidification time allows determination of local freezing times and cooling rates in castings of complex shape by making metallographic rather than thermal measurements.

The secondary dendrite arm spacing typically depends on local solidification time to a power between 0.3 and 0.5(11-12).

$$d_2 \propto t_f^n \quad \text{where } 0.3 \leq n \leq 0.5 \quad (1-4)$$

The grain structure, columnar or equiaxed, and the grain size are not important factors in determining dendrite arm spacing. Near a chill the dendrites are less branched than in regions that have lower thermal

gradients and lower cooling rates. There is also a tendency for the primary dendrite arm spacings to increase with local solidification time, although with a weaker dependence than the case of secondary arms.

1.3.5. Segregation

Segregation is a sufficiently important aspect of the solidification behavior of cast alloys that it is listed separately notwithstanding its close relation to microstructure. The nonuniform distribution of alloy elements that occurs on the scale of dendrite arm spacing or the grain size is termed microsegregation. This may take the form of coring in the primary phase and/or significant amounts of nonequilibrium constituent. When the nonuniformity occurs over the scale of centimeters, it is termed macrosegregation.

These individual elements of structure and segregation are not necessarily separable in their mode of formation or in their region of occurrence. The various aspects of structure are interrelated. As an example, one result of macrosegregation may be to concentrate inclusion particles and eutectic constituents in certain regions of a casting. As another example, microporosity and nonequilibrium constituent particles often are found to occur together in the last places to freeze, locally, the regions between the dendrite arms of the primary phase.

1.3.5.1 Microsegregation. Measures of microsegregation that may be taken from actual castings include segregation ratio and percent nonequilibrium phase. Segregation ratio, S , is defined as the local maximum in solute content for a particular component divided by the local minimum where the region considered is on the scale of the dendrite arm spacing. A value of 1.0 would indicate a homogeneous alloy, the equilibrium condition for a single phase alloy. The greater the deviation of S from 1, the greater is the degree of microsegregation in a particular alloy. Also, the greater the amount of nonequilibrium phases such as eutectics, the greater is the degree of microsegregation.

Experimental and analytical results on the development of microsegregation in dendritic freezing(8,11-16) indicate that the extent of microsegregation for a given element in an alloy will depend on a factor termed α_i , where

$$\alpha_i = D_{Si}\eta = \frac{D_{Si}t_f}{(d_2/2)^2} \quad (1-5)$$

D_{Si} is the diffusion coefficient for that element in the primary solid phase and η is the ratio of the local solidification time, t_f , to the square of half of the secondary dendrite arm spacing. As cast microsegregation should approach the equilibrium value, $S = 1$, for large values of α_i . The smaller the values of α_i in comparison to one, the

greater will be the segregation ratio and the extent of nonequilibrium phases (up to the limiting case of negligible diffusion in the solid phases).

In equation (1-5) the value of α_1 and, thus, the extent of microsegregation depends neither on the local solidification time nor on the dendrite spacing but rather on their relationship as given by the ratio η . Because dendrite arm spacing and local solidification time are related by equation (1-4), η changes only slowly, if at all, with increases in local solidification time. Thus, it would be expected from the model that extent of microsegregation, at the solidus, would not be much affected by changes in the cooling rate. At the end of freezing, an electron beam weld and a massive ingot would have about the same degree of microsegregation provided the mode of freezing is dendritic for both cases.

Little data on the freezing of nickel base superalloys has been analyzed in light of this model and all the pertinent data have not been collected. In particular, the assumptions inherent in the model have not been checked for nickel base alloys, notably the possible effect of rate of dendrite tip advancement on dendrite tip undercooling and the possible undercooling or repression of solid phases. Further, the experimental data and detailed calculations supporting the theory have been obtained, mainly, from binary alloy systems. As has been pointed out, the alloy system of concern here has ten major components.

1.3.5.2 Macrosegregation. Because the liquid in the mushy zone is enriched in solute, the movement of this liquid from one part of the casting to another can lead to macrosegregation. One source of macrosegregation is the flow of solute enriched liquid to feed solidification shrinkage(17-20). Another source of macrosegregation is convection induced by thermal and/or solute gradients(20-21). Normally, as an alloy freezes the density of solid phases that are forming is less than the density of the liquid from which they form. If a pore is to be precluded, liquid must flow to feed the shrinkage. When the flow of enriched liquid in the mushy zone leads to a net change in composition within the volume element, macrosegregation results. Such is the case whenever there are transients in G , the local thermal gradient; ϵ , the local cooling rate; or v , the local velocity of fluid flow. Changes in v result from thermal conditions but also from changes in cross section. Because superalloys show relatively little shrinkage, macrosegregation as a result of this mechanism has not been considered important. However, the effect of hafnium on the macrosegregation tendencies of superalloys is not known.

It must be kept in mind that the understanding of macrosegregation requires the knowledge of the solute redistribution that occurs on the local scale of the dendrite arm spacing, also, that macrosegregation is manifested in the casting by an alteration of the microsegregation. For example, positive macrosegregation, an enrichment in the last elements to freeze, usually increases the amount of nonequilibrium eutectic. Negative macrosegregation leads to a decrease in the amount of nonequilibrium segregate.

While many generalizations can be made about cast structure and properties, the effect of casting parameters on the structure of a particular alloy and the relation of structure to properties are highly varied and specific to the individual system. Each alloy system and set of casting conditions has to be studied individually. General statements can only be considered as guidelines.

1.3.6. Behavior of MAR-M200

Mar-M200 can be considered as a typical advanced Ni-base superalloy. The liquidus temperature has been reported to be 1415°C. The primary phase field is the γ solid solution. The only other equilibrium phase which forms during solidification is the MC carbide based on the TiC compound with the NaCl structure. Nb, Zr and W substitute liberally for Ti in the carbide and a certain amount of carbide segregation is noted in electron microprobe experiments. These carbides probably form during the last one third of solidification and are entrapped between secondary dendrite arms and along grain boundaries.

The solute distribution coefficients (this term is interchangeable with partition ratio, k_i) for the major alloying elements appear to be less than one with the exception of Co and W, where $k_i > 1$. Elements such as Al, Ti and Nb are rejected by the dendrites and tend to accumulate in the interdendritic regions. Interdendritic enrichment of Cr rarely has been observed, probably due to its relatively high diffusivity. Co and W, on the other hand, are incorporated into the dendrite centers and are present to a lesser extent in the interdendritic material. The W segregation is severe and is very difficult to eliminate in subsequent heat treatment due to the low diffusivity of this refractory element in Ni.

A brief explanation of the source of contrast in the solidification microstructures of $\gamma + \gamma'$ superalloys is illustrative of the solidification process. As soon as solidification is complete, the structure is about 85-95% primary γ phase. Upon further cooling, precipitation of the ordered γ' precipitation hardening phase is initiated. Since the γ phase is inhomogeneous, there is a variation in the γ' solvus temperature throughout the structure. The highest solvus temperature is associated with the Al and Ti rich interdendritic areas. Precipitation of the coherent precipitate begins first in these areas, and particle coarsening proceeds rapidly at the very high temperatures. The interdendritic solvus is traditionally referred to as the solvus temperature and would normally occur at about 1185°C in MAR-M200. At substantially lower temperatures, γ' begins to form in the dendrite centers. The smaller diffusion coefficient, equilibrium volume fraction, and coarsening times in these regions result in finer particles and a slightly lower volume fraction of precipitate near the dendrite centers and result in the differential etching which is normally observed on a polished and etched sample.

At growth rates typical of the directional solidification process there is already a considerable deviation from equilibrium during solidification. This is primarily due to insufficient diffusion in the solid

which is formed early in the solidification process. For all components, except carbon, $\alpha_1 < 1$. This lack of rapid diffusion does not allow for the continual readjustment which is normally required during equilibrium solidification. As a consequence, the dynamic microsegregation amplitude is large, and a small amount of $\gamma + \gamma'$ eutectic can be formed as the last solidification product. This microconstituent is mostly γ' and can be eliminated by a high temperature homogenization heat treatment. The solubility of Cr in γ' is extremely low and therefore γ webs which form between the coarse γ' particles in the eutectic pool are enriched in Cr.

In the case of Mar-M200 the volume fraction of the non-equilibrium eutectic microconstituent does not seem to vary substantially over a wide range of growth conditions, provided all major forms of macrosegregation have been suppressed. This is generally accomplished by maintaining horizontal interfaces during directional growth, and by working with the highest possible thermal gradients. These precautions are required in order to prevent concentration driven convection of the interdendritic fluid which is less dense near the solidus surface than near the liquidus(21). There is normally a tendency for these two liquids to interchange via a localized convection process which leads to severe lateral macrosegregation and moderate axial segregation. The horizontal interfaces and the high gradient simply minimize the energy available to drive this localized convective process. (It would be extremely difficult to prevent this convective action when the interfaces deviate from horizontal and the growth rate is a low to intermediate value.)

Foreign particles in a cast alloy frequently are the result of impurities introduced into the alloy by the melting or casting operation. For example, hafnia inclusions in nickel base superalloys result from reaction of hafnium with the melting crucible, the mold, or the core. Also, as-cast second and third phase dispersions may be purposeful elements of the microstructure intended for property improvement, such as metal carbides (MC) in Mar-M200 and γ' in the eutectic constituent of hafnium modified MAR-M200(4,22). The as-cast second phase particles may be equilibrium or nonequilibrium constituents of the microstructure. Nonequilibrium particles may be dissolved by the proper selection of solution treatment.

Particles often are located in the interdendritic regions, which are the last regions to freeze locally. Very often this is because the particles are the last phases to freeze, for example as a result of a eutectic reaction such as $L \rightarrow \gamma + \gamma'$. However, some particles that form early in the freezing process are pushed into the interdendritic regions by the thickening secondary dendrite arms. Microporosity as the result of shrinkage or evolution of gas dissolved in the liquid forms in the interdendritic regions as well.

Very little documentation exists as to the solidification microstructure of superalloys under extreme growth conditions. It is known that similar structures to those already discussed are normally formed near the chill plate, although they are considerably finer due to the high heat transfer coefficient and resultant cooling rates. It is known that welded superalloys are dendritic and still finer in the scale of

and cellular material had been produced previously at G/R ratios in excess of $300^{\circ}\text{C-hr/cm}^2$. For comparison, the G/R values typical of the power down process would be 1 and for withdrawal we would have about 2 in the same units. An extremely important point is that very little is known about this ratio near the chill surface and this knowledge surely needs expansion.

1.3.7. Influence of Hafnium Additions on Solidification

The addition of Hf to Mar-M200 dramatically changes the solidification microstructure. This element is essentially insoluble in the γ phase under equilibrium conditions and this leads to partitioning at the growth rates and thermal gradients typical of the power-down and withdrawal solidification processes. A single previous measurement of the distribution coefficient of Hf appropriate to the latter stages of solidification indicated that it was only 0.10. This is completely consistent with the low solubility of Hf in the dendrite and with the nature of the ductilization effect which Hf produces. The addition of Hf to Mar-M200 increases the normal volume fraction of eutectic constituent from 2% to about 15%. It is worthwhile to note that for the case of 15 wt% of the eutectic microconstituent, a Hf level of 8 wt% in the eutectic would account for 1.2 wt% Hf in the alloy. Naturally, almost all of the Hf in the eutectic resides in the γ' phase within the pools.

1.4 References

1. F. L. VerSnyder and R. W. Guard, "Directional Grain Structures for High Temperature Strength," Trans. Am. Soc. Metals, 52 (1960) 485-493.
2. F. L. VerSnyder, R. B. Barrow, B. J. Pearcey, and L. W. Sink, Trans. Intl. Vacuum Metal Conf., ed. by E. L. Foster (New York: American Vacuum Society, 1967) 391-411.
3. F. L. VerSnyder and M. E. Shank, "The Development of Columnar Grain and Single Crystal High Temperature Materials Through Directional Solidification," Mater. Sci. Eng., 6, no. 4 (1970) 213-247.
4. D. N. Duhl and C. P. Sullivan, "Some Effects of Hafnium Additions on the Mechanical Properties of a Columnar-Grained Nickel-Base Superalloy," J. of Metals, 23, no. 7 (1971) 38-40.
5. J. S. Erickson, W. A. Owczarski, and P. M. Curran, "Process Speeds Up Directional Solidification," Met. Prog., 99, no. 3 (1971) 58-66.
6. J. E. Doherty, B. H. Kear, A. F. Giamei, and C. W. Steinke, "The Effect of Surface Chemistry on Grain Boundary Strength," Grain Boundaries in Engineering Materials, ed. J. L. Walter and D. A. Woodford, Fourth Bolton Landing Conference (1974).

7. E. E. Stonebrook and W. E. Sicha, "Correlation of Cooling Curve Data with Casting Characteristics of Aluminum Alloys," AFS Trans., 57 (1949) 489-498.
8. T. F. Bower, H. D. Brody, and M. C. Flemings, "Measurement of Solute Redistribution in Dendritic Solidification," Trans. TMS-AIME, 236 (1966) 625-634.
9. R. Schlatter, S. M. Thesis, University of Pittsburgh, 1968.
10. B. U. Z. Igwe, S. M. Thesis, University of Pittsburgh, 1969.
11. B. Chalmers, Principles of Solidification (New York: John Wiley and Sons, 1964).
12. M. C. Flemings, Solidification Processing (New York: McGraw Hill, 1974).
13. L. H. Cadoff, Westinghouse Electric Corporation, R & D Center, Churchill Boro, PA, Manuscript in preparation.
14. H. D. Brody and M. C. Flemings, "Solute Redistribution in Dendritic Solidification," Trans. TMS-AIME, 236 (1966) 615-624.
15. M. C. Flemings, R. V. Barone, D. R. Poirier, and H. D. Brody, "Microsegregation in Iron Base Alloys," JISI, 208 (1970) 371-381.
16. J. I. Nurminen and H. D. Brody, "Dendrite Morphology and Microsegregation in Cast Titanium Alloys," Titanium Science and Technology, ed. R. I. Jaffee and H. M. Burte (New York: Plenum Press, 1973) 1893-1914.
17. G. E. Nereo and M. C. Flemings, "Macrosegregation, Part I," Trans. TMS-AIME, 239 (1967) 1449-1459.
18. G. E. Nereo, R. Mehrabian and M. C. Flemings, "Macrosegregation, Part II," Trans. TMS-AIME, 242 (1968) 41-49.
19. G. E. Nereo and M. C. Flemings, "Macrosegregation, Part III," Trans. TMS-AIME, 242 (1968) 50-55.
20. R. Mehrabian, M. Keane and M. C. Flemings, M.I.T., Technical Report to Office of Naval Research, Contract NONR-3963 (09), November 1969.
21. S. M. Copley, A. F. Giamei, S. M. Johnson and M. G. Hornbecker, "The Origin of Freckles in Unidirectionally Solidified Castings," Met. Trans., 1 (1970) 2193-2204.
22. J. E. Doherty, B. H. Kear, and A. F. Giamei, "On the Origin of the Ductility Enhancement in Hf-doped Mar-M200," J. of Metals, 23, (November, 1971) 59-62.

Table 1.1: Chemical Analyses of Master Ingots

Alloy	Cr	Co	Ti	Al	W	Nb	C	Zr	B	Hf	Ni
Mar-M200	8.08	9.31	1.88	4.85	12.76	1.05	.15	.03	.018	0.0	Balance
Mar-M200 + 1.0% Hf	8.61	11.1	1.93	4.99	11.66	.92	.18	.05	.016	0.86	Balance
Mar-M200 + 2.0% Hf	8.60	9.5	1.95	5.01	11.60	.95	.15	.09	.015	2.10	Balance
Mar-M200 + 2.5% Hf	9.45	10.72	1.95	5.03	11.94	1.03	.14	.09	.018	2.66*	Balance

*X-ray fluorescence

EFFECT OF HAFNIUM ON TRANSVERSE CREEP DUCTILITY OF D. S. MAR-M200

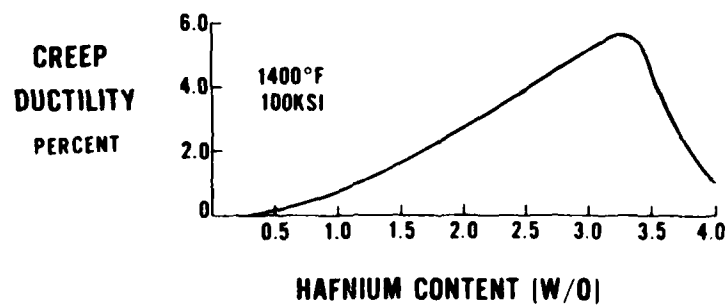


Figure 1.1: Effect of hafnium additions on the creep elongation of Mar-M200.

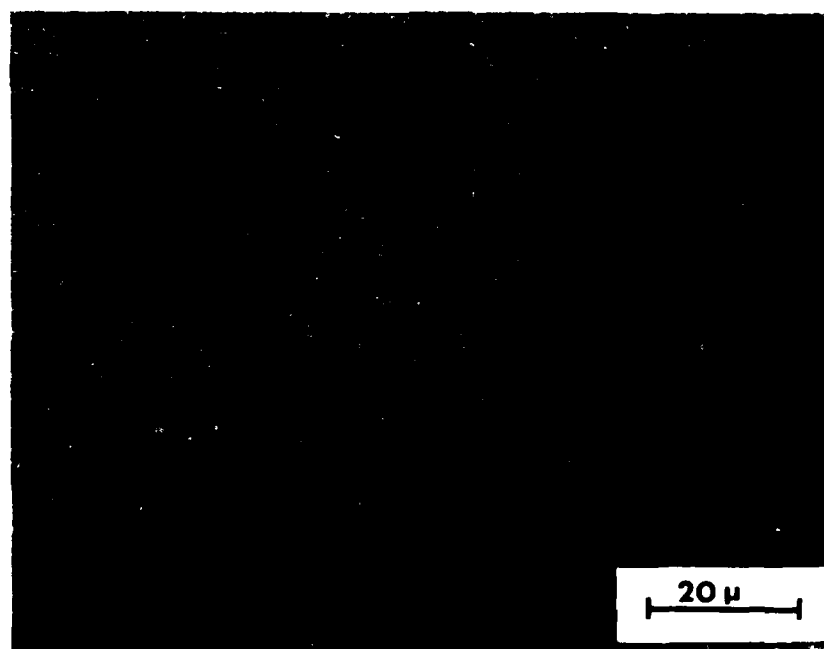
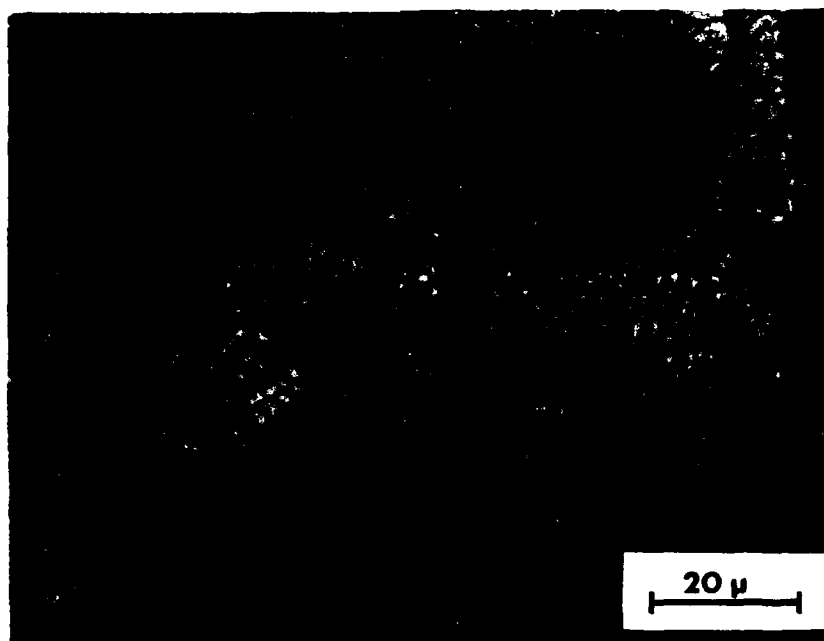


Figure 1.2: Effect of Hf on grain boundary microstructure in directionally solidified MAR-M200.
Top: Hf modified. Bottom: MAR-M200 without Hf additions.

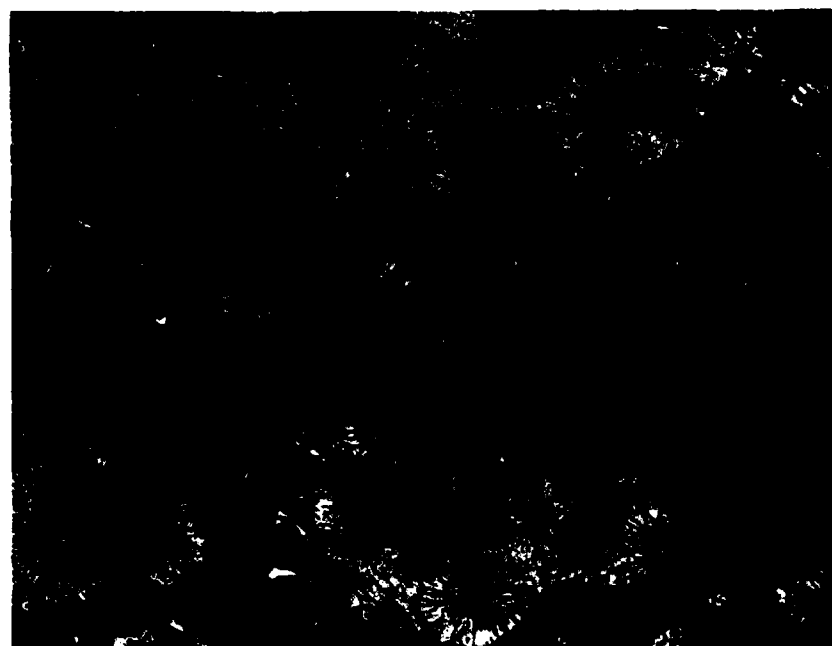
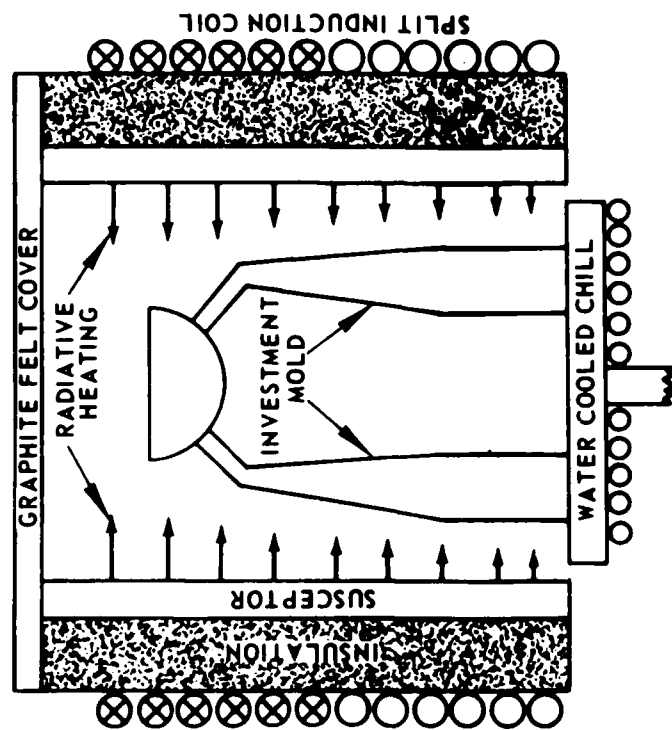


Figure 1.3: Directionally solidified Mar-M200 + 1.5 wt. pct. Hf. These are longitudinal airfoil sections and have nominally been prepared by the same processing method. Blades have had some thermal exposure (1800°F/100 hr.) 250X.

POWER DOWN PROCESS



H.R.S. PROCESS

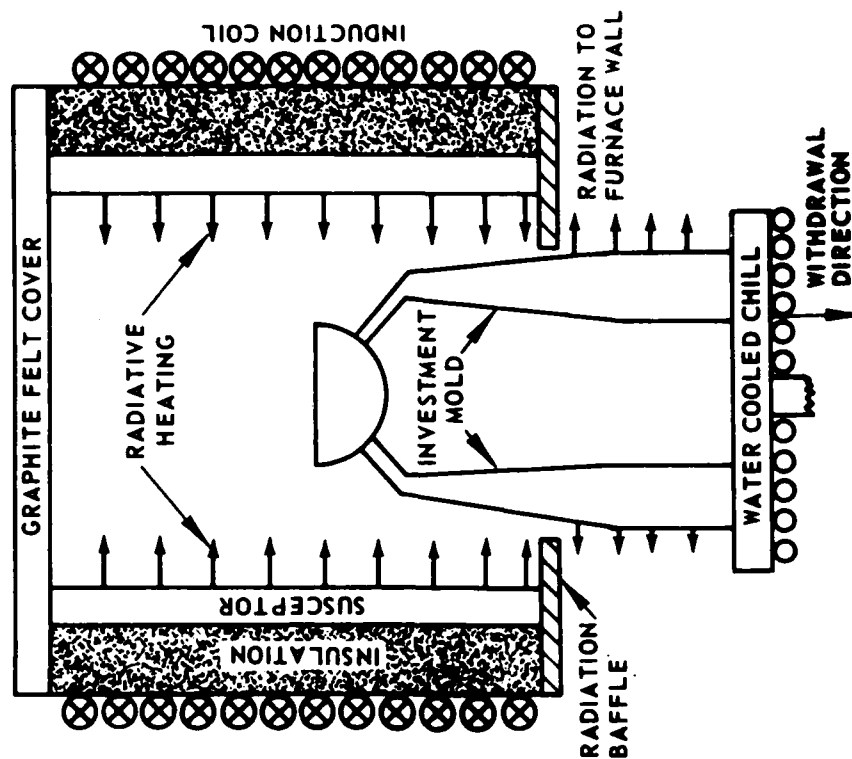


Figure 1.4: Schematic representation of the techniques used in the unidirectional solidification of superalloys. X Indicates power on to induction coil. Left: Power down (P.D.) process. Right: High rate solidification (H.R.S.) process.

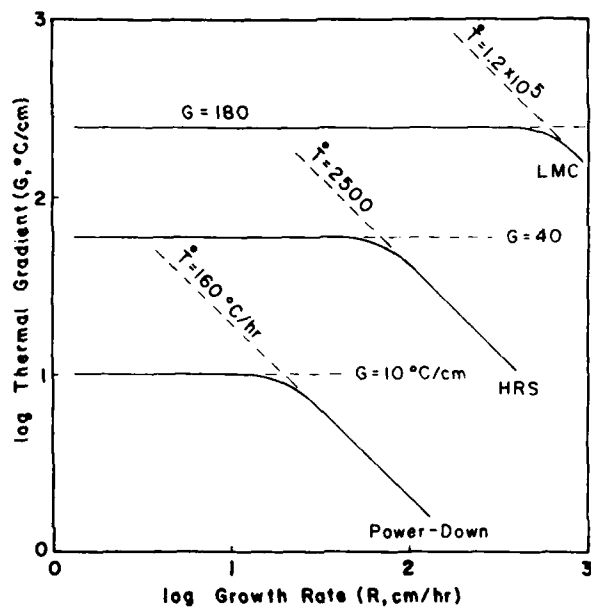


Figure 1.5: Log - log plot of thermal gradient vs. growth rate for various directional solidification processes. Asymptotic thermal gradients and cooling rates are noted.

2.0 Task I: Basic Alloy Parameters

2.1 Purpose

The main goal of this phase of the program was to develop an annotated solidification curve for MAR-M200 and to determine changes in the solidification curve that result from the addition of hafnium. The solidification curve of an alloy is a plot of temperature versus fraction solid in the freezing range. It is annotated to show the phases that form in a particular temperature range and their compositions. For a multicomponent alloy the solidification curve may be used as a guide in understanding the solidification behavior of the alloy under a wide range of casting conditions.

One important solidification feature that both depends upon and influences the solidification curve is microsegregation. In support of the determination of the solidification curves, microsegregation patterns in these alloys have been determined, and the development of microsegregation has been related to the solidification curve.

2.2 Experimental Approach

By a combination of interrupted solidification and isothermal holding experiments combined with thermal analysis, optical metallography, scanning electron metallography and electron probe analysis, the solidification curve, dendrite arm spacing data, and microsegregation data have been obtained for MAR-M200 plus modifications of MAR-M200 with various additions of hafnium. The method of performing each of the solidification experiments is described in sections 2.2.1-2.2.3. Important details of the analysis techniques are described in the same section as the results. Unless otherwise indicated standard techniques have been employed.

2.2.1 Interrupted Solidification

Interrupted solidification runs are made by heating a sample to above its liquidus temperature, slowly cooling the sample below the liquidus temperature, and upon reaching a predetermined temperature quenching the sample to room temperature. For success the solid that formed on the slow cool will be unchanged by the quench. Thus, the progress of solidification can be followed by analyzing samples quenched from a series of temperatures within the freezing range.

The basic concept of interrupted solidification is to give a small sample a relatively slow, controlled cool through the freezing range to interrupt solidification at that point in the process (i.e., temperature or fraction solid) of interest. To be successful in trapping the solidification structure, diffusional processes in the solid phase must be inhibited by the quench. The parameter α_1 , which was introduced in the technical background section on microsegregation (equation 1-5), allows a ready estimate on the amount of diffusion during the quench. For

negligible diffusion $\alpha_i \ll 1$. The value of α_i depends directly on the local solidification time, directly on the solute diffusion coefficient, and inversely on the square of the dendrite arm spacing. The slow initial cooling rate will cause a relatively large dendrite arm spacing in the solid to form before the quench. The large dendrite arm spacing together with the short local solidification time after the quench should serve to "quench in" the solute distribution pattern present at the time of quenching. Our experience indicates that this technique is well suited to the study of Ni-base superalloys.

In this program samples were placed in 1.6 cm. I.D. alumina crucibles and suspended within a tube furnace with a calibrated thermal gradient. The furnace tube was sealed at the bottom and top and a constant rate of argon flow was maintained in the furnace. The samples were heated and cooled by moving the furnace tube relative to the samples. The sample temperatures were measured directly by Pt/Pt-10% Rh thermocouples held 1.0 cm from the bottom of the sample crucibles. The thermocouple tips were protected only by a thin layer of ZrO_2 . The samples were quenched by disconnecting the thermocouple leads, cutting the support wires and allowing the samples to perforate the bottom seal and fall into agitated ice-water. Quantitative metallography was by point counting. Electron microprobe analysis was used to determine solute redistribution behavior during freezing.

2.22 Isothermal Holding

Cooling to a temperature in the solidification range and then holding at that temperature for various time intervals before rapidly cooling will yield information on the rate of change of structure and of solute distribution. It will also coarsen some features of the structure and make them more visible.

Experimentally, the set-up was the same as for interrupted solidification except that when a predetermined temperature was reached on cooling, the furnace motion was stopped and the sample was held at that temperature for a selected time. Then the sample was quenched. Again for Ni-base superalloys good definition was obtained between the solid present at the end of the hold and the solid formed by quenching the liquid present after the hold.

2.23 Thermal Analysis

The thermal data collected on the interrupted solidification runs were combined with qualitative and quantitative metallography to give the temperatures for the first formation of solid phase, the fraction solid at each temperature, and the tendency of various phases to undercool.

Additionally, differential thermal analysis (D.T.A.) was used to check the above values. The D.T.A. method employed relatively large samples, about 50 g., and relatively low cooling rates, less than $10^\circ\text{C}/\text{minute}$. As a result we obtained more representative data than is gained

with normal D.T.A. apparatus. The same size crucibles were used for D.T.A. as for the interrupted solidification and isothermal hold runs. The sample crucible plus one with pure nickel were suspended in close proximity within a furnace. Thermocouples were placed in the sample and in the nickel. The sample was heated or cooled by controlling the power supply to the furnace. A small constant temperature difference was maintained between the two crucibles until transformation occurred in the sample. Then, the temperature of the sample lagged that of the reference nickel. The method was quite sensitive to solidification events involving heat liberation and, also, it was used to estimate fraction solid versus temperature. In plotting the temperature difference between the sample and pure nickel, the temperature of first deviation from the constant value was taken as the liquidus and the temperature of return to a constant value was considered the solidus. The area under the curve was considered to be proportional to the heat generated for total solidification (fraction solid, f_s , equal to one). Then the cumulative area under the curve to a given temperature divided by the total area was considered equal to f_s . One inherent assumption is that each increment of solidification evolves the same amount of heat. Since the composition of each phase and the solid phases forming change during solidification, the foregoing assumption is not expected to hold exactly. Therefore, the D.T.A. determined solidification curves were used only as guides.

2.3 Solidification Curves

Solidification curves for MAR-M200 and MAR-M200 + 1.9% Hf, are given in Figures 2.1 and 2.2. The data leading to the solidification curves are summarized below and listed, in part, in Table 2.1.

2.3.1 Thermal Data

Results of D.T.A. runs on MAR-M200 and MAR-M200 + 1.9% Hf are shown in Figure 2.3 and listed in Table 2.1 where the liquidus and solidus temperatures are given for each alloy. The liquidus temperature represents the first formation of γ . There is evidence of the beginning of formation of a second solid phase at 1335°C for MAR-M200 and at 1311°C for the alloy with 1.9% Hf. There is no indication of eutectic formation in the curve for MAR-M200, however, for the alloy with 1.9% Hf there is an indication that eutectic formation starts at 1230°C. The solidification curves marked D.T.A. in Figures 2.1 and 2.2 were obtained by measuring the areas under the D.T.A. curves of Figure 2.3. As indicated at the end of section 2.23, these solidification curves are considered less accurate than those determined by quantitative metallography.

The liquidus temperatures measured for each alloy on each interrupted solidification and isothermal hold sample are listed in Table 2.1. The scatter from run to run is small. However, the liquidus temperature measured here is significantly lower than temperatures reported by others(1,2). Based on our relatively slow cooling rate, large sample size, and the fact our thermocouple was immersed in the

alloy with only a thin protective layer of ceramic, we expect the present data to be more reliable.

2.32 Metallographic Data

Figures 2.4 and 2.5 show relatively low magnification photomicrographs of interrupted solidification samples of MAR-M200 + 1.9% Hf, quenched from 40% and 55% solid, respectively. The contrast between the primary γ dendrites present before the quench and the quenched liquid is clear. Figures 2.6 and 2.7 show a series of higher magnification photomicrographs of MAR-M200 and MAR-M200 + 1.9% Hf, respectively. These series allow the bracketing of the first temperature of MC formation and of eutectic γ' formation. Note, for example that in MAR-M200, MC had not formed by 1343°C, but MC is present at 1336°C. For the alloy with 1.9% Hf, MC forms between 1300 and 1305°C.

Examination of the samples in the polished but unetched condition shows the carbides very well. (Note: Figure 2.8, top) Because the samples were quenched while partially liquid, the relation of the carbides to the primary γ dendrites is apparent, also. At this point carbide morphology can be observed and the volume fraction measured. Etching brings out the segregation in the primary dendrites and the eutectic microconstituent. Quantitative metallography can then be performed on the eutectic constituent. Quantitative metallography on the primary phase can be performed in the etched and unetched condition. Based on quantitative metallography and temperature measurements on the interrupted solidification samples, the solid curves in Figures 2.1 and 2.2 were obtained.

It is pointed out here, but not reported in detail, that several nonequilibrium phases have been observed and identified in the quenched liquid regions. These phases result from the partitioning of elements into the liquid and would not normally occur in alloys continuously cooled, quickly or slowly, from a totally liquid condition.

2.4 Microsegregation

The interrupted solidification technique allows the tracking of the solute redistribution process during solidification and, thus, the development of microsegregation. Figure 2.9 shows the distribution of alloying elements between solid and liquid phases determined by scanning across a dendrite arm on a path extending into the quenched liquid pools on either side. The sample is MAR-M200 + 1.9% Hf quenched from 1300°C.

A scan across any one dendrite arm is not likely to be representative. A more representative technique is to point count on an array of points taken so that the point spacing is greater than the dendrite spacing but not a rational multiple. In this work we used grids of 11 x 11 points for a total sample of 121 points. At each point W and Ti intensities were counted. The data for each element were then converted to weight percent by the ratio:

$$C_i = \frac{N C_o I_i}{\sum_{j=1}^N I_j} \quad (2-1)$$

where C_i is the composition on the 'i'th point in the grid, N is the total number of points in the grid, C_o is the average weight percent of the element in the sample, and the I_i 's are the measured intensities in counts per second. The data for each element from a sample were ordered by weight percent (ascending order for Ti, descending order for W) and then plotted as weight percent of element versus volume fraction, f , where

$$f = \frac{\text{cumulative point number}}{N} \quad (2-2)$$

Figure 2.10 compares this statistically derived solute distribution across a dendrite arm for samples quenches from 1343°C and 1315°C. One surprising feature is the apparent redistribution in W that occurs within the solid phase.

2.5 Dendrite Morphology

Secondary dendrite arm spacings were made on primary dendrites that seemed to be roughly parallel to the plane of polish. The results are reported in Table 2.1. The data are discussed in section 7.0.

2.6 Carbides

One observation that can be made by following the progression of MC is that the carbides in this regime of cooling rates form first in the script morphology. The script carbides then coarsen (to reduce surface area) into the blocky form. In this case script and blocky carbides are different stages in the same process.

2.7 Eutectic

The $\gamma + \gamma'$ eutectic forms in the last stages of freezing. The eutectic did not start to form until the alloy was over 80% solid.

As cast MAR-M200 has been reported to show 2-5 vol % eutectic, whereas the hafnium modified alloy (1.9 wt% Hf) shows about 15 vol % eutectic. Small to moderate amounts of eutectic are desirable in improving the transverse ductility in creep. However, large amounts of eutectic are undesirable because (1) the eutectic retains large amounts of alloying elements that otherwise would have strengthened the matrix and (2) large amounts of eutectic impair the mechanical properties. It has

been observed(3) that in superalloys such as IN 100, the eutectic micro-constituent can be eliminated or at least greatly reduced by a very slow cool from the liquidus to the solidus temperature. The precipitation of $\gamma + \gamma'$ eutectic can be suppressed(4) by splat cooling in Inconel 713 C alloy. In the slowly cooled samples reported in Table 2.1 and Figures 2.1 and 2.2, the amount of $\gamma + \gamma'$ eutectic is substantially less than the amount typically found in commercial castings.

2.8 References

1. J. K. Tien and R. P. Gamble, "The Suppression of Dendrite Growth in Nickel Base Superalloys During Unidirectional Solidification," Mater. Sci. Eng., 8 (1971) 152-160.
2. Claudia J. Burton, private communication.
3. E. P. Whelan, "The Elimination of Eutectic γ' from IN 100," J. Inst. Metals, 100 (1972) 333-35.
4. A. K. Bhambri, T. Z. Kattamis and J. E. Morral, "Cast Microstructure of Inconel 713 C and Its Dependence on Solidification Variables," Met. Trans., 6B (1975) 523-537.

TABLE 2.1 Basic Alloy Parameter Studies

A. Differential Thermal Analysis

<u>Temp Prior to Quench (°C)</u>	<u>Local Solidif. Time (sec)</u>	<u>Secondary Dendrite Spacing (μm)</u>	<u>Primary Carbides (Vol. %)</u>	<u>Eutectic (Vol. %)</u>	<u>Temperature Liquidus (°C)</u>	<u>Solidus (°C)</u>
MAR-M200						
1250	3750	148	2.26	0	1367	1260
MAR-M200 + 1.9% Hf						
1210	660	64	1.5	4.1	1340	1214
1200	830	57	1.5	6.6	1338	1216

B. Interrupted Solidification

<u>Temp Prior to Quench (°C)</u>	<u>Liquidus to Quench Time (sec)</u>	<u>Secondary Dendrite Spacing (μm)</u>	<u>Fraction Solid (Vol. %)</u>	<u>Carbide (Vol. %)</u>	<u>Liquidus (°C)</u>
MAR-M200					
1343	580	82	59	0	1365
1336	638	74	62.5	1.4	1366
1315	2100	108	77	1.6	1367
MAR-M200 + 1.9% Hf					
1312	1150	70	42	0	1339
1306	1361	80	44	0	1338
1300	1710	99	61	0.8	1338
1278	1560	91	78	1.5	1340

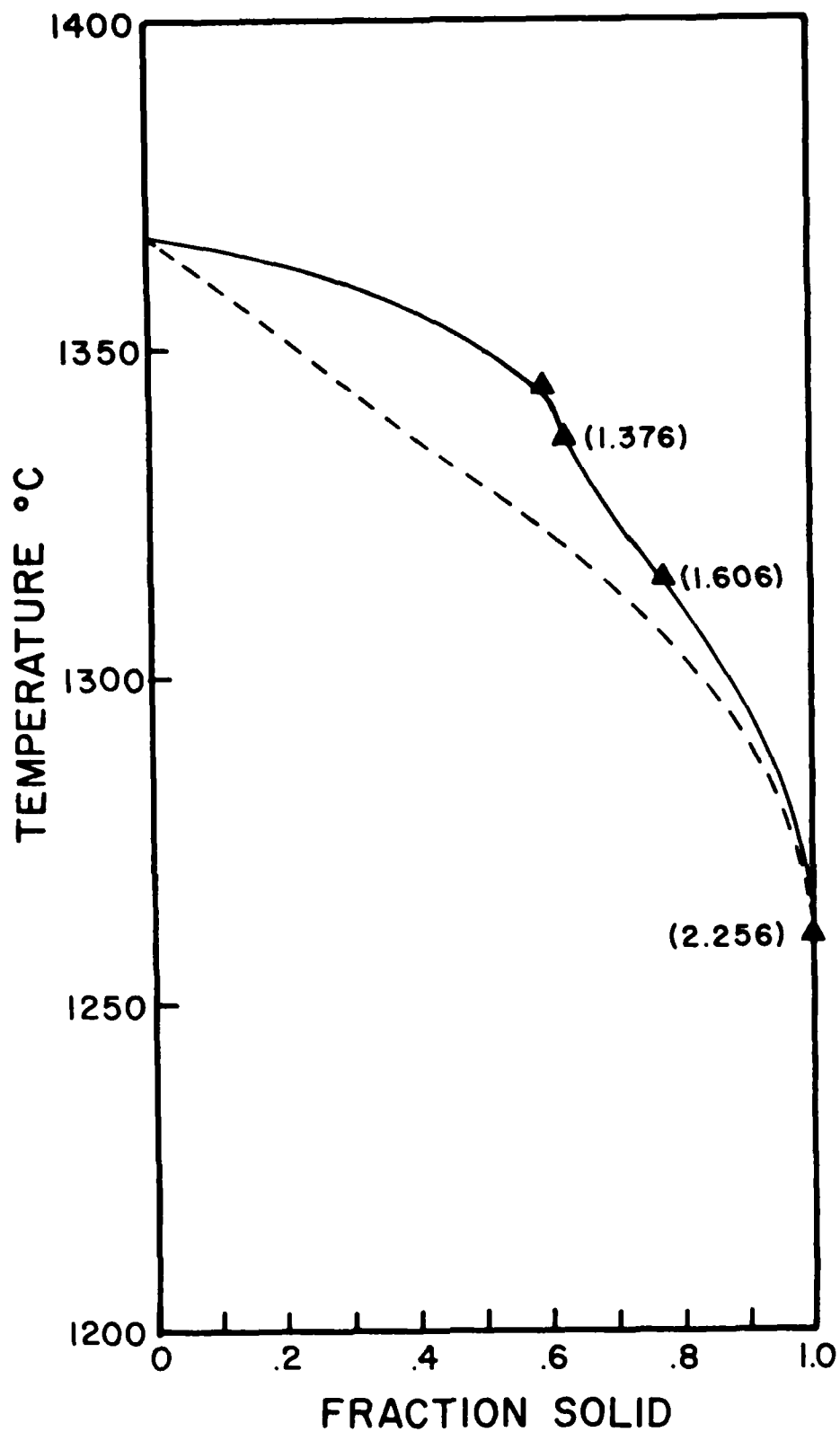


Figure 2.1: Solidification curve for MAR-M200. Solid line is determined by quantitative metallographic analysis. Dashed line is determined by thermal analysis. Numbers in parentheses indicate volume % carbide, if any, corresponding to that data point.

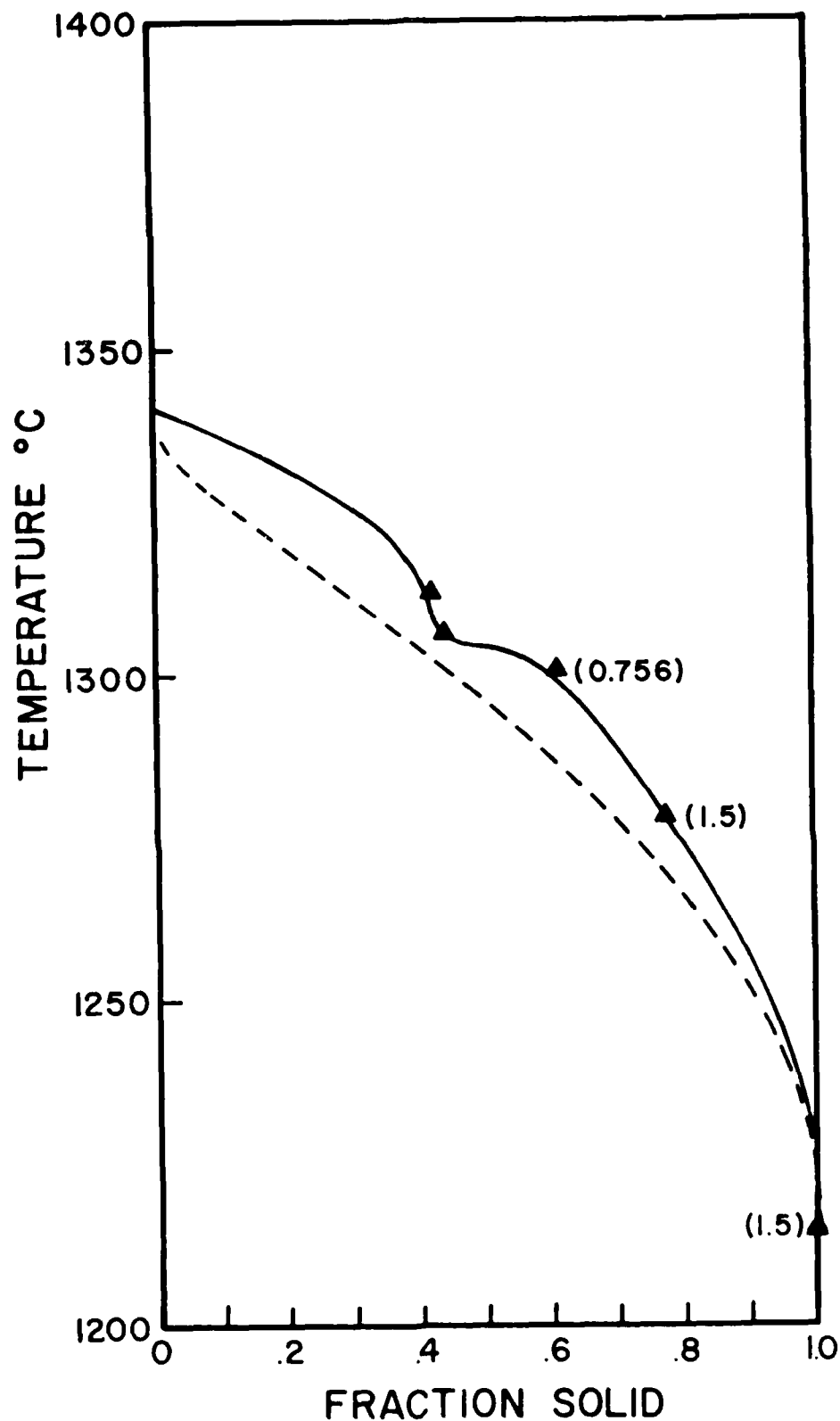


Figure 2.2: Solidification curve for MAR-M200 modified with 1.9% Hf. Solid line is determined by quantitative metallographic analysis. Dashed line is determined by thermal analysis. Numbers in parentheses indicate volume % carbide, if any, corresponding to that data point.

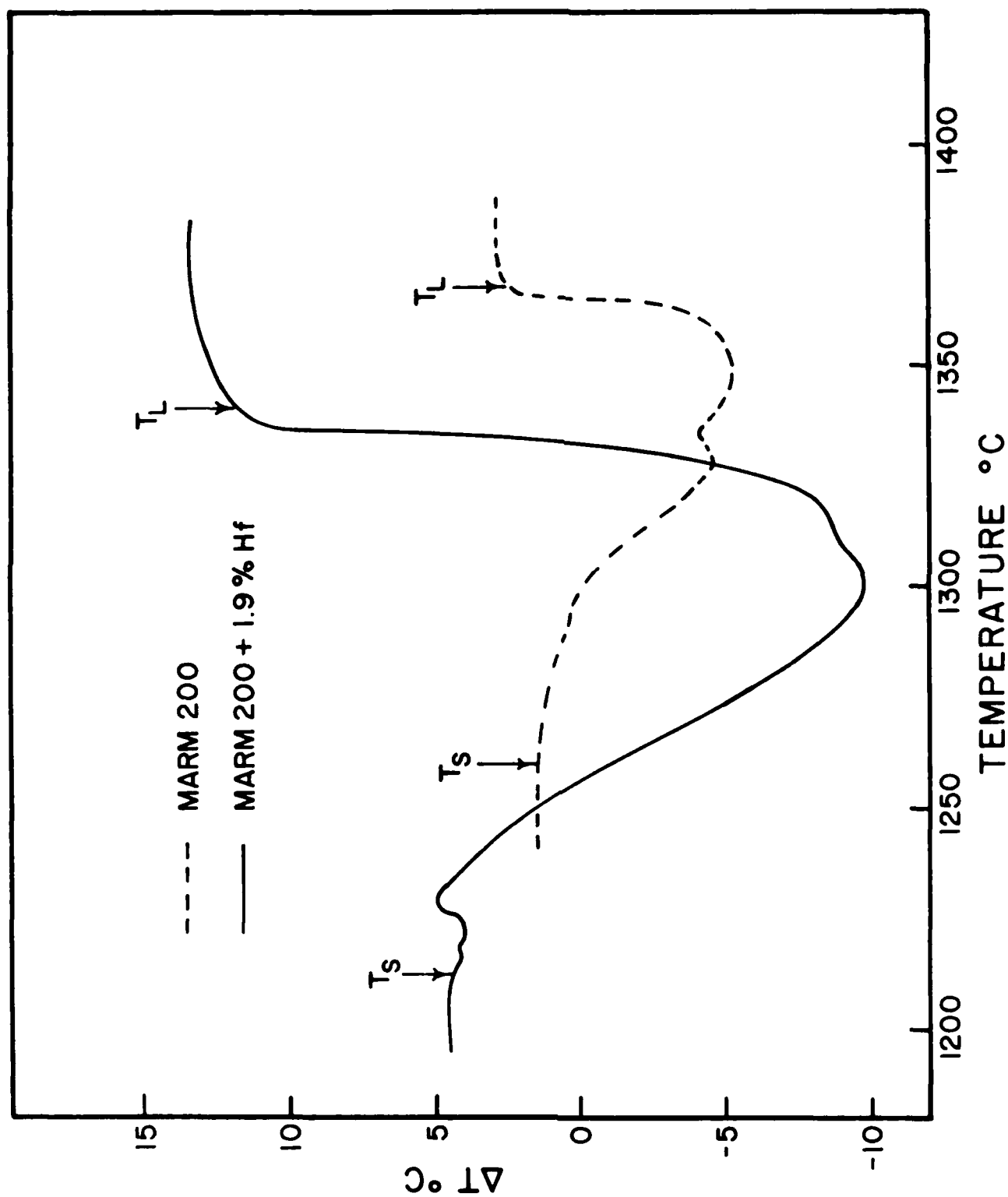


Figure 2.3: Results of differential thermal analysis runs on MAR-M200 and MAR-M200 modified by 1.9% Hf. The plot is of temperature differential between Ni standard and superalloy sample versus sample temperature.

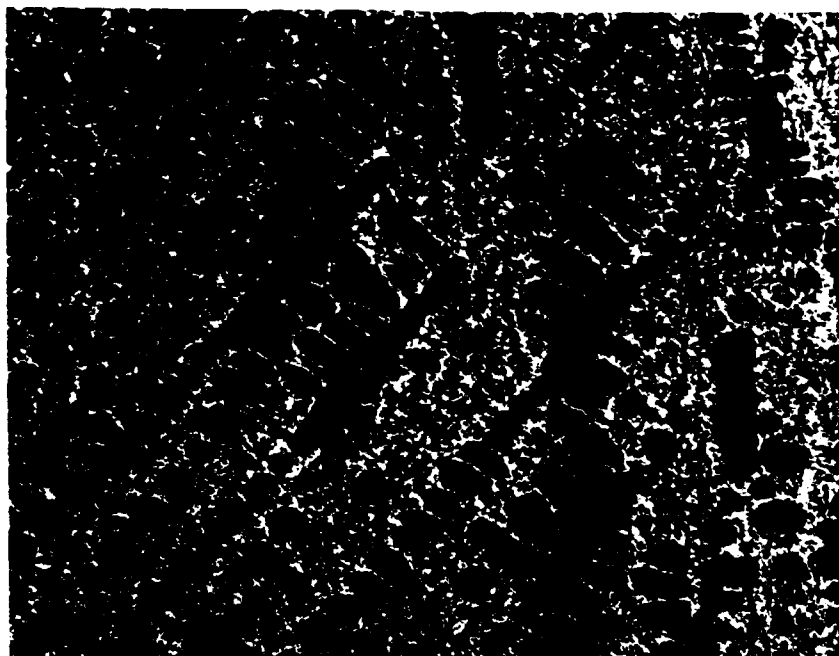


Figure 2.4: Photomicrograph of interrupted solidification sample for MAR-M200 modified by 1.9% Hf quenched at 40% solid (44X)

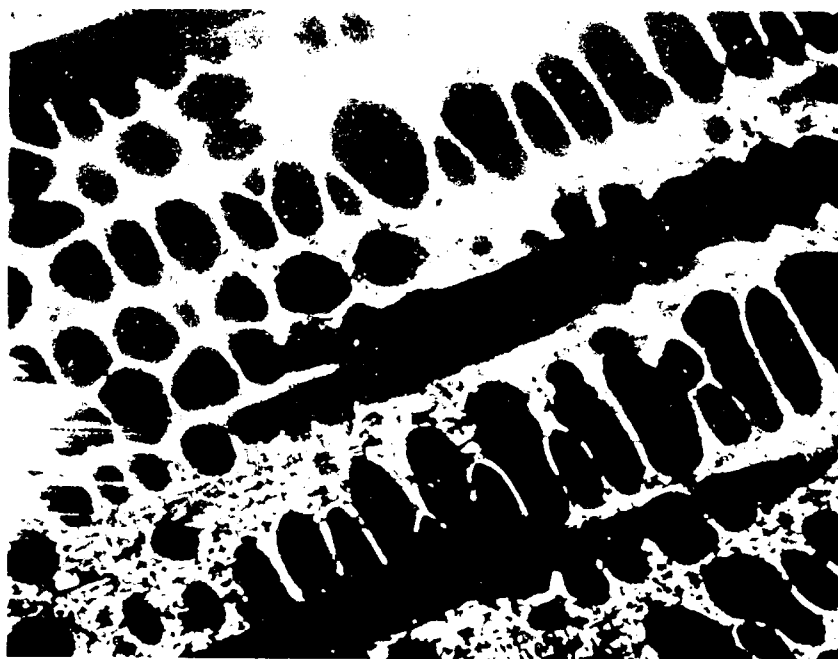


Figure 2.5: Photomicrograph of interrupted solidification sample for MAR-M200 modified by 1.9% Hf quenched at 55% solid. (76X)

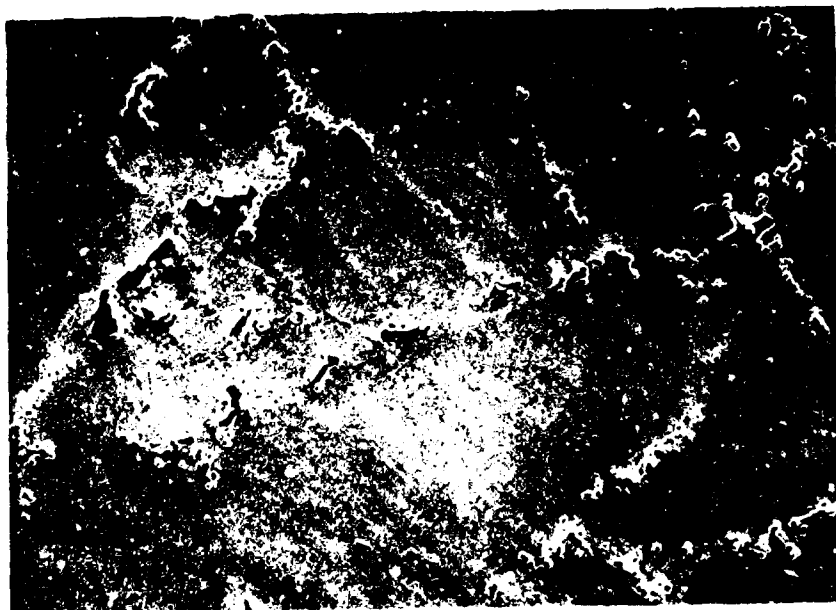


Figure 2.6a: Photomicrograph of interrupted solidification sample for MAR-M200 quenched from 1343°C. (300X)

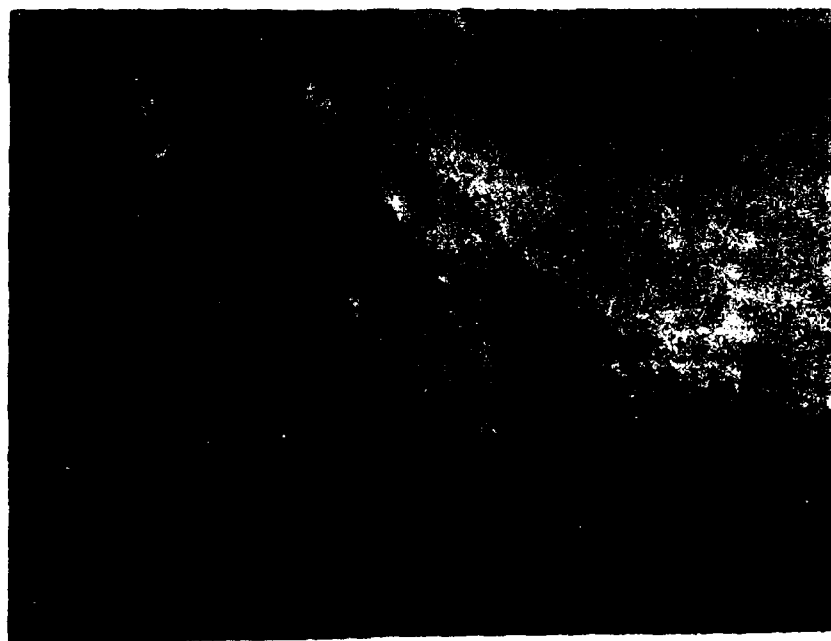


Figure 2.6b: Photomicrograph of interrupted solidification sample for MAR-M200 quenched from 1336°C. (200X)



Figure 2.6c: Photomicrograph of interrupted solidification sample for MAR-M200 quenched from 1315°C. (160X)

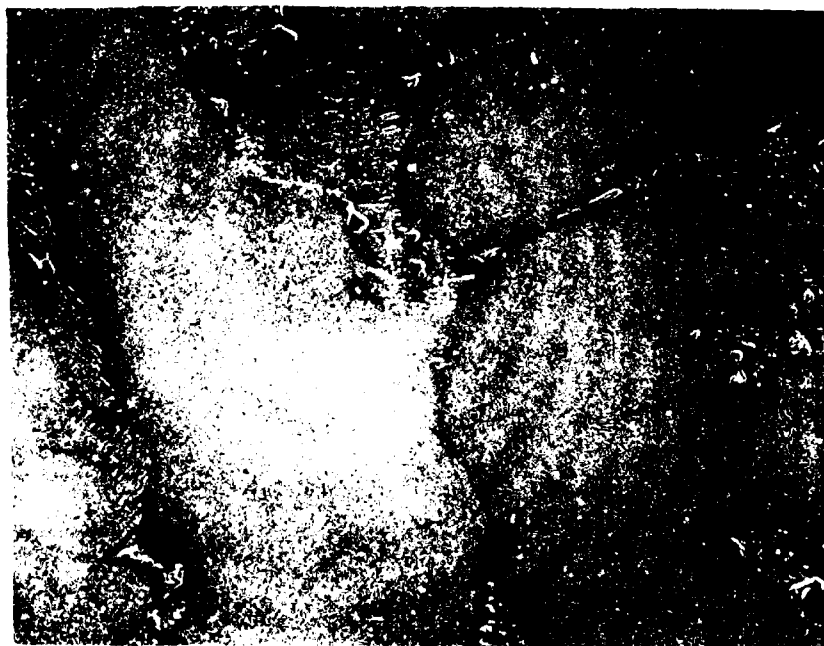


Figure 2.7a: Photomicrograph of interrupted solidification sample for MAR-M200 modified by 1.9% Hf quenched from 1305°C. (300X)



Figure 2.7b: Photomicrograph of interrupted solidification sample for MAR-M200 modified by 1.9% Hf quenched from 1300°C. (200X)

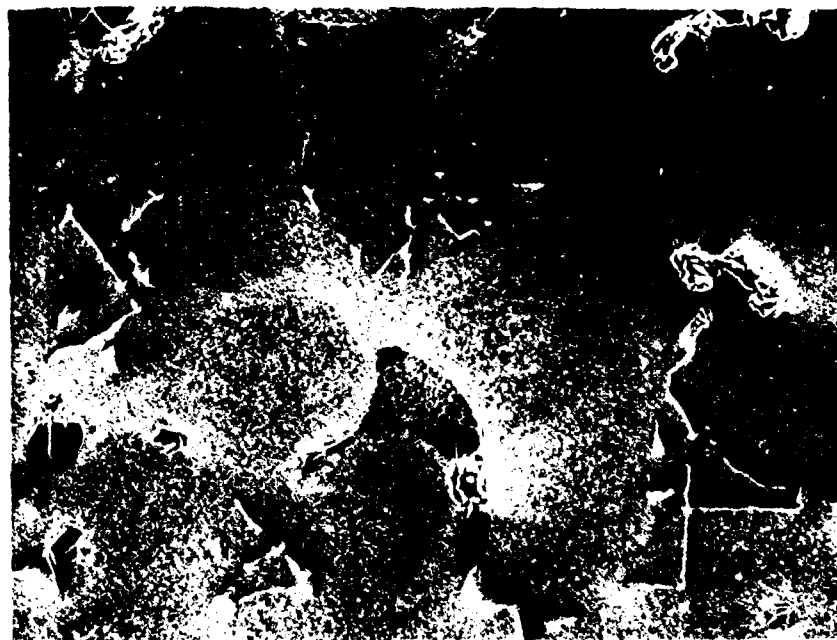


Figure 2.7c: Photomicrograph of interrupted solidification sample for MAR-M200 modified by 1.9% Hf quenched from 1210°C. (300X)

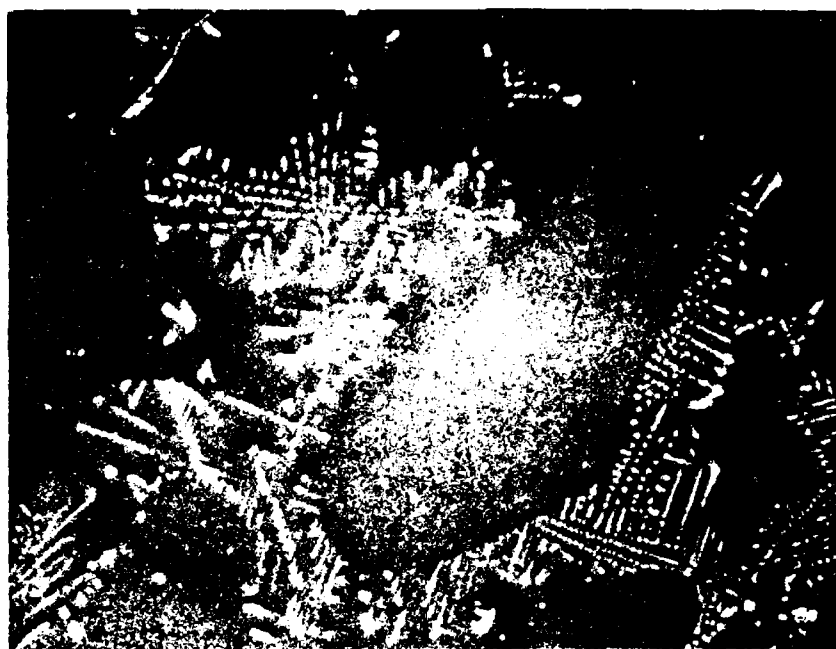


Figure 2.8: Comparison of unetched (top, 1000X) and etched (bottom, 1600X) interrupted solidification samples of MAR-M200 quenched from 60% solid.

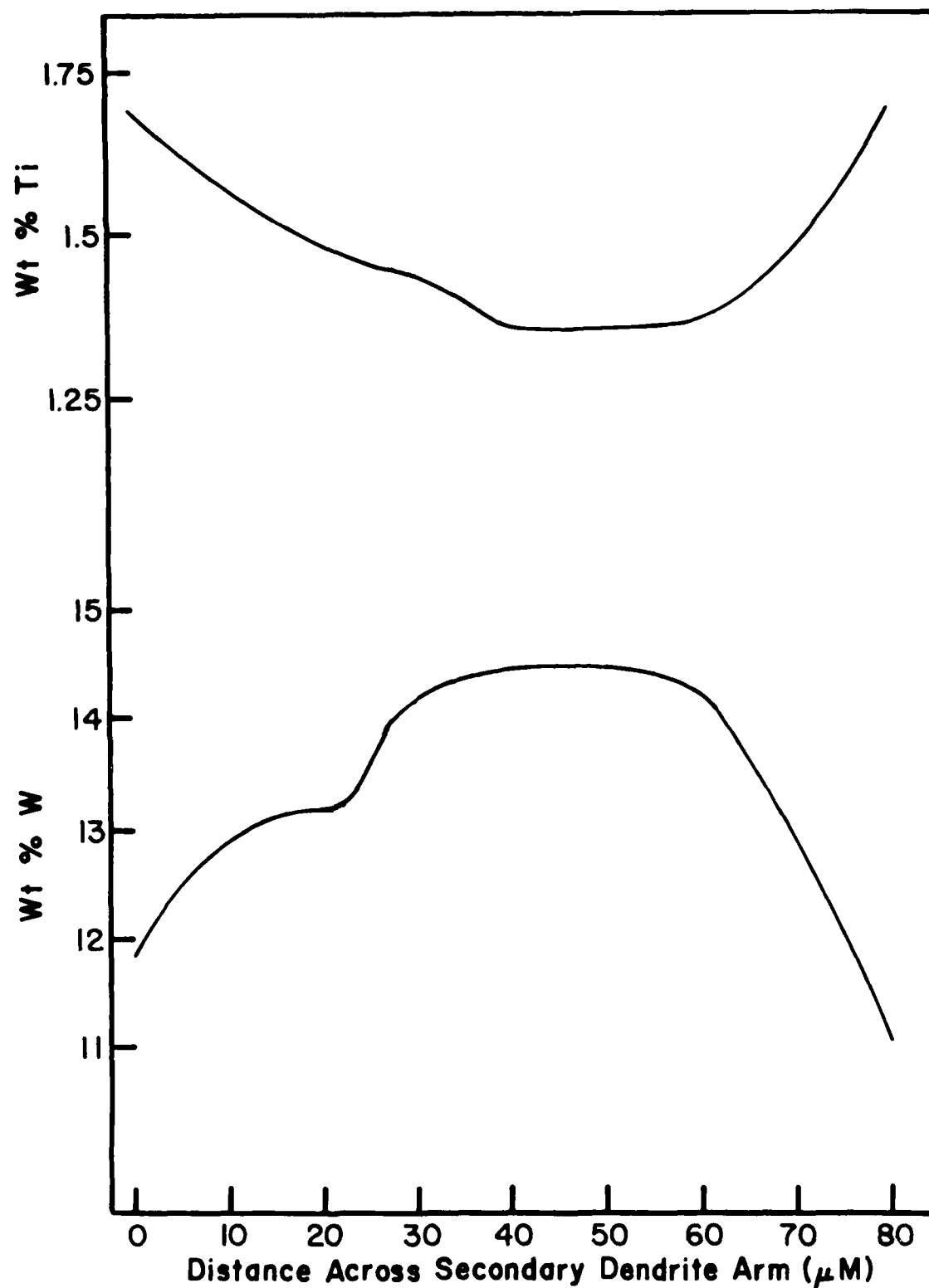


Figure 2.9a: Variation of Ti and W across secondary dendrite arm in MAR-M200 modified by 1.9% Hf. Traces are made across the same arbitrarily selected secondary dendrite arm.

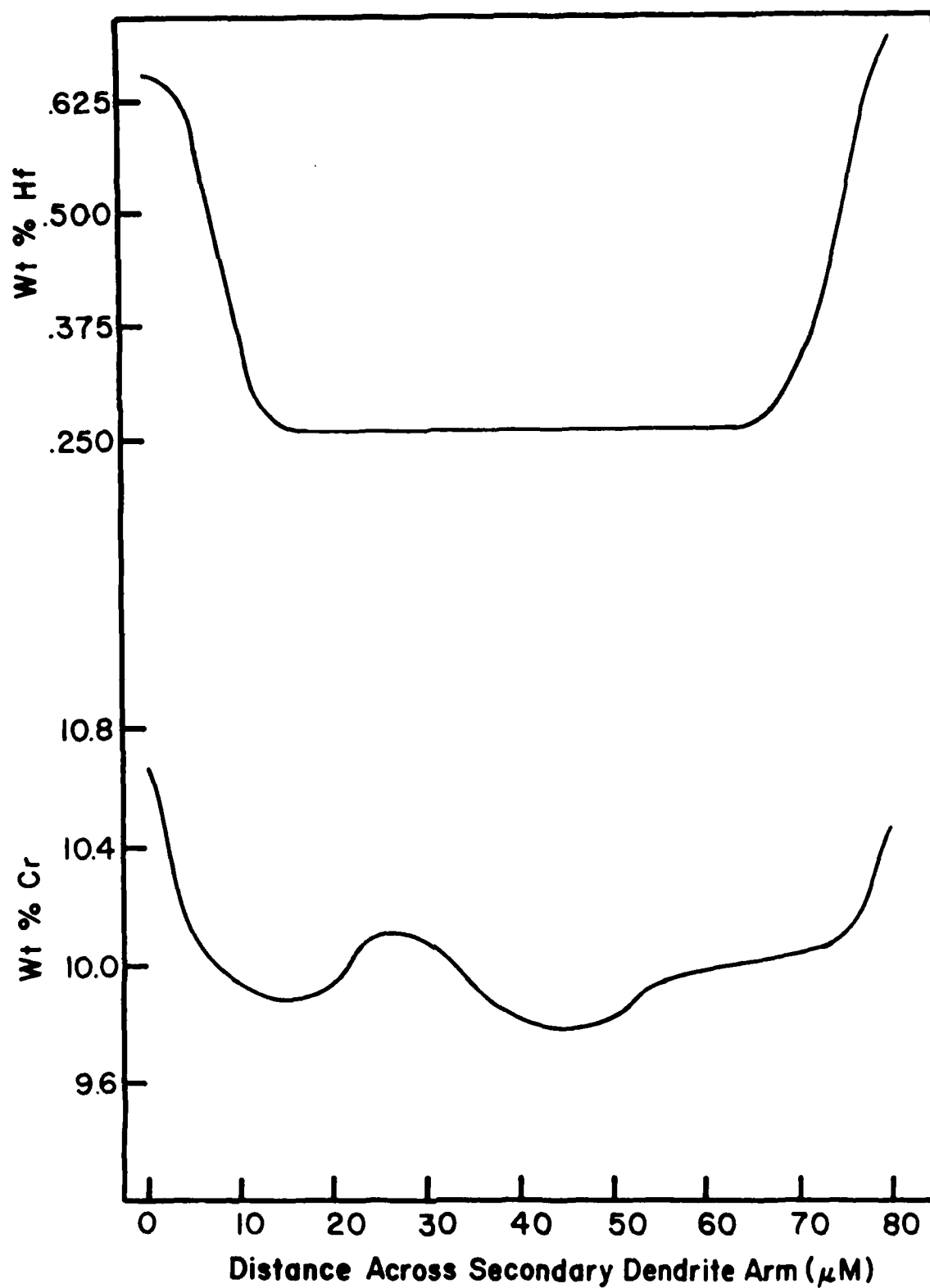


Figure 2.9b: Variation of Hf and Cr across secondary dendrite arm in MAR-M200 modified by 1.9% Hf. Traces are made across the same arbitrarily selected secondary dendrite arm.

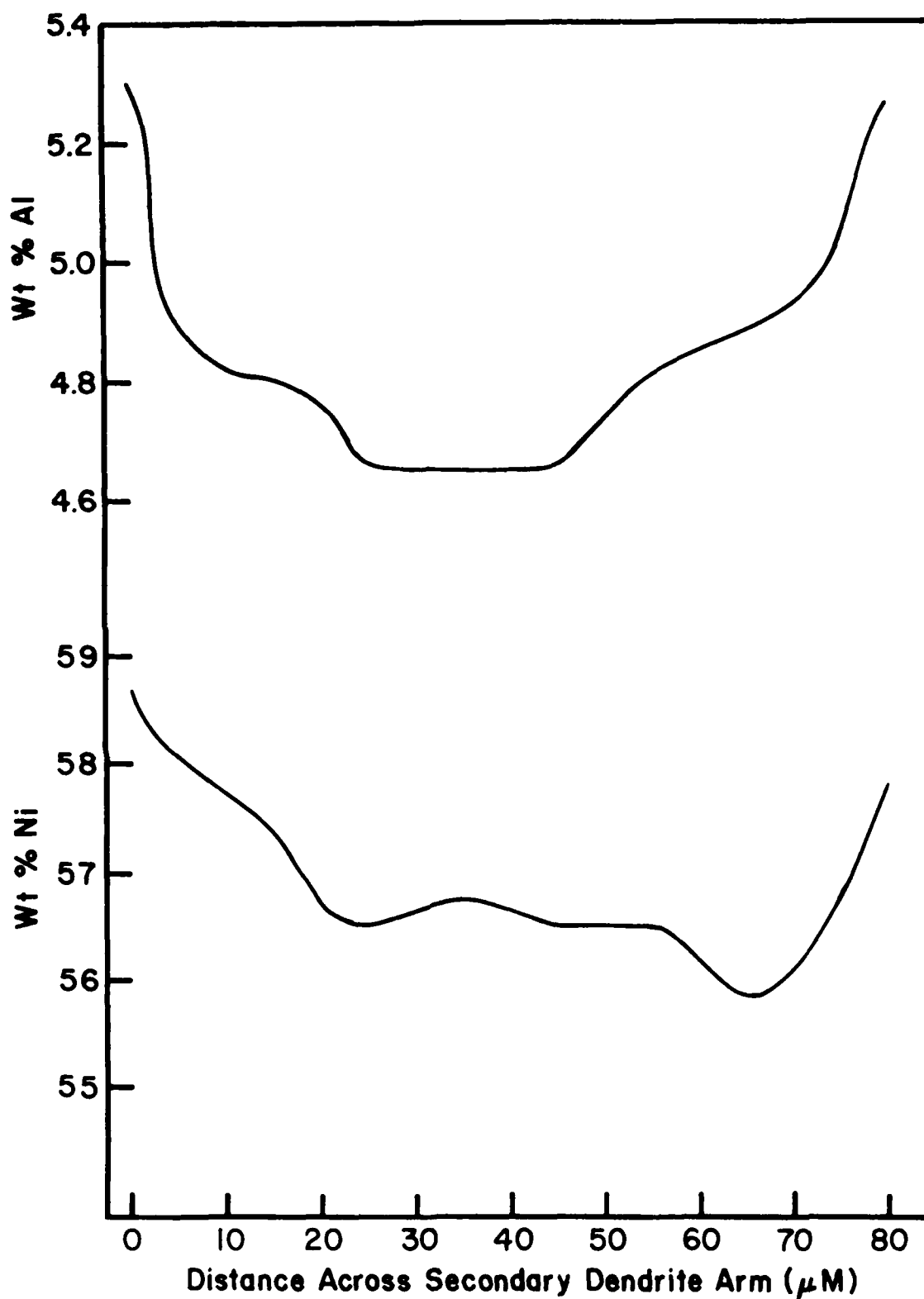


Figure 2.9c: Variation of Al and Ni across secondary dendrite arm in MAR-M200 modified by 1.9% Hf. Traces are made across the same arbitrarily selected secondary dendrite arm.

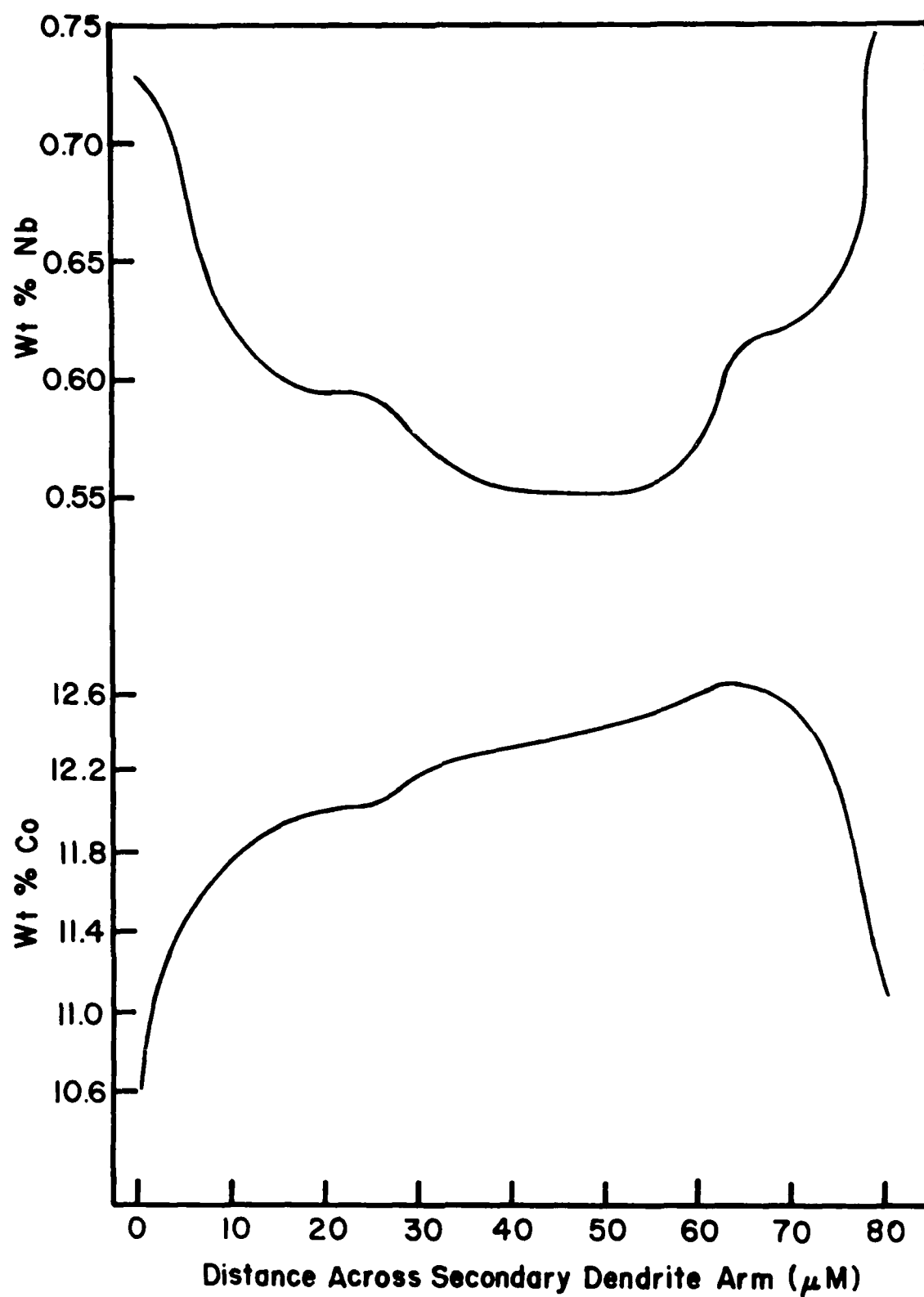


Figure 2.9d: Variation of Nb and Co across secondary dendrite arm in MAR-M200 modified by 1.9% Hf. Traces are made across the same arbitrarily selected secondary dendrite arm.

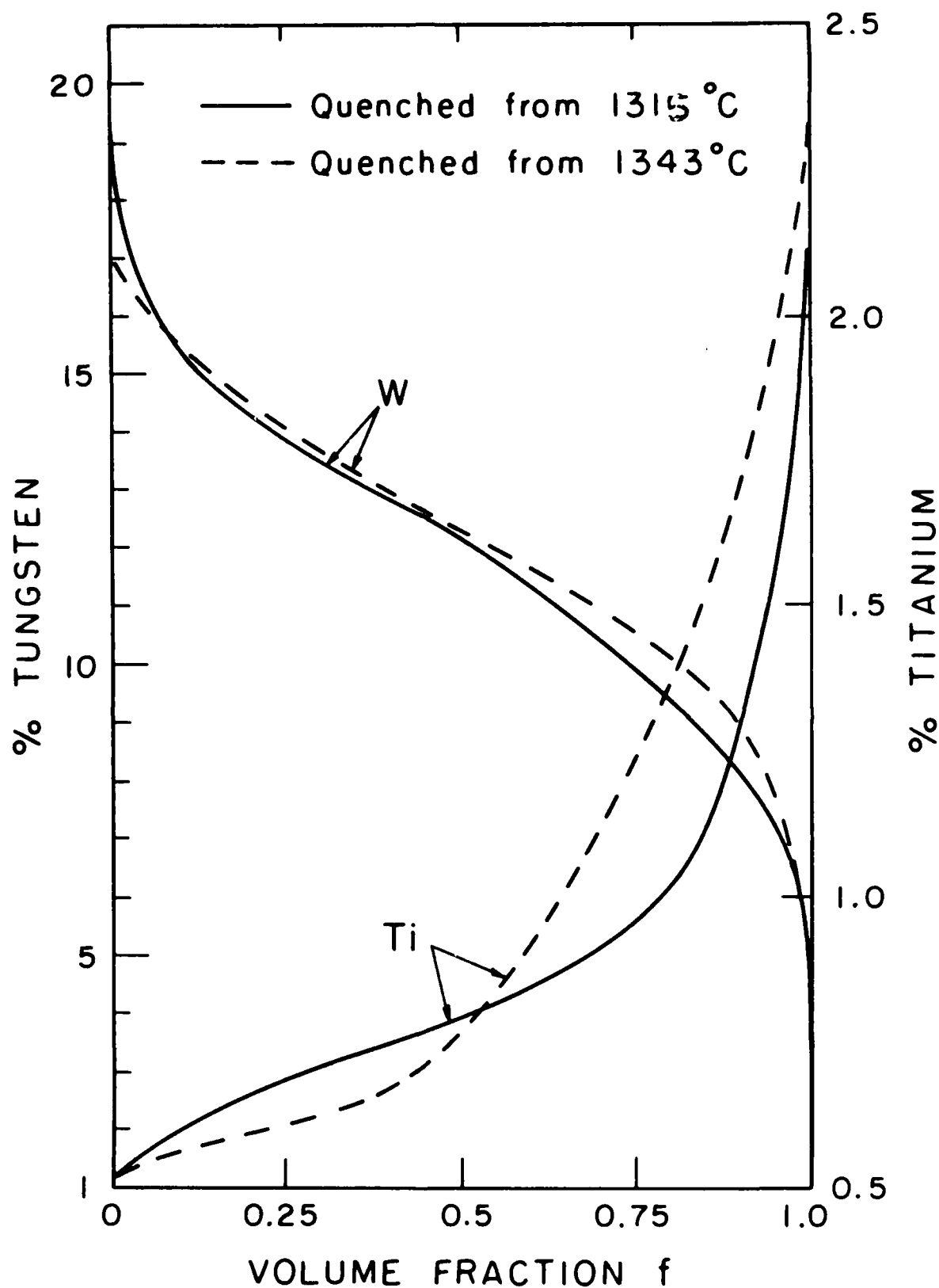


Figure 2.10: W and Ti distributions in MAR-M200 interrupted solidification samples quenched from 1343°C (59% solid) and 1315°C (77% solid). C_0 for W and Ti were assumed to be 12% and 1%, respectively.

3.0 Task II: Controlled Unidirectional Solidification

3.1 Introduction

A directed fundamental approach has been taken to define the interdependence of microstructure and growth conditions on directionally cast MAR-M200 and the influence of hafnium additions on the relationship.

Since variation in the microsegregation patterns of Hf modified MAR-M200 could be induced in the wide range of solidification conditions available in the laboratory scale liquid metal cooling (LMC) apparatus described in detail below, a powerful analytical tool was available for this study. The basic rationale for using this tool was that a complete description was available for the thermal events which occurred during solidification. A solidification procedure could be carried out and subsequently carefully analyzed to give the precise interrelationship between growth variables such as thermal gradients, growth rates, local solidification times and mushy zone heights and microstructural variables such as primary and secondary dendrite arm spacing, carbide shapes and sizes, and eutectic volume fractions. Once a base case was established and characterized, this solidification system allowed for the variation of a single selected parameter by a controlled amount.

3.2 Experimental Procedure

3.2.1. Materials and Casting Apparatus

Perhaps the most versatile controlled solidification technique is the liquid metal cooling (LMC) process. A laboratory version of this technique is illustrated in Figure 3.1. Normally a bar of superalloy is made with a central cavity to accept a set of axial thermocouples in a thin ceramic protection tube. This bar is placed inside of a ceramic tube or mold and is melted in-situ using induction heating. A high frequency induction generator powers a coil of variable turn density supported on a pyrex mandril. A large diameter quartz tube is used to define the vacuum system required to protect the superalloy from oxidation. This tube is cooled on the outside by a water tower. The heat is generated bysuscepting to tubes of tantulum or graphite just inside the quartz tube. The mold is suspended from above by a refractory metal tube and ceramic pins. The thermocouples which are placed at various positions along the length of the supperalloy bar are brought up out of the vacuum system inside the mold support tube. The mold is centrally placed in the susceptor and the top and bottom of the hot zone are sharply defined with highly efficient heat shields. Beneath the lower set of shields, a molten cooling bath is held at a controlled temperature. The coolant may be circulated to maximize heat transfer. When the molten Ni-base superalloy has been brought up to the desired level of superheat, the mold can be lowered at a controlled rate into the cooling bath. The heat transfer coefficient is so large for this process that the growth rate and the thermal gradient are essentially independent, which is never the case for power-down or for withdrawal. In addition, very high levels of thermal gradient can be achieved (see

Figure 1.5) with a vacuum compatible cooling system, e.g. 200°C/cm. The flexibility which this controlled solidification system allows makes it an ideal vehicle for studying solidification microstructures produced under a wide variety of conditions.

Various combinations of mold materials, Hf alloy levels, and cooling schemes have been used to obtain specific growth conditions. The runs completed on this task are summarized in Tables 3.1, 3.2,* and 3.3. The compositions of the alloy rods melted in the LMC apparatus are given in Table 1.1. The molds were 1.2-1.4 cm. diameter bars from 10-20 cm. in length. Melting and stabilization were carried out using closed loop induction heating. Immersion or withdrawal was then initiated at the lower of the rates, R_1 . The mold was lowered for a distance of at least 5 cm. (4 mold diameters). At this point a controlled acceleration growth transient was initiated. This was carried out in such a way that growth rate increased linearly with distance, and therefore exponentially with time, from the lower rate, R_1 , to the higher rate, R_2 , according to the equation:

$$R = R_1 \exp \left[\frac{(R_2 - R_1)}{h} t \right] \quad (3-1)$$

where R is the instantaneous rate and h is the transient height. This transient was computed ahead of time on an IBM 370 interactive digital computing system. The purpose of the smooth acceleration was to propagate the existing grains and dendrites with minimum disruption. The small rate change steps were accomplished with a variable speed drive motor. The transient heights were 0, 1 cm, or 2 cm, depending on the magnitude of the rate change. Finally, at least 5 cm of material was grown at R_2 under nominally steady state conditions.

3.2.2. Microstructural Analyses

From the unidirectionally cast bars transverse cuts 2 cm. below the start of the transient and 2 cm. above the top of the transient were taken for primary dendrite spacing, carbide, and eutectic measurements under well documented solidification conditions. Longitudinal specimens were analyzed for secondary dendrite arm spacing measurements as well as eutectic volume fraction. The method of cutting from the bar is illustrated in Figure 3.2.

The microstructural analyses started with a definition of MC carbide size and shape. The transverse sections were mounted, mechanically polished, and final polished using a Syntron vibratory polishing table. They were then examined and photographed at 500X in the as-polished condition. A representative micrograph was taken in each case. In addition, any unusual features were documented.

*Table 3.2 also includes the results of calculations and measurements which are discussed in sections that follow.

The transverse samples used for carbide analysis were swab etched in fresh 50% lactic acid, 33% HCl and 17% HNO₃ for primary dendrite analysis. In some cases it was necessary to repolish and re-etch the specimen for improved contrast. Typical photomicrographs were taken at 100X for the lower sections and 200X for the higher sections. The number of dendrite centers (N) per unit area (A, on the film) at magnification M was then counted. An idealized rhombohedral array of dendrites per unit area would have a side length d₁ (equivalent primary spacing) which is given by:

$$d_1(\text{cm.}) = \frac{1}{M} \sqrt{\frac{2A(\text{cm}^2)}{N\sqrt{3}}} \quad (3-2a)$$

or, more conveniently:

$$d_1(\mu\text{m}) = \frac{10^4}{M} \sqrt{\frac{2A(\text{cm}^2)}{N\sqrt{3}}} \quad (3-2b)$$

Surface preparation for secondary dendrite arm spacing measurements was identical to that for primary dendrite observations, except that the Syntron operation was skipped on the long sections, such as the transient lengths. The measurements were taken in regular regions with fine structure such that no features were missing due to substantial displacement between section plane and dendrite core. The number of secondaries, N, was counted along a line of length L, at magnification M. The secondary spacing is then given by:

$$d_2 = \frac{L}{M(N-1)} \quad (3-3)$$

Several procedures were used for measurement of eutectic volume fraction. The most reliable technique was to point count by using a metallograph with a viewing screen. A transparency with a grid pattern was set over the screen and the number of points falling over a eutectic pool counted. Then the sample was moved a consistent amount, the grid replaced, and the points falling on eutectic pools counted again. The sample was moved a number of steps in the +X-direction, then one step in the +Y-direction and then a number of steps in the -X-direction, etc., thus tracing out a grid pattern on the sample. Correlation effects were avoided by rotating the dendrite pattern relative to the X and Y directions such that any eutectic alignment was not allowed to be coincident with the translation axes. This could be a serious problem for longitudinal specimens. The transverse analyses showed less scatter.

3.2.3. Thermal Analysis

For the purpose of process control or process analysis, cooling curves are normally generated during the fabrication of a directional casting. This section describes the use of the Pratt and Whitney Aircraft TCTEMP and PROCES computer programs for obtaining pertinent data which completely characterize the thermal behavior of the directional solidification process starting with the experimentally determined cooling curves. Cooling curves, in the form of thermocouple EMF output vs. time, taken at various positions serve as input parameters for the TCTEMP deck for the IBM 370. In its present configuration, this deck converts EMF values from Pt-6Rh/Pt-30Rh thermocouples (Type B) into temperature in °F or °C and creates an output file or punches the output on cards suitable for input into the PROCES deck. In cases where temperature is recorded directly as a function of time, the cooling curve input data is simply written on coding sheets for keypunching or direct input from an interactive terminal.

The PROCES program generates axial thermal profiles (temperature vs. height with parametric time) from the cooling curves, i.e. $T(Z_i, t)$ vs. t . The thermal profiles are expressed and plotted as best fit third order polynomials:

$$T(Z, t_n) = a_0 + a_1 Z + a_2 Z^2 + a_3 Z^3 \quad (3-4)$$

where n is a time index and $a_i = a_i(n)$. Whenever a thermal profile intersects the liquidus temperature, the assumed horizontal liquidus surface is located in time and space by spatial iteration. Points can thus be tabulated for liquidus and solidus interfacial positions (Z_L and Z_S) at various times. These points are also curve fitted with a third order polynomial:

$$Z_L = b_0 + b_1 t + b_2 t^2 + b_3 t^3 \quad (3-5)$$

$$Z_S = c_0 + c_1 t + c_2 t^2 + c_3 t^3 \quad (3-6)$$

The time derivatives of the continuous Z_L and Z_S functions are the growth rates for the two interfaces:

$$R_L = \frac{\partial}{\partial t} [Z_L(t)] = b_1 + 2b_2 t + 3b_3 t^2 \quad (3-7)$$

$$R_S = \frac{\partial}{\partial t} [Z_S(t)] = c_1 + 2c_2 t + 3c_3 t^2 \quad (3-8)$$

The space derivatives of the continuous thermal profile curves at the interfacial temperature intersections lead to the interfacial thermal gradients:

$$G_L = \frac{\partial}{\partial Z} [T(Z,t)]_{T_L} = [a_1 + 2a_2Z + 3a_3Z^2]_{T_L} \quad (3-9)$$

$$G_S = \frac{\partial}{\partial Z} [T(Z,t)]_{T_S} = [a_1 + 2a_2Z + 3a_3Z^2]_{T_S} \quad (3-10)$$

Note that G_L can be taken as a function of Z_L or t since the two are related through (3-5). The spatial dependence is more useful and is both tabulated and plotted as such. If R_L is computed each time that a thermal profile/liquidus temperature intersection occurs, G_L and R_L can be tabulated at corresponding interfacial locations and therefore cross-plotted. The same is done for R_S vs. G_S .

The interfacial position vs. time relations (3-5) and (3-6) provide two additional useful parameters. The spatial separation of the interfaces at any given time represents the mushy zone height:

$$\Delta Z(t_n) = Z_L(t_n) - Z_S(t_n) \quad (3-11)$$

The time separation of the interfaces at a given level on the mold represents the local solidification time:

$$t_f(Z_k) = t_S(Z_k) - t_L(Z_k) \quad (3-12)$$

where Z_k is chosen to correspond to a known position of either the liquidus or solidus surface at a known time of observation. Thus one of the two points $t_L(Z_k)$ or $t_S(Z_k)$ is known immediately. For example, assume $t_L(Z_k)$ is known, the other point, $t_S(Z_k)$, is determined by solving (inverting) the equation:

$$Z_S(t) = c_0 + c_1t + c_2t^2 + c_3t^3 = Z_k \quad (3-13)$$

3.3 Experimental Results

3.3.1. Thermal Analyses

The results of a typical computerized thermal analysis are shown in Figures 3.3-3.5 for run number G-21 which was for a nominal 2.5 wt.% Hf

level. The initial condition was that the liquidus isotherm was approximately at the Z=0 cm. position on the bar. The lower rate was 5cm./hr. and was held for a distance of 6 cm. At that point the growth rate was accelerated to 25cm./hr. over a transient height of 1 cm. Finally, the high rate was held over a 6 cm. length. This experiment was carried out in the laboratory radiation cooling unit with a 0.15 cm. wall thickness recrystallized Al_2O_3 mold. Note in particular Figures 3.4 and 3.5 which illustrate the thermal gradient, G, and isotherm advance rate, R, values obtained at the positions where transverse microstructural samples were cut.

Experience has shown that the convenient computerized thermal analysis (as it was formulated initially) was accurate only at low and intermediate levels of thermal gradient. For actual thermal gradients exceeding $100^\circ\text{C}/\text{cm.}$, the third order polynomial curve fitting was no longer sufficiently steep and the thermal gradient was underestimated by the previously described PROCES program. The program was replaced by SAFE and SLOPE for high thermal gradient work. The programs allow for the use of fourth order polynomials.

An alternative method has been used, as well, for high thermal gradient runs. The method assumes dynamic steady state such that the mold lowering rate would be equal to the growth rate (note Figure 3.5). Then, the thermal gradient can be computed from the cooling rate as follows (note, also, equation (1-2) in section 1.31):

$$G = \frac{\varepsilon}{R} = \frac{\Delta T}{\Delta t} \frac{\Delta T}{\Delta Z} = \frac{\Delta T}{\Delta Z} \quad (3-14)$$

The thermal gradients computed from the PROCES program and those computed from the observed cooling rates utilizing equation (3-14) are listed for comparison in Table 3.2. In the analyses of experiments that follow, the values of G derived from measured cooling rates are reported for values of $G > 100^\circ\text{C}/\text{cm.}$

Figure 3.6 summarizes the thermal conditions obtained in the runs listed in Tables 3.1-3.3. The thermal measurements were made on samples with nominally 2% Hf addition. Thermal conditions in runs with alloys of other compositions were assumed to be the same as measured for the 2% Hf alloy, under comparable processing conditions. Previous attempts to reproduce thermal conditions in this crystal growth equipment had proved to be extremely reliable.

3.2.2. Carbide Morphology

Micrographs illustrating representative carbide morphologies are presented in Figures 3.7-3.10. The carbides were categorized as coarse or fine and as blocky, script, or transition. Examples of carbides that were categorized as blocky, script, and transition are shown in Figure 3.7 top left, bottom right, and bottom left, respectively.

The data are listed in Table 3.2 and plotted with respect to log G and log R axes in Figures 3.11 and 3.12. Fine carbides are associated with high cooling rates; regions on a log G vs log R plot that are far from the origin. Script carbides were found at low ratios of thermal gradient to growth rate; blocky carbides at high G/R.

3.3.3. Dendrite Arm Spacing Measurements

Micrographs illustrating the primary dendrite morphology in the transverse sections in which the primary dendrite arm spacings were measured are presented in Figures 3.13-3.16. The primary dendrite arm spacings measured for each run are listed in Table 3.2. The data are plotted versus thermal conditions and hafnium content in Figures 3.17-3.19.

Primary dendrite arm spacings are plotted versus cooling rate ($\epsilon \approx GR$) for 0 and 1% Hf samples in Figure 3.17a and for 2 and 2.5% Hf samples in Figure 3.17b. The same line with slope of $-1/3$ on both log-log plots seems to fit the data rather well. However, a line of slope $-1/4$ would give a reasonable fit to the data; and a line of slope $-1/2$ would give a poor fit to the data.

Following the theory of Hunt⁽¹⁾ the primary dendrite arm spacings are plotted versus $GR^{1/2}$ on a log-log axes in Figure 3.18. A line of slope $-1/2$ as would be the relation predicted by the theory is drawn through the data. The fit is adequate but not as close as the surprisingly good fit shown in Figure 3.17.

The effect of hafnium content on primary dendrite arm spacing is explored in Figure 3.19. It appears that at high cooling rates primary dendrite arm spacing is not affected significantly by hafnium content; and at lower cooling rates primary dendrites are refined slightly by the addition of hafnium.

Secondary dendrite arm spacings were measured on longitudinal sections. Secondary dendrite arm features were difficult to discern in grains far from the $\langle 001 \rangle$ growth axis and/or in sections with cooling rates less than 1000°C/hr (18°C/min or 0.3°C/sec). Micrographs illustrating representative sections from which secondary dendrite arm spacings were measured are presented in Figures 3.20-3.23. The data are listed in Table 3.2 and presented in Figures 3.24 and 3.25.

The secondary dendrite arm spacings are plotted versus cooling rate on log-log axes for 0 and 1% Hf in Figure 3.24a and for 2 and 2.5% Hf in Figure 3.24b. The same line with a slope of $-1/3$ is an excellent fit to the data of both plots. However, a line of slope $-1/2$ would give a reasonable fit to the data in Figure 3.24; and a line of slope $-1/4$ would give a poor fit to the data. Previous data on PWA 1418L (the best superalloy data available at the time this project was initiated) showed a slope of $-1/2$. The current work covers a much wider range of cooling rates and reflects the better statistics and the significant improvement in technique which occurred during this program.

The influence of hafnium content on secondary dendrite arm spacings is explored in Figure 3.25. As observed with regard to primary dendrite spacing, secondaries are refined by hafnium additions at low cooling rates and are not significantly affected by hafnium at higher cooling rates.

3.3.4. Eutectic Volume Fraction

Micrographs of samples etched to show the morphology and amount of the eutectic constituent are presented in Figures 3.26-3.29. The measured volume percent of eutectic data are listed Table 3.2. The volume percent eutectic data are plotted versus the hafnium content in Figure 3.30 and versus cooling rate in Figure 3.31.

The eutectic constituent increases as the hafnium content is increased from about 5% eutectic with no hafnium addition to about 20% eutectic with 2.5% hafnium addition. The variability in the as cast eutectic constituent is apparent at all hafnium contents except 1%. At 0% Hf the variability in eutectic is seen to be related to cooling rate. Slow cooling rates result in decreased amounts of eutectic. At 2 and 2.5% Hf the eutectic constituent varies $\pm 5\%$. The variation indicated in Figure 3.31 is not simply related to cooling rate.

3.4 Discussion

The achievement of extreme rate-gradient combinations was accomplished according to plan. Low thermal gradients were difficult to achieve in laboratory scale equipment as this is contrary to the design of crystal growth equipment. The lowest steady thermal gradients were achieved by using thick porous shell molds, insulating wraps, low hot zone temperatures, high tin temperatures and/or radiation cooling. High thermal gradients were obtained by using this fully dense mold materials, profiled hot zones, high hot zone temperature, LMC and low tin temperatures. The cooling rate was primarily controlled by the selection of a suitable mold lowering rate. Ther thermal analysis verified that the growth rate followed the mold lowering rate very closely. Near steady-state conditions were achieved at the desired two locations in each bar.

Computer aided thermal analyses (modified as described in Section 3.3.1.) worked well for thermal gradients up to $200^{\circ}\text{C}/\text{cm}$. Computed gradients were consistent with gradients directly obtained from cooling rate instruments.

The data presented herein define the influence of thermal conditions (G,R, ϵ) on carbide type and size, dendrite arm spacing, and eutectic volume fraction for MAR-M200 and MAR-M200 with various amounts of hafnium. These baseline data should enable better control of D.S. casting processes and post-facto analysis of cast structures. The data herein could be used to set aims for castings process parameters directed at quantitatively achieving a desired microstructure. Alternatively, solidification conditions in a production or developmental casting could be determined by analyzing the microstructure and comparing the behavior

to that found in this study. This has already been accomplished to solve several production problems. For example, cooling rates ($\epsilon = GR$) could be approximated based on dendrite arm spacing measurements and from carbide size. The ratio G/R could be bracketed using Figure 3.12 for carbide type.

The observed slope (power dependence) of about -0.33 for log primary dendrite spacing versus log cooling rate would become +0.33 on a log-log plot of primary dendrite spacing versus local solidification time. This data is comparable to previously determined data for P.W.A. 1418L which, over a limited range, yielded a slope of +0.29. Although the power dependence of primary spacings was found to be the same as for secondary arms, it is probable the mechanisms controlling these spacings are different.

The influence of hafnium in reducing primary and secondary spacings at low cooling rates may be due to low diffusivity for Hf influencing the kinetics of dendrite coarsening. The overall effect of Hf on solution kinetics and properties, however, cannot be predicted directly from this result.

The volume percent of eutectic constituent increases by 5-6% for each 1% addition of hafnium. For MAR-M200 with no hafnium the percent eutectic increases from about 20% at a cooling rate of 300°C/hr to about 5% at a cooling rate of 10,000°C/hr. With additions of Hf over 1% the scatter in data prevents determination of the effect of cooling rate on eutectic fraction. The origin of the scatter is discussed again in Chapter 7.0.

Table 3.1: Mold/Cooling Combinations

<u>Run No</u>	<u>Mold Type</u>	<u>Cooling</u>	<u>T Hot Zone</u>	<u>T Bath</u>	<u>Group ID</u>
G-18, G-25, G-30, G-34, G-36, G-3	Dense	LMC	1650°C	250°C	1
G-20, G-24, G-31, C-6	Porous	LMC	1490°C	350°C	2
G-21, G-32, G-29, C-2	Dense	HRS	1625°C	--	3
G-27, G-28, G-29, C-2	Porous w/ Fiberfrax	HRS	1500°C	--	4
G-22	Dense	LMC	1480°C	350°C	--
G-23	Porous	LMC	1650°C	250°C	--
G-26	Porous w/ 1/2 Fiberfrax	HRS	1540°C	--	--

Code:

Dense = Recrystallized Alumina

Porous = Alumina/Silica Shell Mold

LMC = Liquid Metal Cooling

HRS = High Rate Solidification (Radiation Cooling)

Fiberfrax = Mold Wrapped with 1/2" Thick Fiberfrax Blanket

TABLE 3.2: SUMMARY OF THERMAL CONDITIONS AND MICROSTRUCTURAL FEATURES

Run No.	w/o Hf	Rate cm/hr	Gradient		Gradient from		Cooling Rate °C/hr	Primary Dendrite Spacing μm	Secondary Dendrite Spacing μm	Carbide Type	Eutectic Vol %
			Gradient (Computer) °C/cm	Cooling Rate °C/cm							
G-18B	2.5	5	119	195	200	976	204	50	21.4	Blocky	21.5
G-18T	2.5	100	119	200			92.5	21.4		Script	21.1
G-20B	2.5	5	75	81	100	408	240	66.6	24.6	Blocky	15.1
G-20T	2.5	50	75	100			118	24.6		Script	20.9
G-21B	2.5	5	101	164	92	824	289	51.6	34	Transition	16.9
G-21T	2.5	25	88	92			186	34		Script	16.9
G-22B	2.5	5	73	106	127	532	289	64	29	Blocky	16.6
G-22T	2.5	50	88	127			144	29		Transition	20.0
G-23B	2.5	5	109	158	96	792	248	40	26	Blocky	23.7
G-23T	2.5	100	105	96			151	26		Script	21.3
G-24B	2.0	5	75*	81*	100*	408*	257	62.5	27.3	Blocky	15.9
G-24T	2.0	50	75*	100*			144	27.3		Transition	17.3
G-25B	2.0	5	119*	195*	200*	976*	226	66.6	23.5	Blocky	20.1
G-25T	2.0	100	119*	200*			120	23.5		Script	19.7
G-26B	2.5	20	65	96	48	1,928	256	44	54	Script	24.8
G-26T	2.5	20	72	48			363	54		Script	22.2
G-27B	2.5	10	42	48.4	24	484	312	75	56	Script	20.1
G-27T	2.5	40	34	24			304	56		Script	17.3
G-28B	2.0	10	42*	48*	24*	484*	363	77	62.3	Script	20.7
G-28T	2.0	40	34*	24*			320	62.3		Script	19.7

* Assumed Values of duplicated run conditions

Run No.	w/o Hf	Rate cm/hr	Gradient		Gradient from		Cooling Rate °C/hr	Primary Dendrite Spacing μm	Secondary Dendrite Spacing μm	Carbide Type	Eutectic Vol %
			(Computer) °C/cm	Cooling Rate °C/cm	Cooling Rate °C/cm						
G-29B	1.0	10	42*	48*	484*	928*	363	56.6	55	Blocky	11.6
G-29T	1.00	40	34*	24*			320				
G-30B	1.0	5	119*	195*	976*	20,040*	215	74.7	21.5	Blocky	11.4
G-30T	1.0	100	119*	200*			85	Script		10.9	
G-31B	1.0	5	75*	81*	408*	5,040*	363	79.3	35.4	Blocky	11.9
G-31T	1.0	50	75*	100*			226	Script		11.3	
G-32B	2.0	5	101*	164*	824*	2,304*	257	90	48	Transition	13.2
G-32T	2.0	25	88*	92			178	Transition		14.1	
G-33B	1.0	5	101*	164*	824*	2,304*	302	101.9	42.6	Blocky	11.3
G-33T	1.0	25	88*	92*			245	Transition		11.5	
G-35B	2.0	100	119*	200*	20,040*	976*	120	20.3	70.5	Script	17.4
G-35T	2.0	5	119*	195*			240	Blocky		15.3	
G-36B	2.0	300	119*	195*	60,000*	100,000*	49	12	22.5	Blocky	12.2
G-36T	2.0	600	119*	200*			68	Blocky		8.7	
C-1B	0.0	5	101*	164*	824*	2,304*	249	52.8	37.8	Transition	3.6
C-1T	0.0	25	88*	92*			207	Transition		4.2	
C-2B	0.0	10	42*	48*	484*	928*	310	104	50.1	Blocky	1.9
C-2T	0.0	40	34*	24*			320	Transition		1.6	
C-3B	0.0	5	119*	195*	976*	20,040*	200	64	25	Blocky	1.7
C-3T	0.0	100	119*	200*			105	Script		4.1	
C-6B	0.0	5	80	111	535	6,540	384	105	37.7	Blocky	1.9
C-6T	0.0	50	105	129			192	Script		5.6	

* Assumed Values of duplicated run conditions

Table 3.3: Plotting Symbol - Run Identification for Growth Rate
Vs. Gradient + Cooling Rate Vs. S_1 or S_2 Plots

<u>Group ID</u>	<u>Run No.</u>	<u>Symbol</u>	<u>Letter</u>
1	G-18	○	A
1	G-25	○	B
1	G-30	○	C
1	G-35	○	D
1	G-3	○	E
2	G-20	□	F
2	G-24	□	G
2	G-31	□	H
2	C-6	□	I
3	G-21	△	J
3	G-32	△	K
3	G-33	△	L
3	C-1	△	M
4	G-27	◇	N
4	G-28	◇	O
4	G-29	◇	P
4	C-2	◇	Q
--	G-22	⊙	R
--	G-23	◇	S
--	G-26	◊	T
--	G-36	D	U

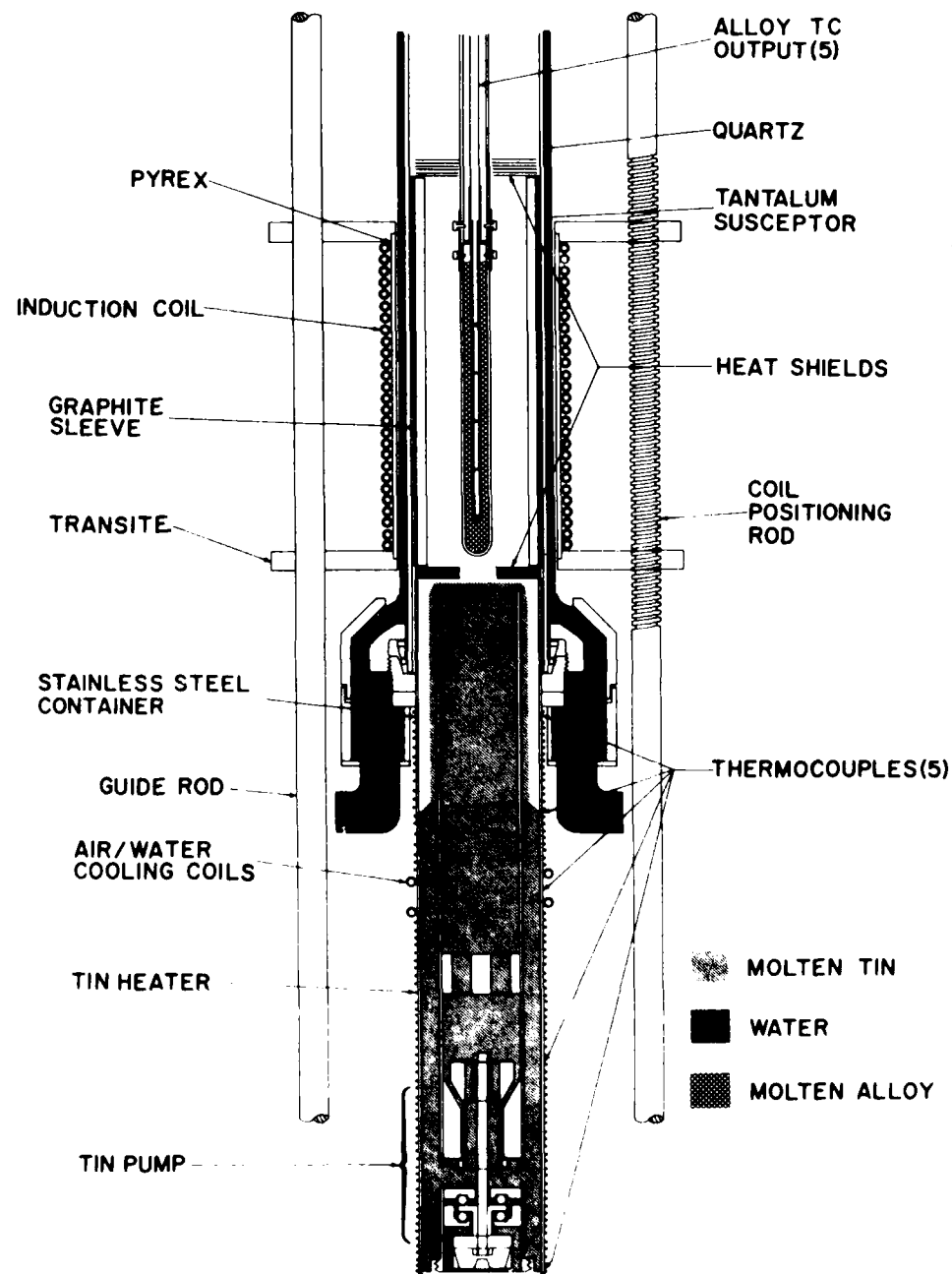


Figure 3.1 Laboratory liquid metal cooling apparatus.

Transient Specimen Layout

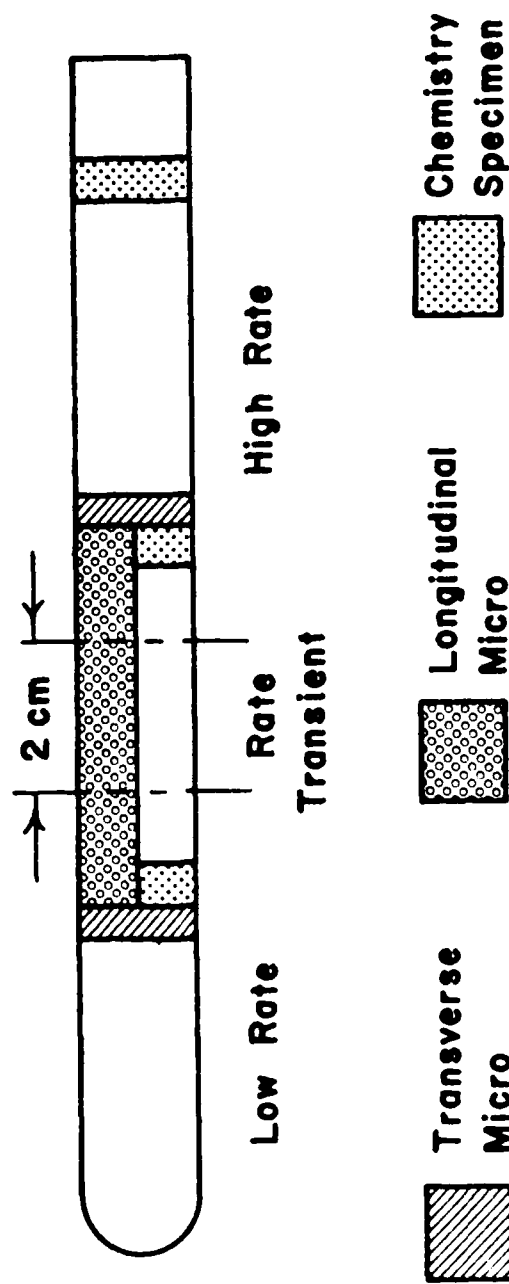


Figure 3.2: Procedure for cutting metallographic and chemistry specimens from LMC bars.

1. TEMPERATURE VS. TIME

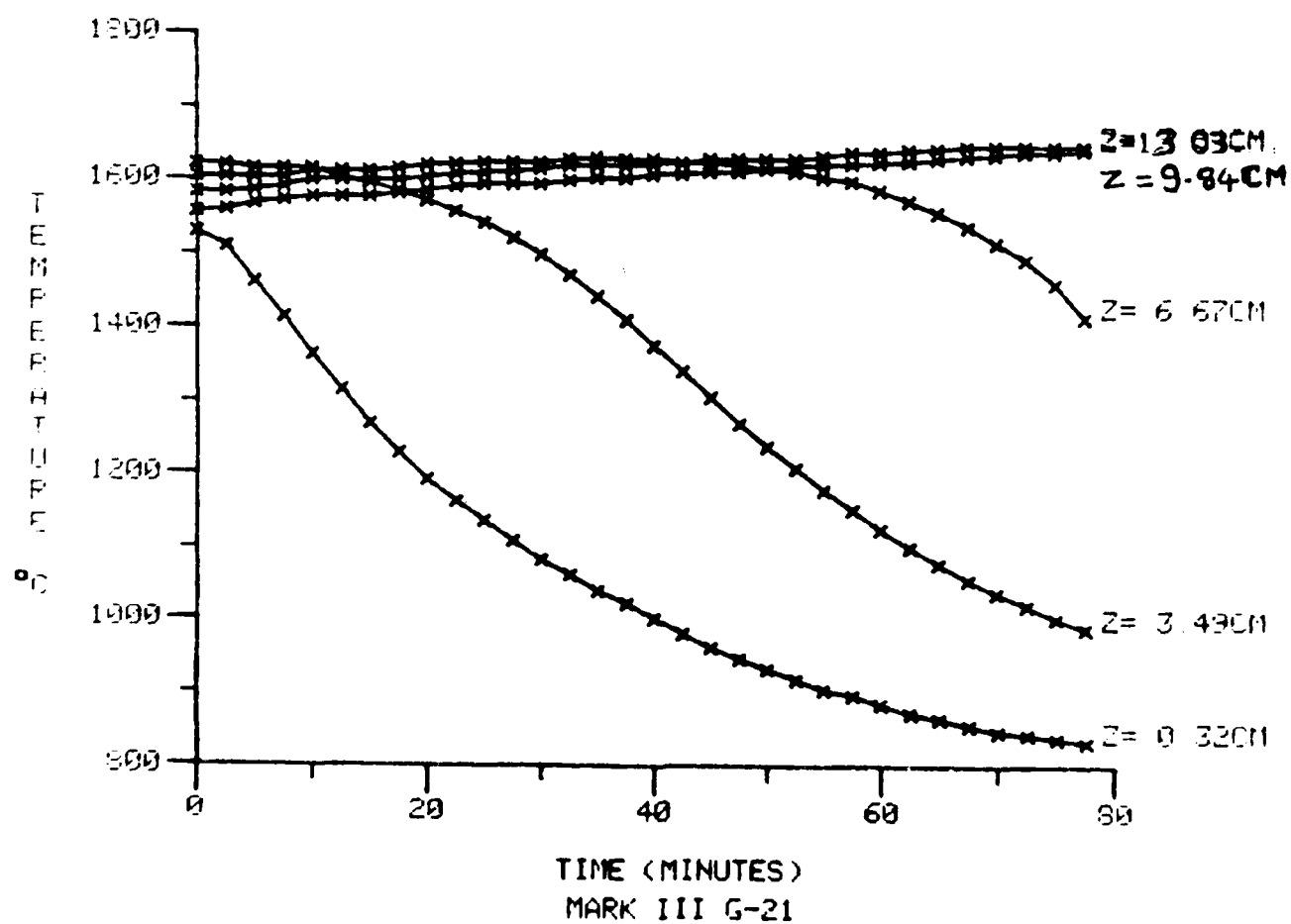


Figure 3.3a: Cooling curves for low rate section of run G-21.

2. TEMPERATURE VS. LENGTH

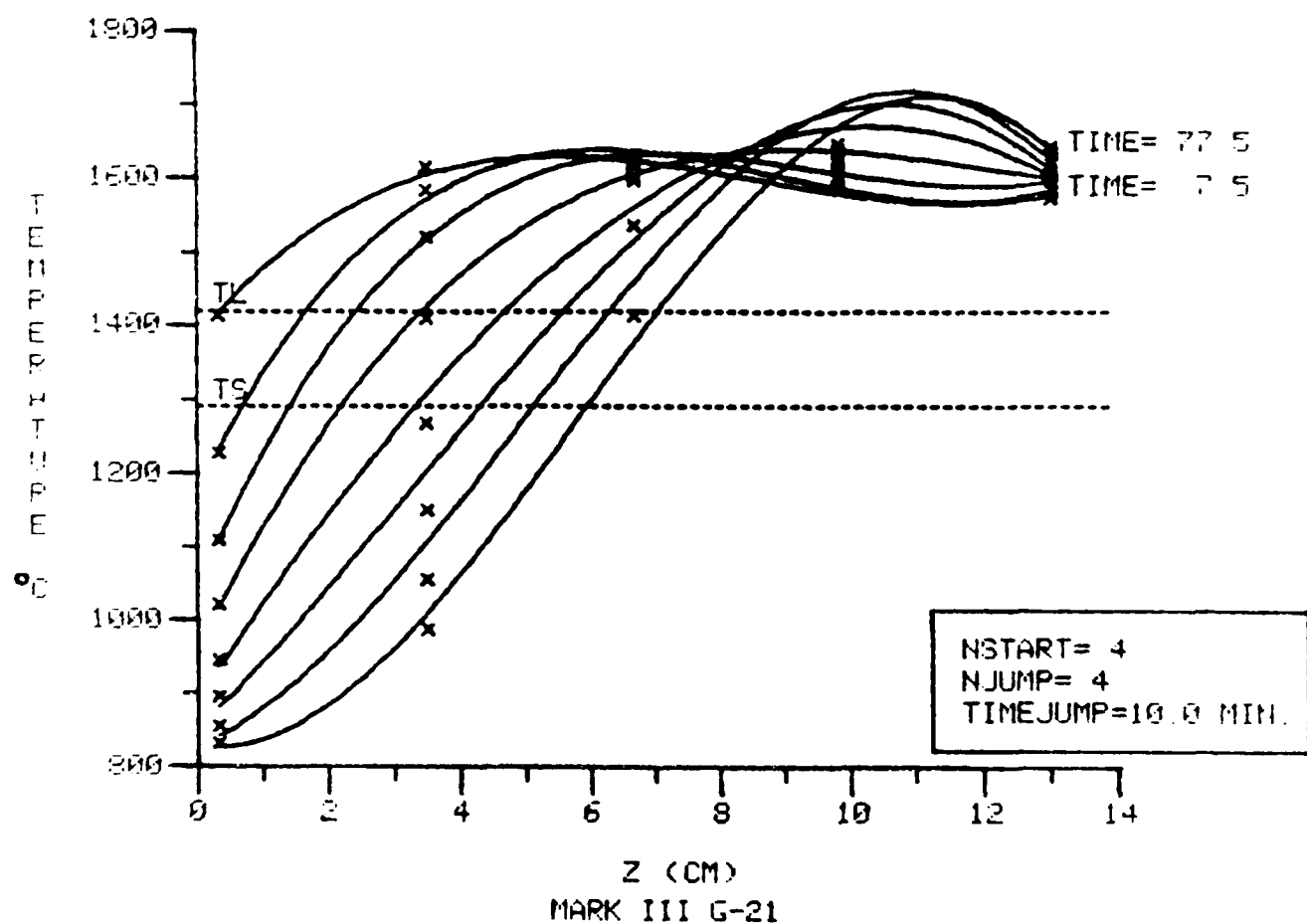


Figure 3.3b: A portion of the thermal profiles for low rate section of run G-21.

3. LIQUIDUS GRADIENT VS. LIQUIDUS POSITION
SOLIDUS GRADIENT VS. SOLIDUS POSITION

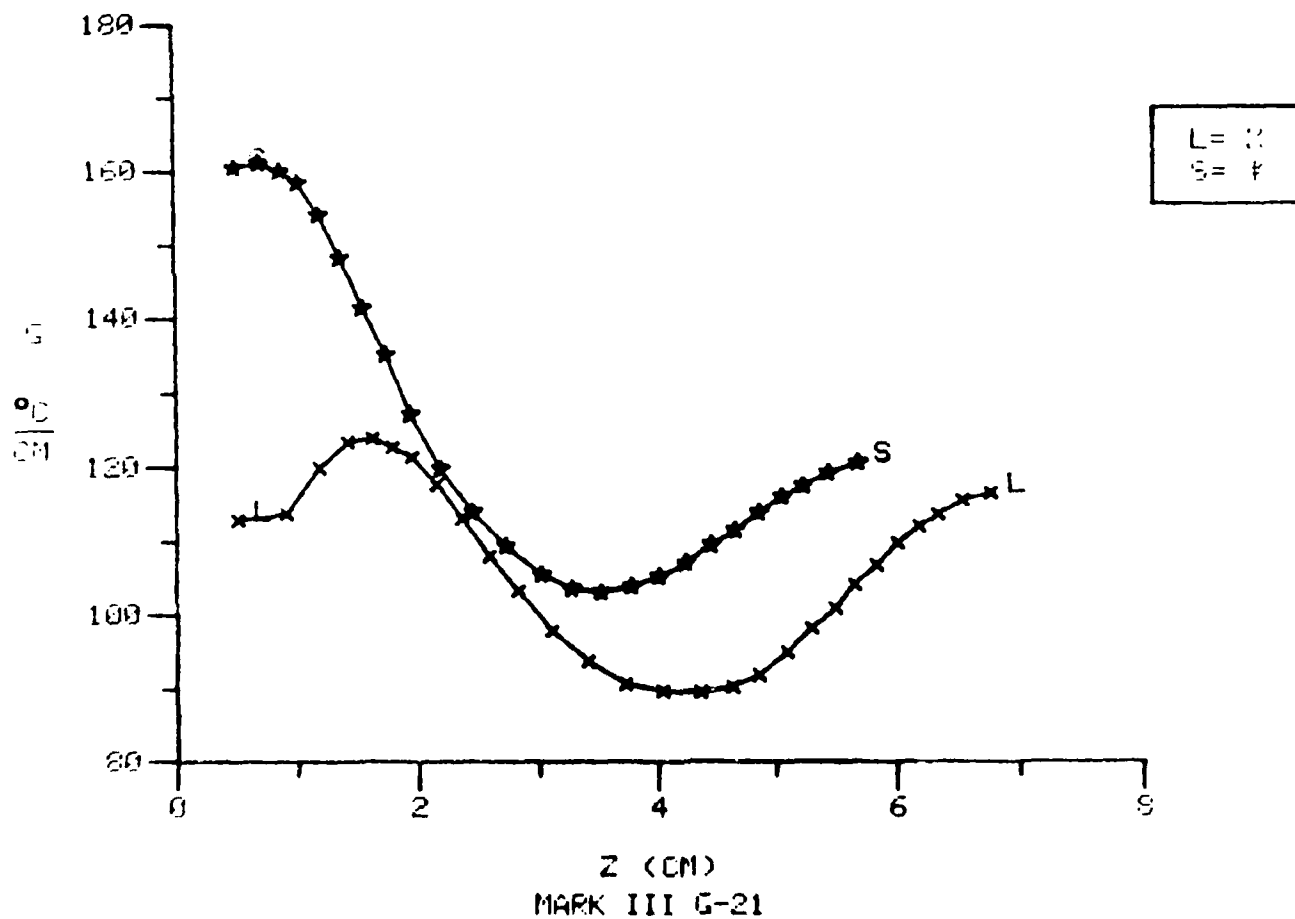


Figure 3.3c: Thermal gradient vs. distance plots for low rate section of G-21.

4. LIQUIDUS POSITION VS. TIME
SOLIDUS POSITION VS. TIME

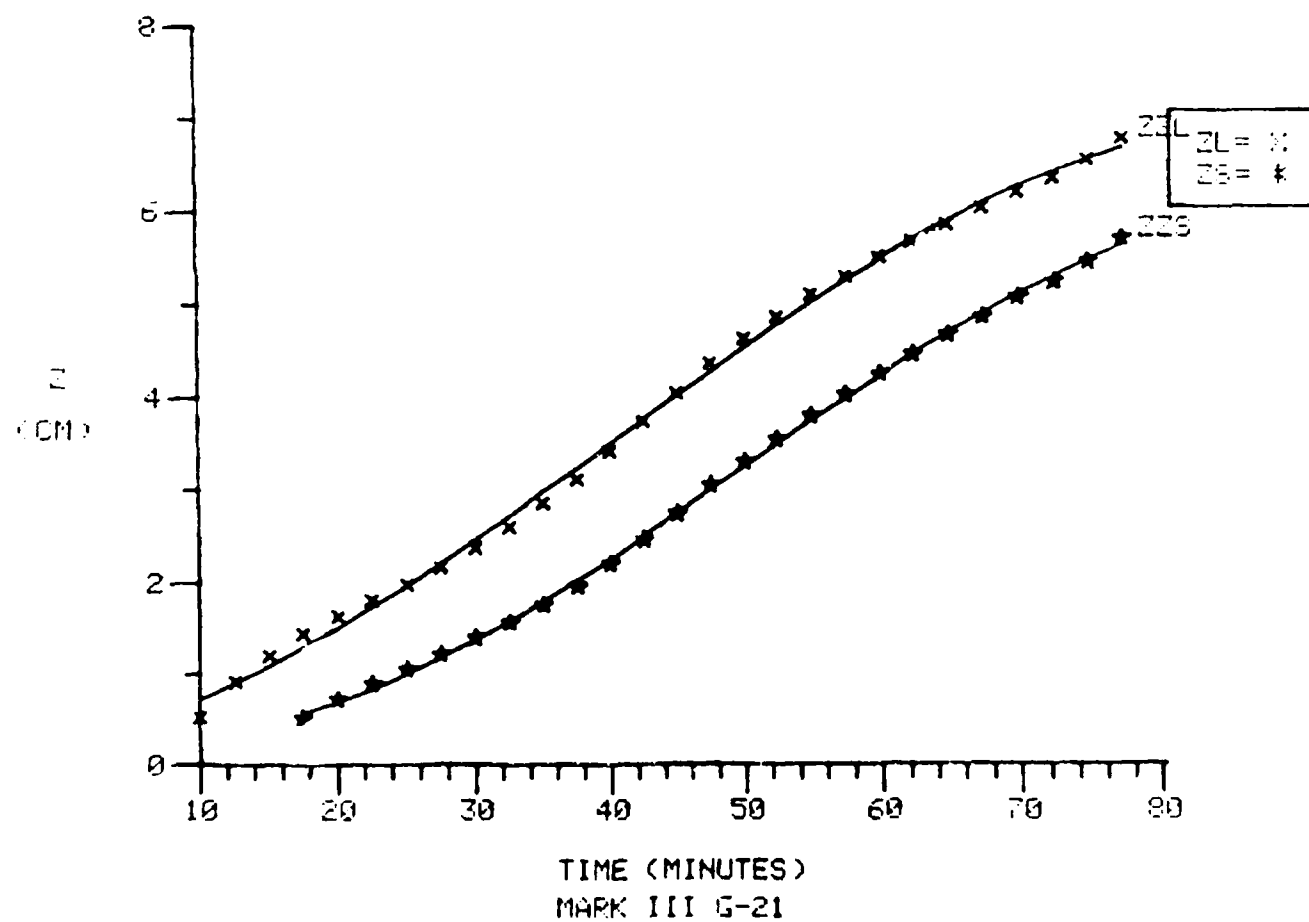


Figure 3.3d: Distance vs. time curves for low rate section of G-21.

5. LIQUIDUS GROWTH RATE VS. LIQUIDUS POSITION
SOLIDUS GROWTH RATE VS. LIQUIDUS POSITION

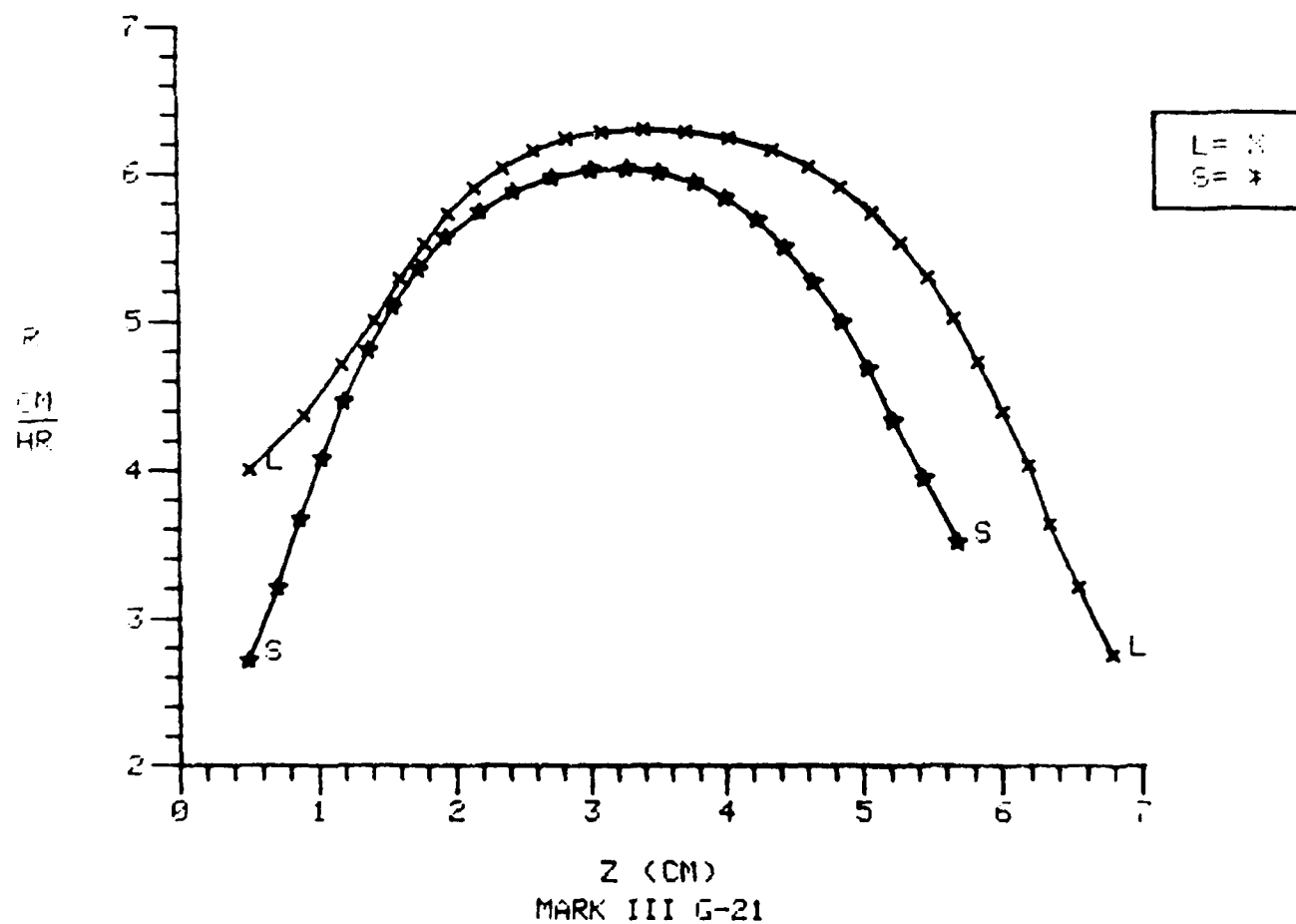


Figure 3.3e: Growth rate distance curves for liquidus and solidus interfaces during low rate portion of G-21.

6. LIQUIDUS GROWTH RATE VS. LIQUIDUS GRADIENT
SOLIDUS GROWTH RATE VS. SOLIDUS GRADIENT

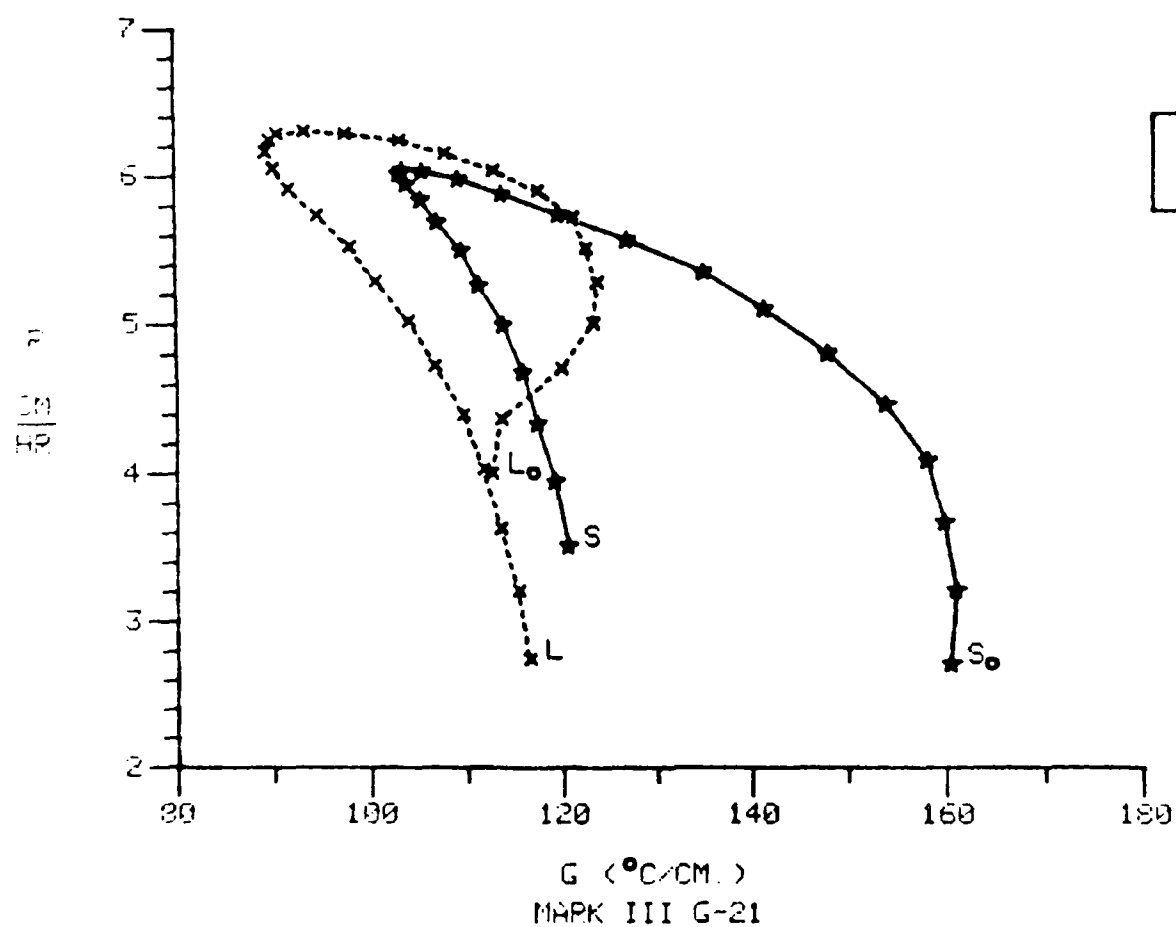


Figure 3.3f: Rate-Gradient map for lower end of G-21. S₀ denotes the beginning of the solidus points.

7. MUSHY ZONE WIDTH VS. TIME

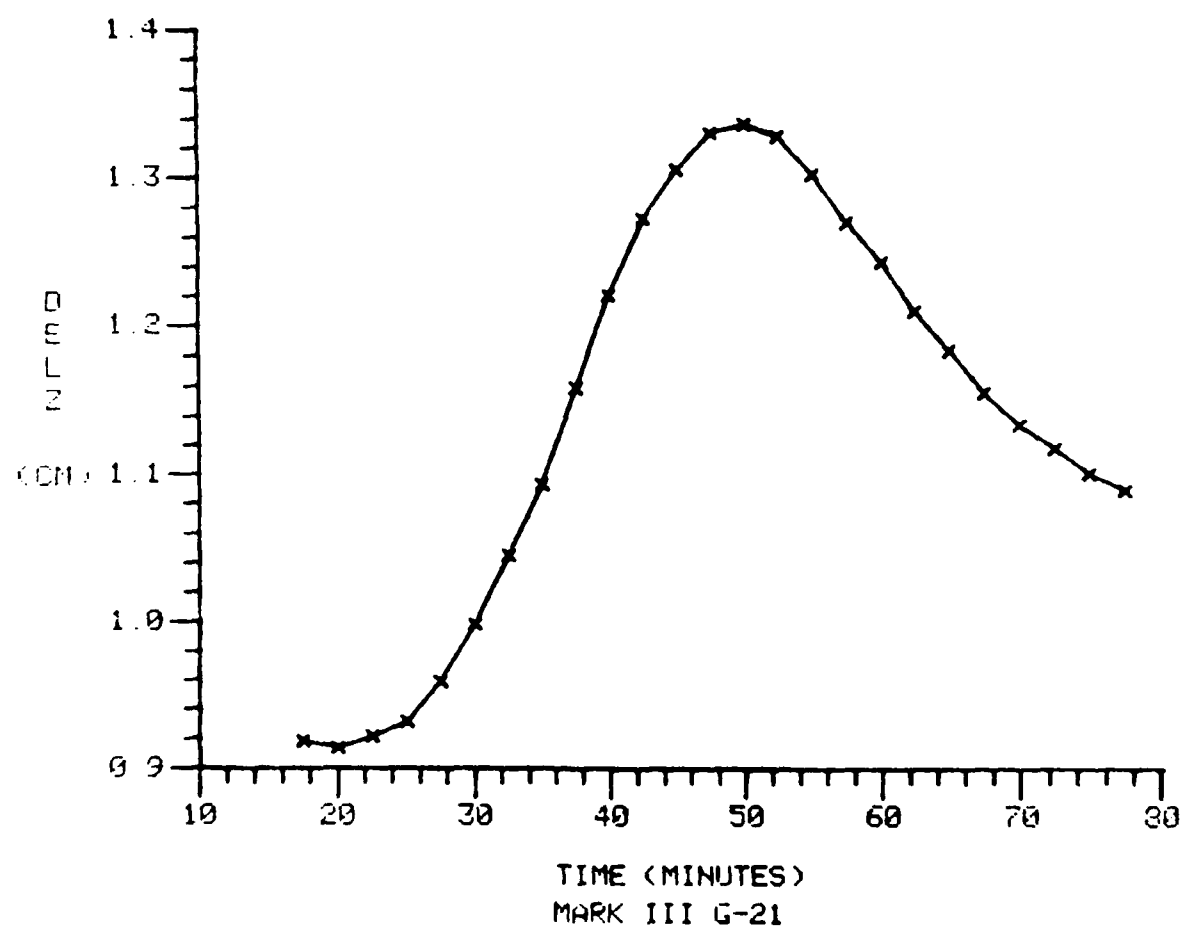


Figure 3.3g: Mushy-zone height vs. time plot for low rate section of G-21.

8. LOCAL SOLIDIFICATION TIME VS. DISTANCE

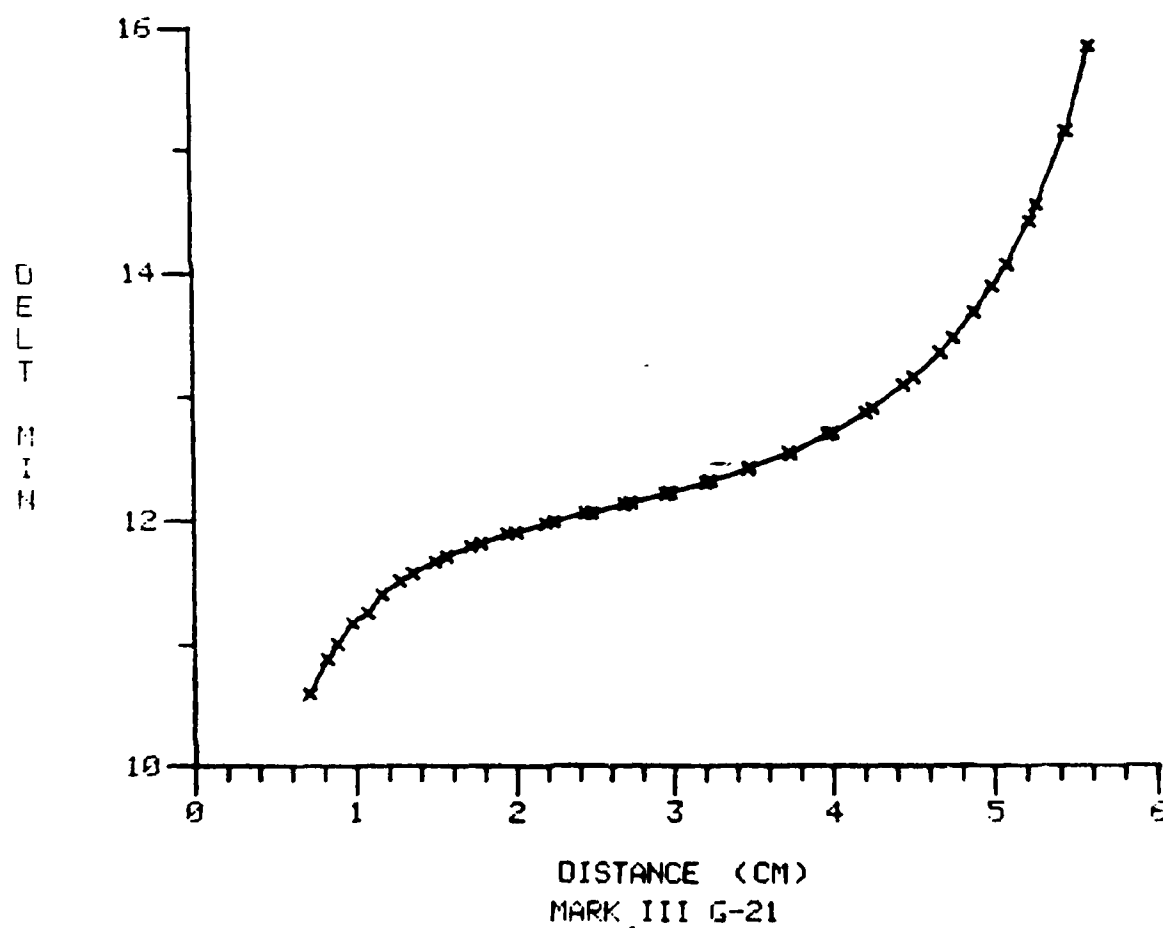


Figure 3.3h: Local solidification time vs. distance plot for bottom end of run G-21.

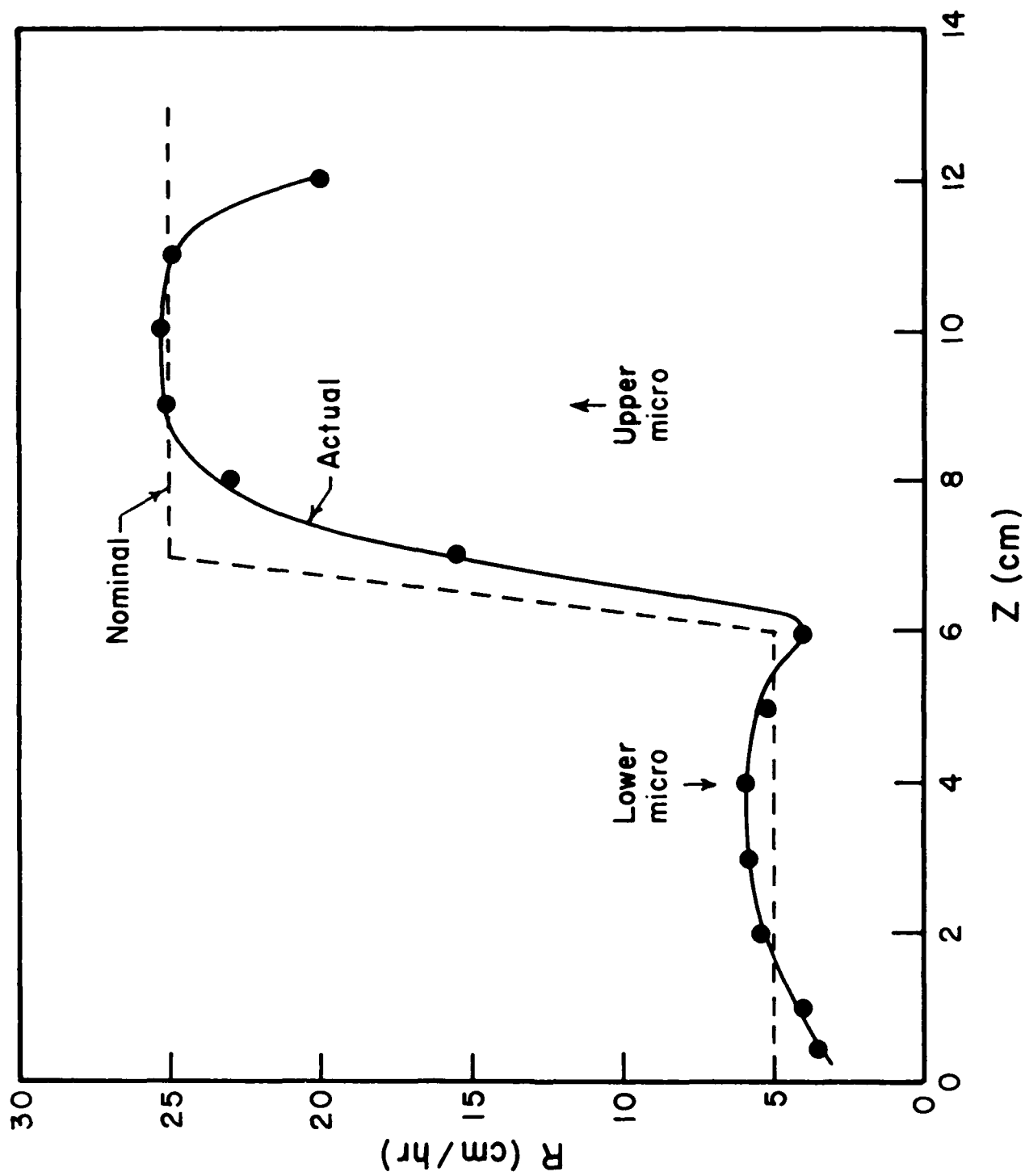


Figure 3.4: Average of liquidus and solidus growth rates vs. position on run G-21. Nominal rates and transverse micro locations are also indicated.

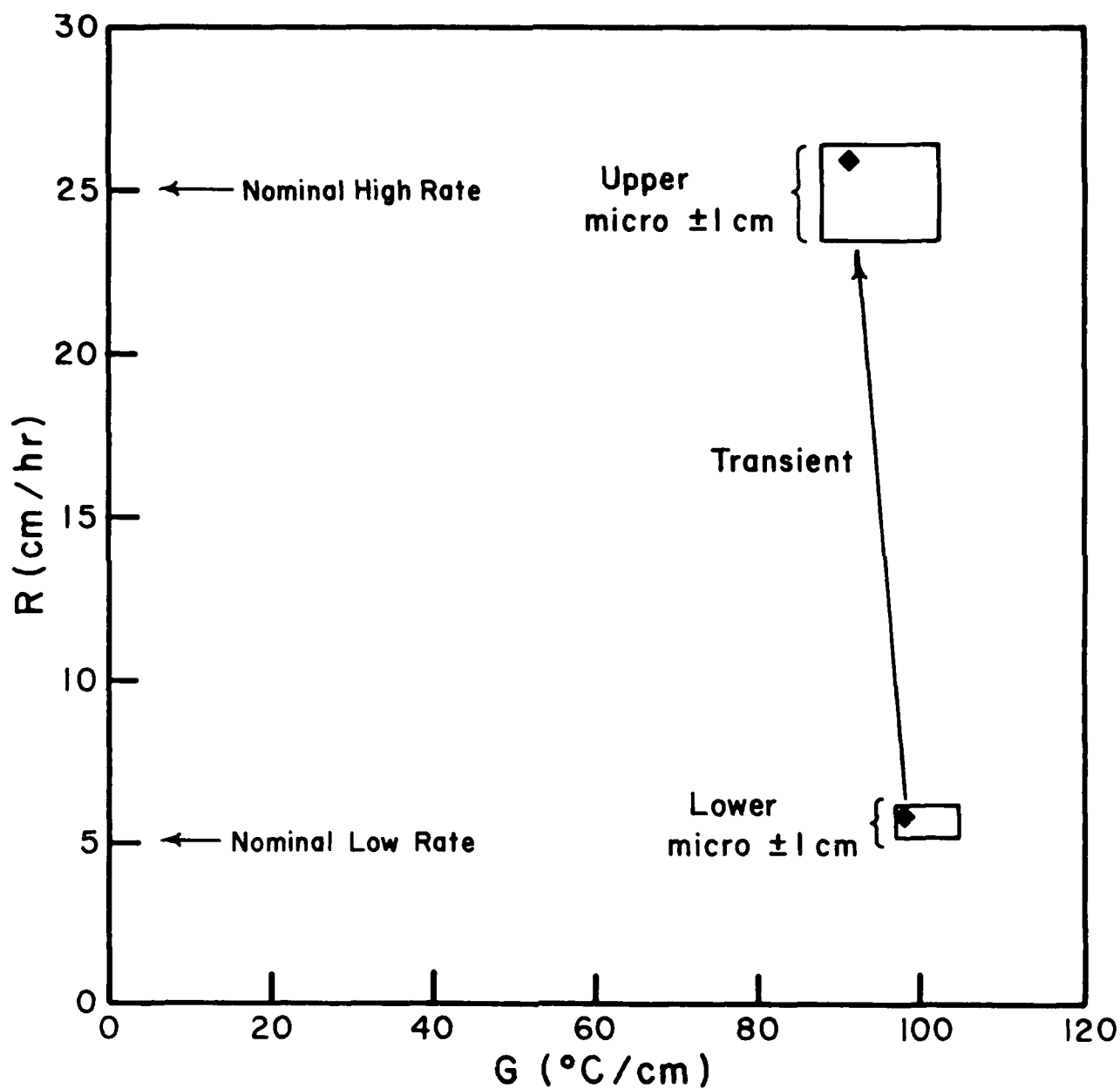


Figure 3.5: Combined rate-gradient map for G-21 showing average liquidus and solidus growth rates and thermal gradients within 1 cm. of exact transverse micro locations (diamond). Results are from computerized thermal analysis.

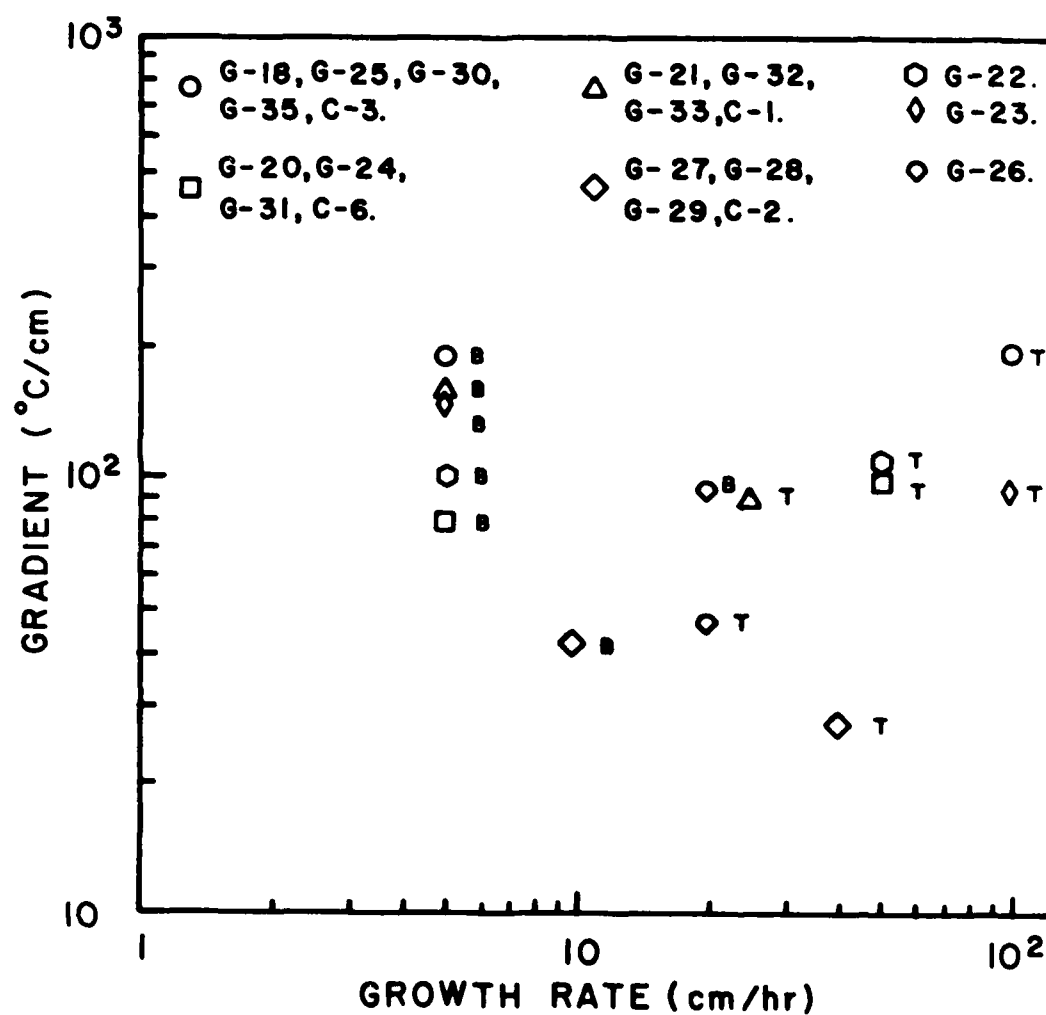


Figure 3.6: Log - log plot of thermal conditions associated with upper and lower micro locations (high and low growth rate, respectively). Refer to Tables 3.1 and 3.3 for code.

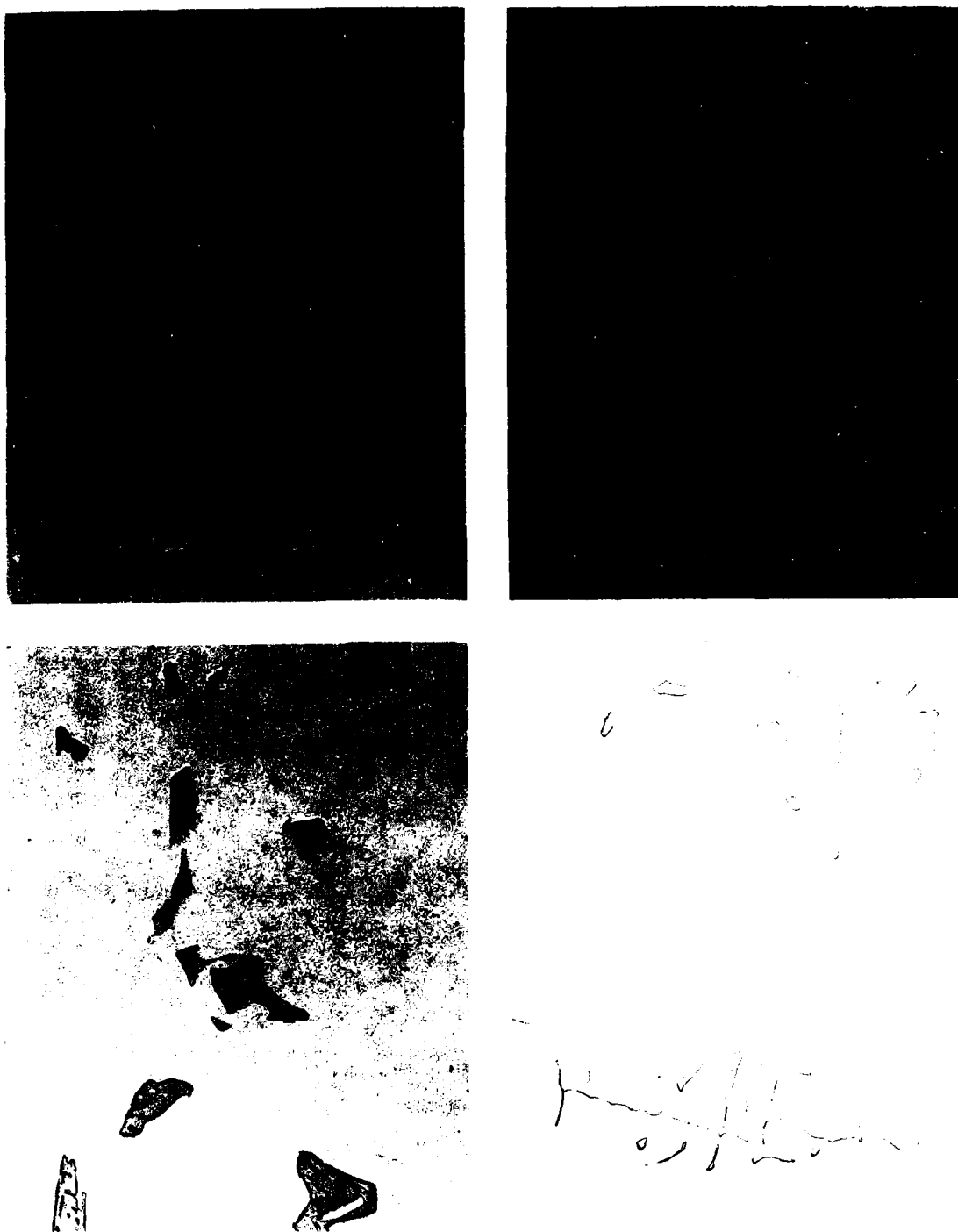


Figure 3.7: Photomicrographs selected to show the range of variation of carbide morphology in unmodified MAR-M200 (unetched, 500 X). Top left: C-3B, high G, low R, high G/R. Top right: C-3T, high G, high R, high ϵ . Bottom left: C-2B, low G, low R, low ϵ . Bottom right: C-2T, low G, high R, low G/R.



Figure 3.8: Photomicrographs selected to show the range of variation of carbide morphology in Mar-M200 + 1% Hf (unetched, 500X). Top left: G-30B, high G, low R, high G/R. Top right: G-30T, high G, high R, high ϵ . Bottom left: G-29B, low G, low R, low ϵ . Bottom right G-29T, low G, high R, low G/R.

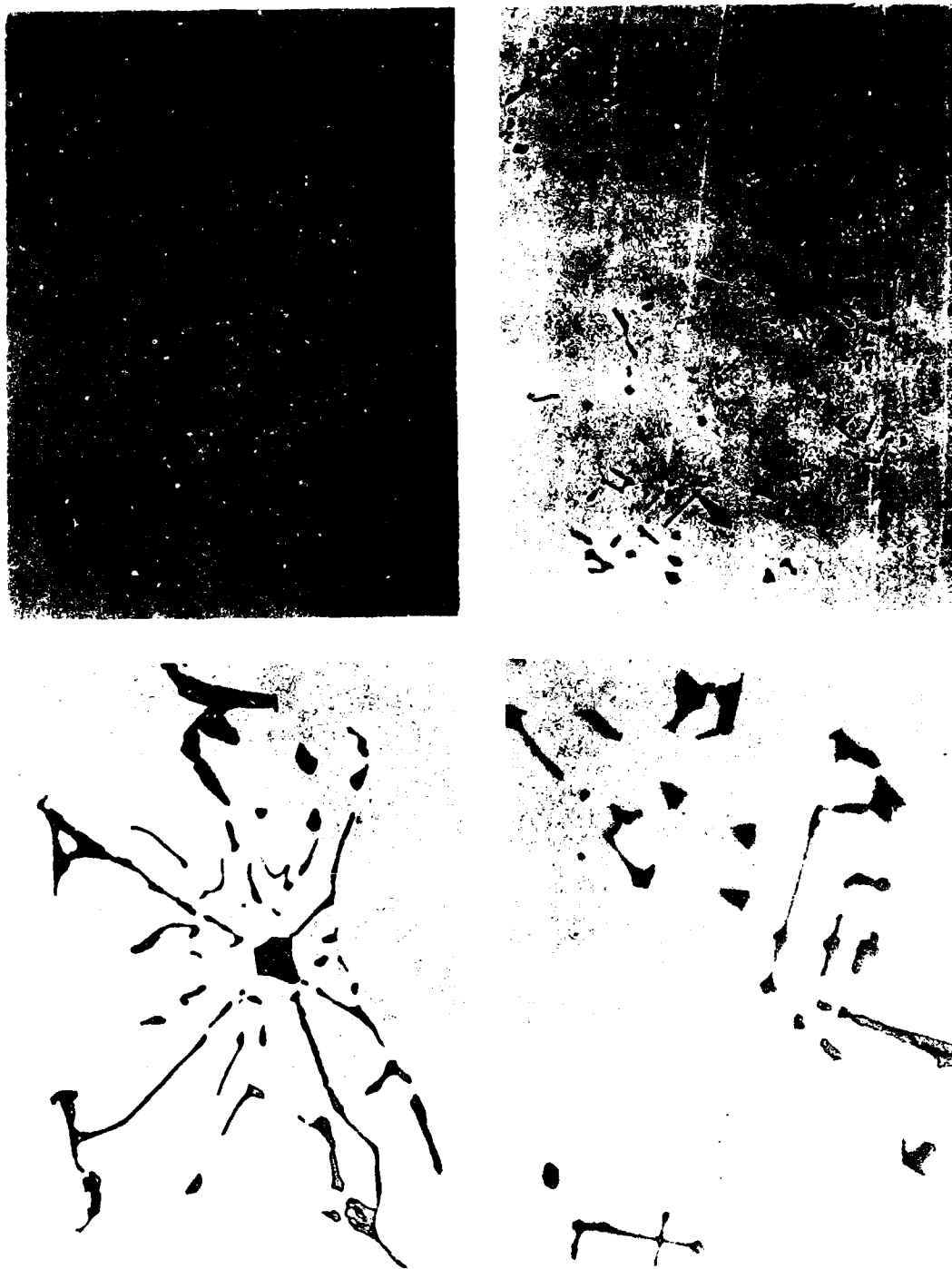


Figure 3.9: Photomicrographs selected to show the range of variation of carbide morphology in Mar-M200 + 2% Hf (unetched, 500X). Top left: G-25B, high G, low R, high G/R. Top right: G-25T, high G, high R, high ϵ . Bottom left: G-28B, low G, low R, low ϵ . Bottom right G-28T, low G, high R, low G/R.

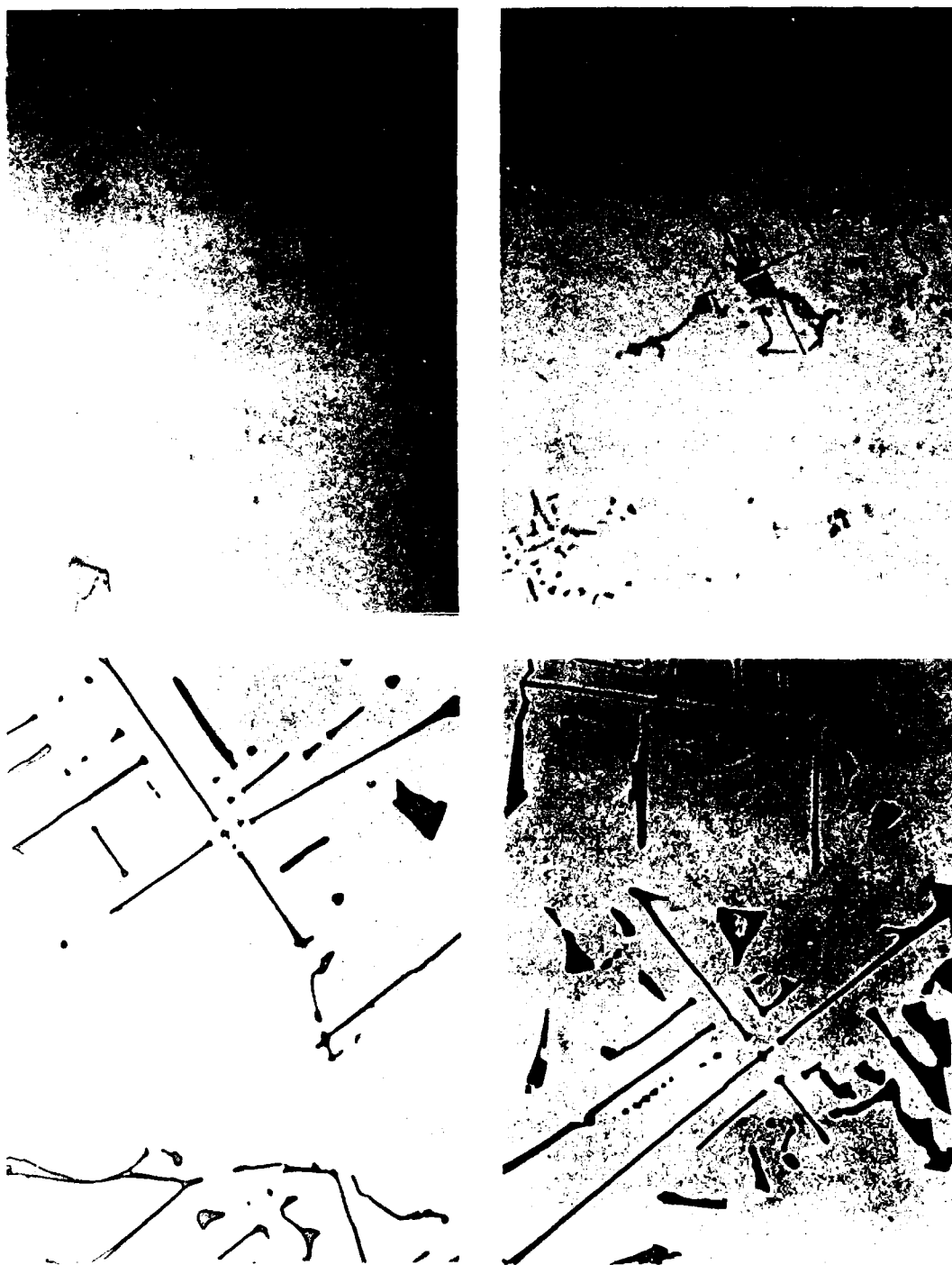


Figure 3.10: Photomicrographs selected to show the range of variation of carbide morphology in Mar-M200 + 2.5% Hf (unetched, 500X). Top left: G-18B, high G, low R, high G/R. Top right: G-18T, high G, high R, high ϵ . Bottom left: G-27B, low G, low R, low ϵ . Bottom right: G-27T, low G, high R, low G/R.

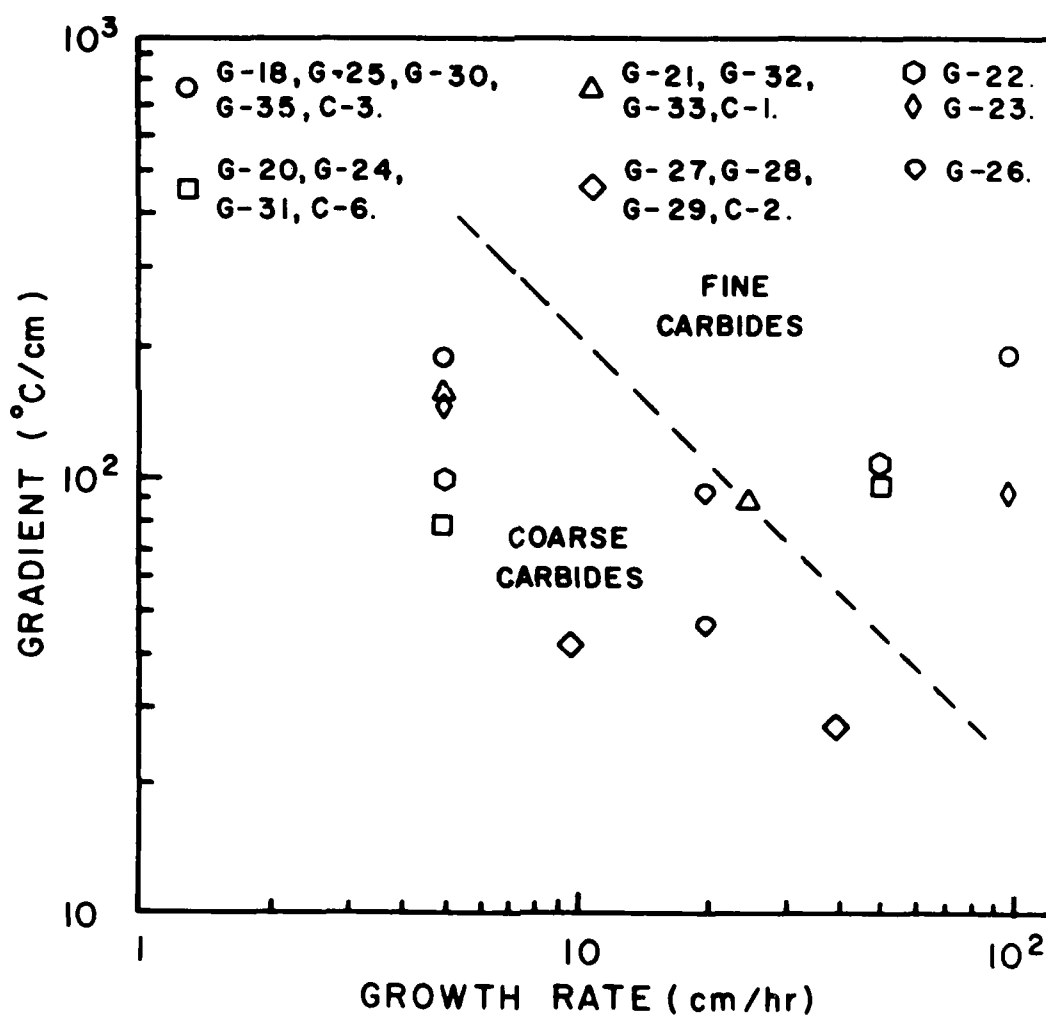


Figure 3.11: Arbitrary transition from coarse to fine carbides at $\epsilon = R \times G = 2400^\circ\text{C/hr}$. Refer to Tables 3-1 and 3-3 for meaning of symbols.

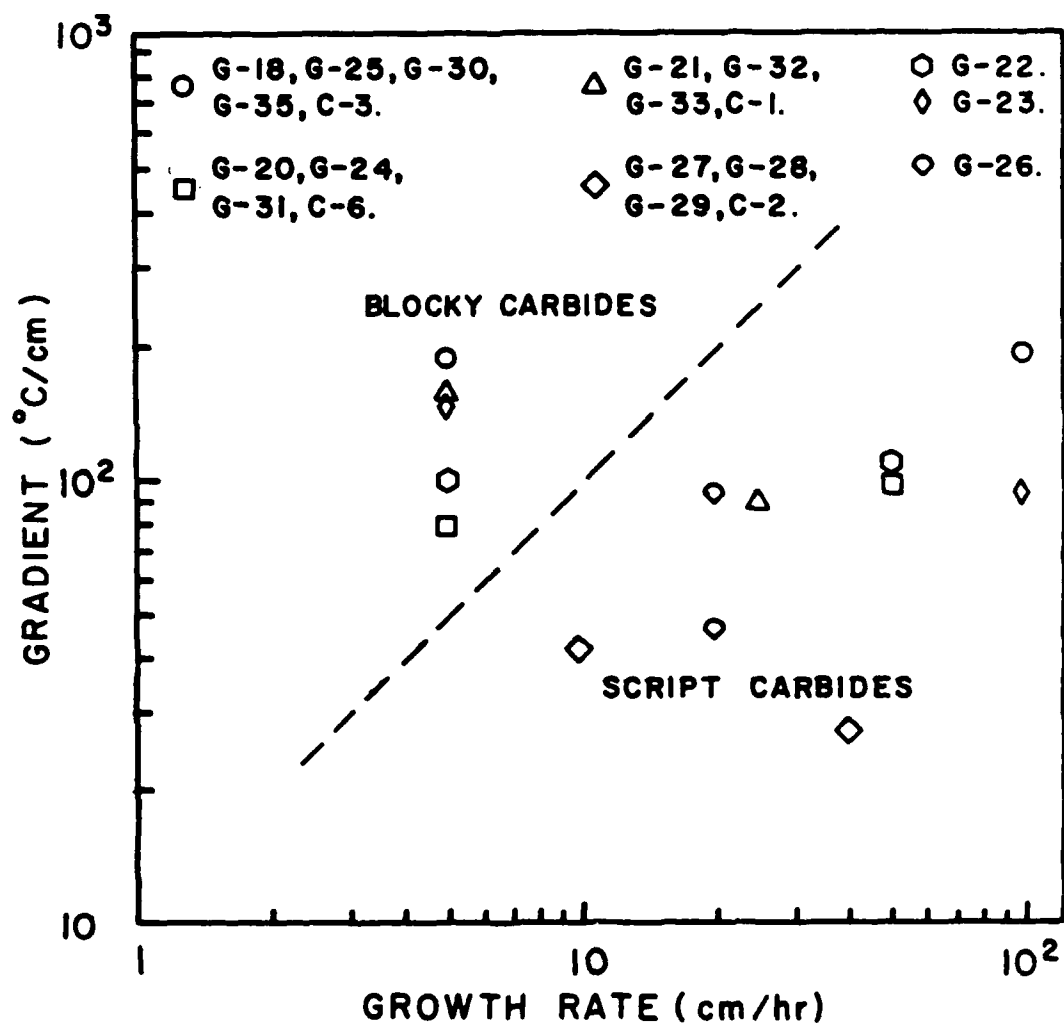


Figure 3.12: Probable blocky/script transition for MC carbides at $G/R = 10^\circ\text{C hr/cm}^2$.

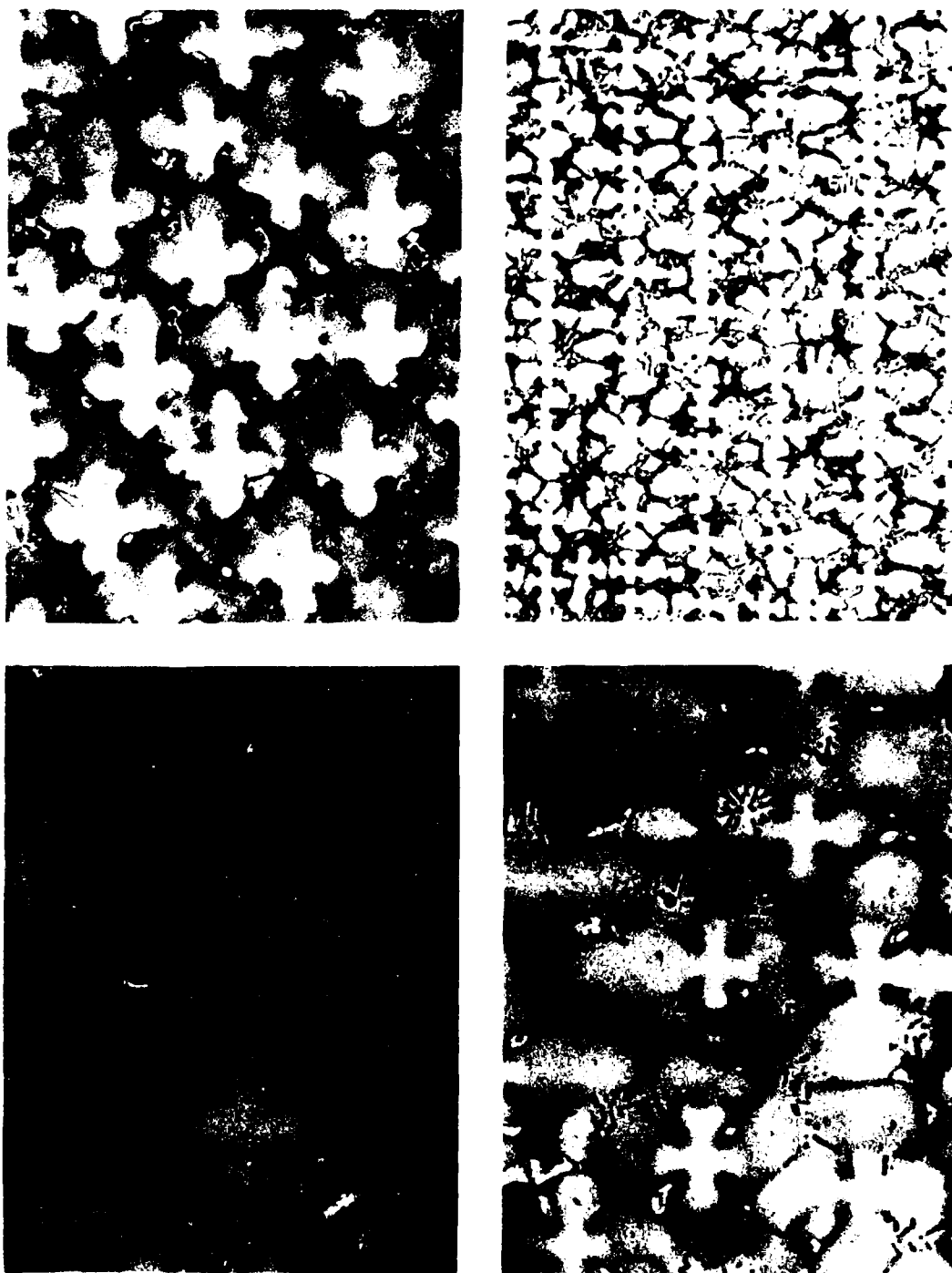


Figure 3.13: Photomicrographs of sections transverse to heat flow typical of samples analyzed to determine primary dendrite arm spacing in unmodified Mar-M200 (50% lactic acid, 33% HCl, 17% HNO₃, 100x). Top left: C-3B, high G, low R, high G/R. Top right: C-3T, high G, high R, high ϵ . Bottom left: C-2B, low G, low R, low ϵ . Bottom right: C-2T, low G, high R, low G/R.

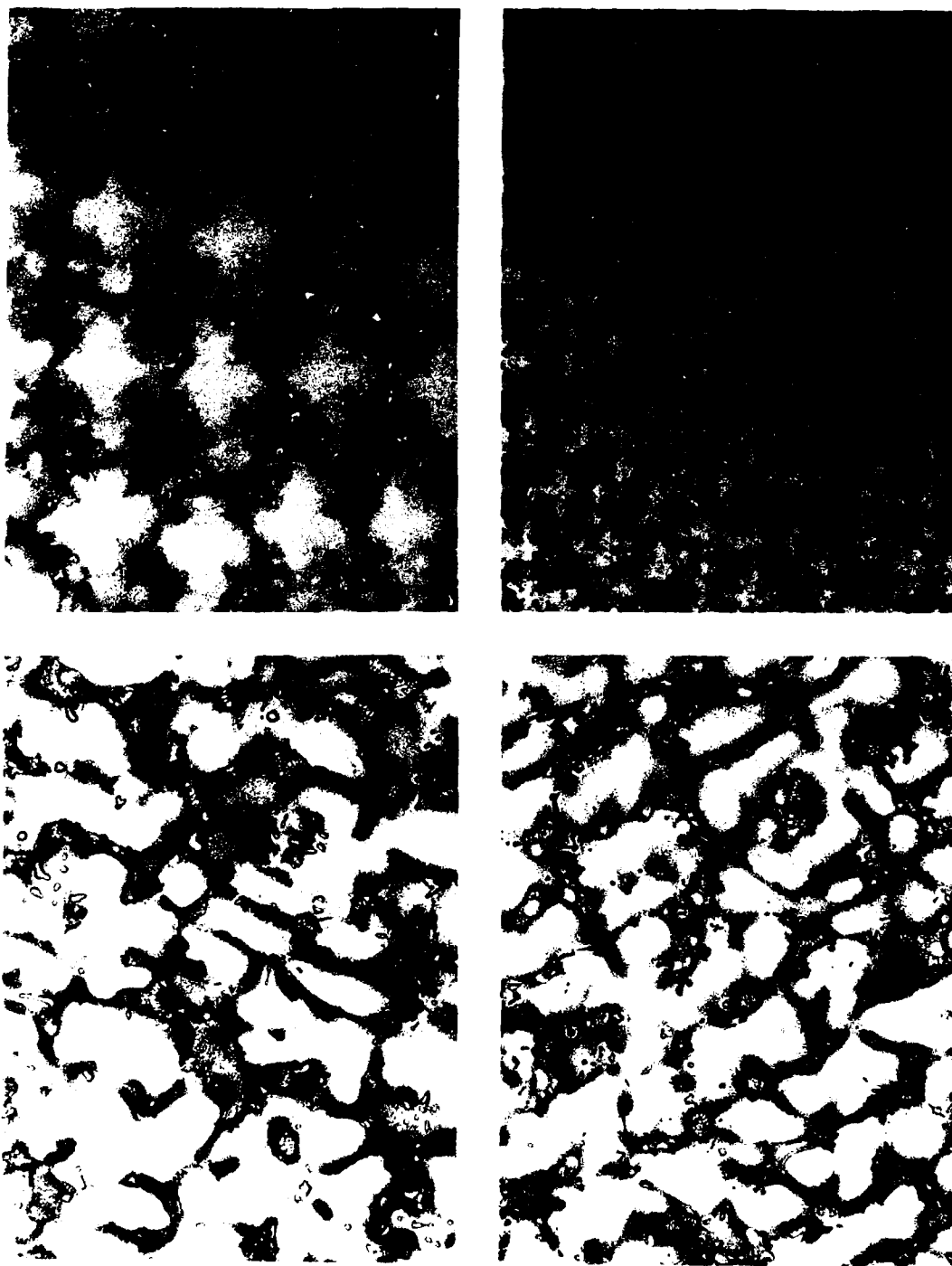


Figure 3.14: Photomicrographs of sections transverse to heat flow typical of samples analyzed to determine primary dendrite arm spacing in Mar-M200 + 1% Hf (50% lactic acid 33% HCl, 17% HNO₃, 100x). Top left: G-30B, high G, low R, high G/R.³ Top right: G-30T, high G, high R, high t. Bottom left: G-29B, low G, low R, low t. Bottom right: G-29T, low G, high R, low G/R.

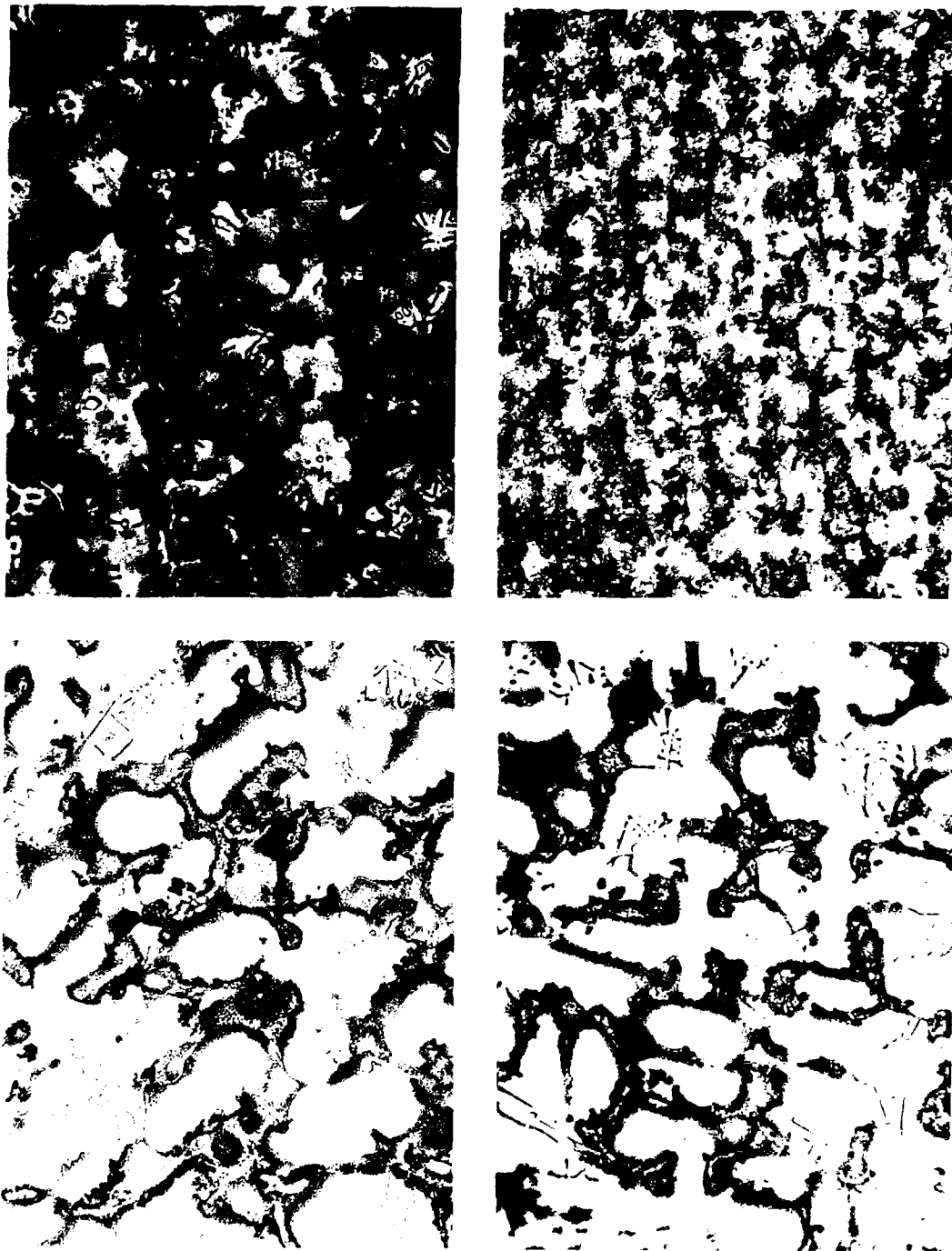


Figure 3.15: Photomicrographs of sections transverse to heat flow typical of samples analyzed to determine primary dendrite arm spacing in Mar-M200 + 2% Hf (50% lactic acid, 33% HCl, 17% HNO₃, 100x). Top left: G-25B, high G, low R, high G/R. Top right: G-25T, high G, high R, high ϵ . Bottom left: G-23B, low G, low R, low ϵ . Bottom right: G-28B, low G, high R, low G/R.

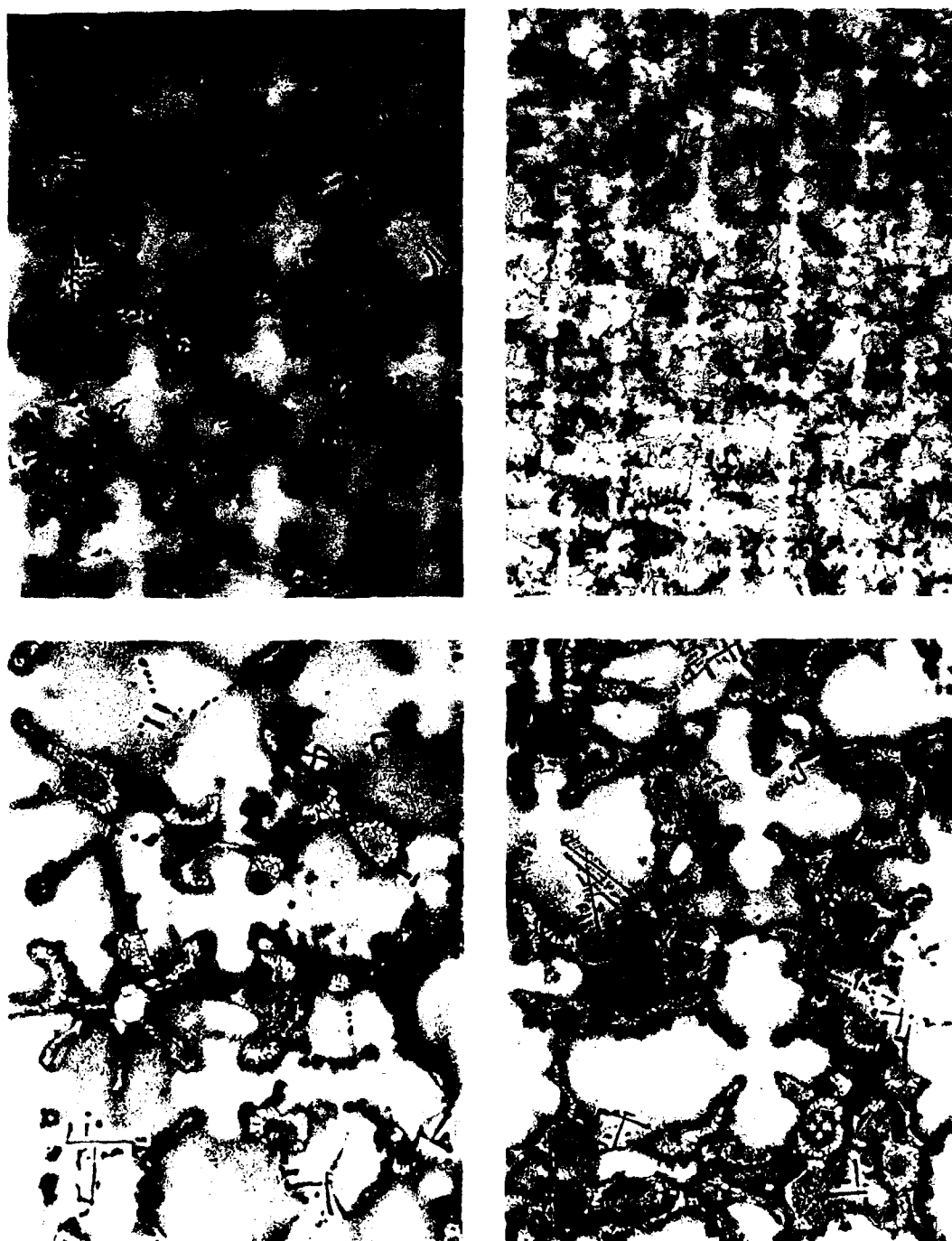


Figure 3.16: Photomicrographs of sections transverse to heat flow typical of samples analyzed to determine primary dendrite arm spacings in HNO_3 (100x). Top left: G-18B, high G, low R, high G/R. Top right: G-18T, high G, high R, high ϵ . Bottom left: 27B, low G, low R, low ϵ . Bottom right: G-27T, low G, high R, low G/R.

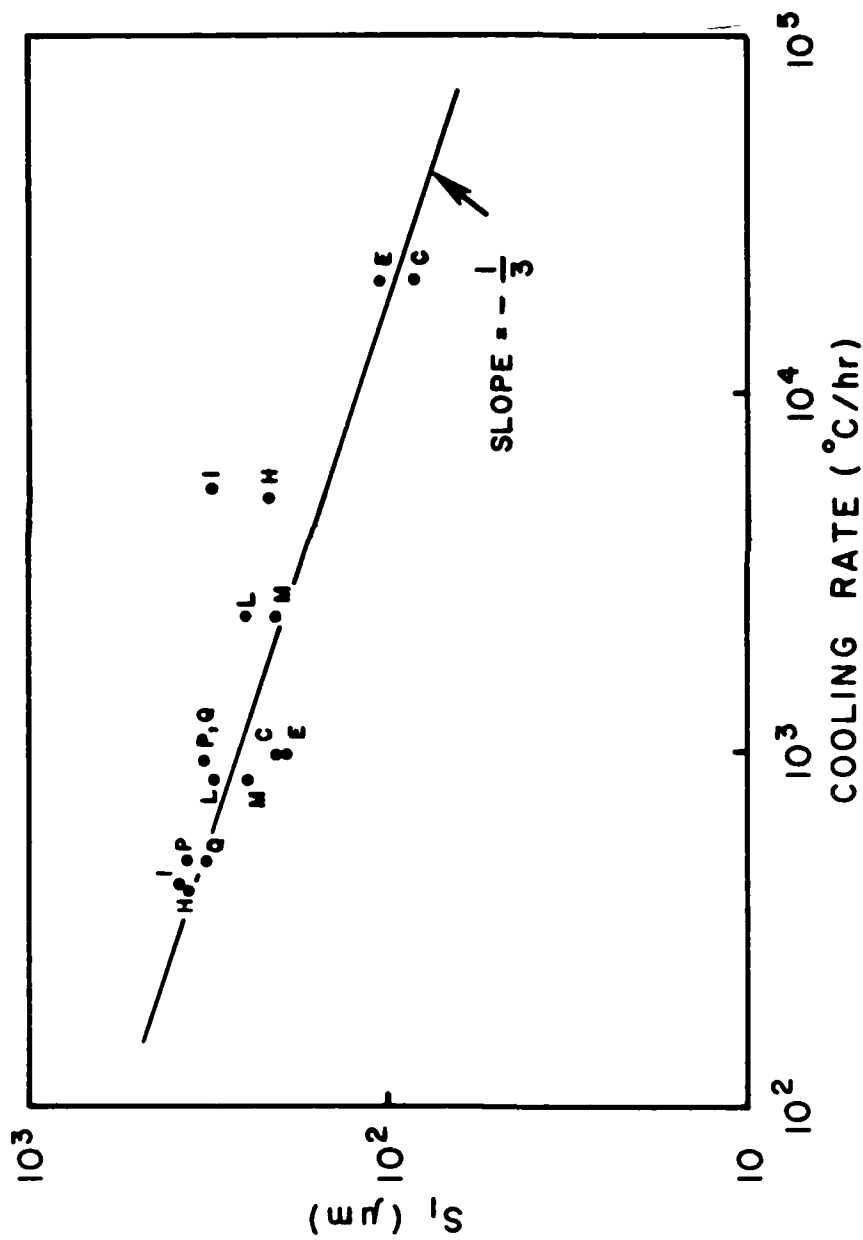


Figure 3.17a: Log of primary dendrite arm spacing versus log of average cooling rate through the freezing range for Mar-M200 and Mar-M200 + 1% Hf alloys solidified in the LMC apparatus.

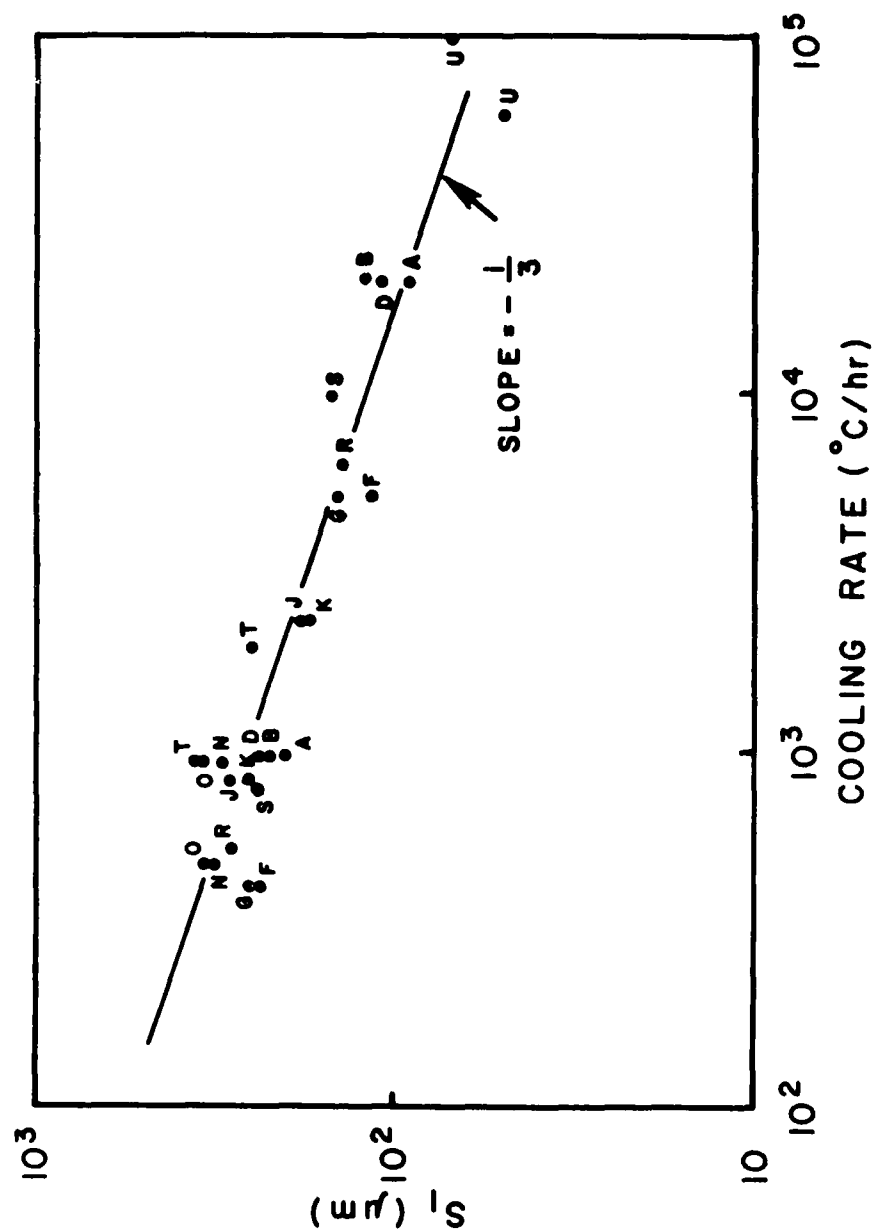


Figure 3.17b: Log of primary dendrite arm spacing versus log of average cooling rate through the freezing range for Mar-M200 + 2% Hf and Mar-M200 + 2.5% Hf alloys solidified in the LMC apparatus.

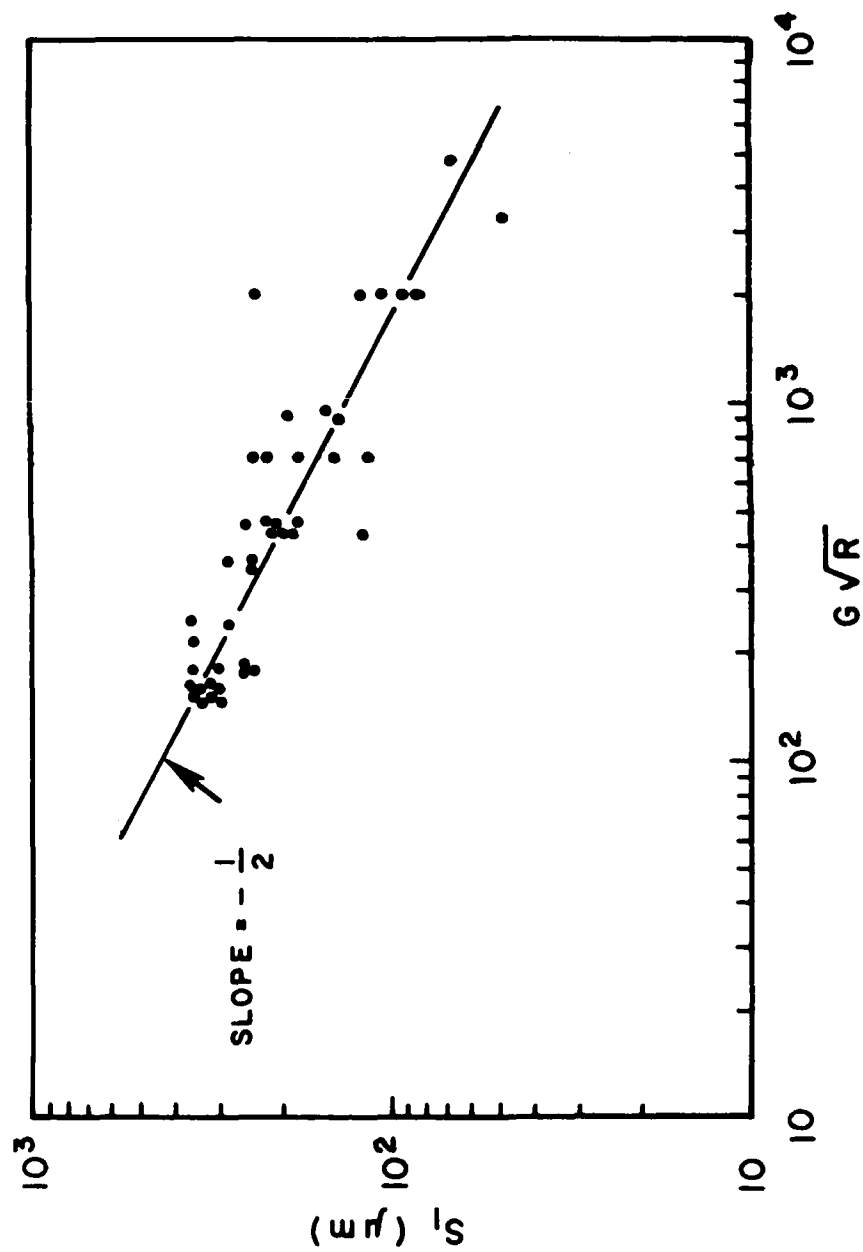


Figure 3.18: Log of primary dendrite arm spacing versus log of $G R$ for Mar-M200 alloys with 0%, 1%, 2%, and 2.5% Hf additions.

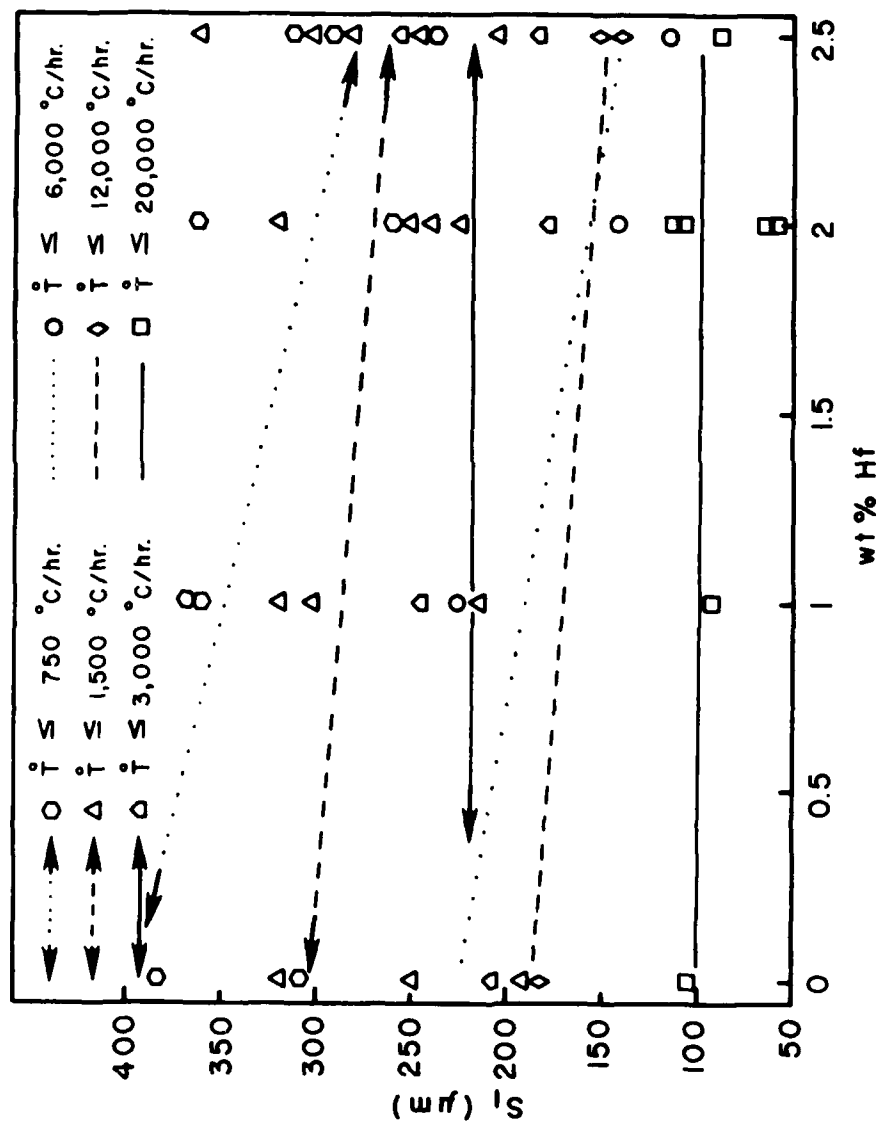


Figure 3.19: Variation of primary dendrite arm spacing with hafnium content for modified Mar-M200.

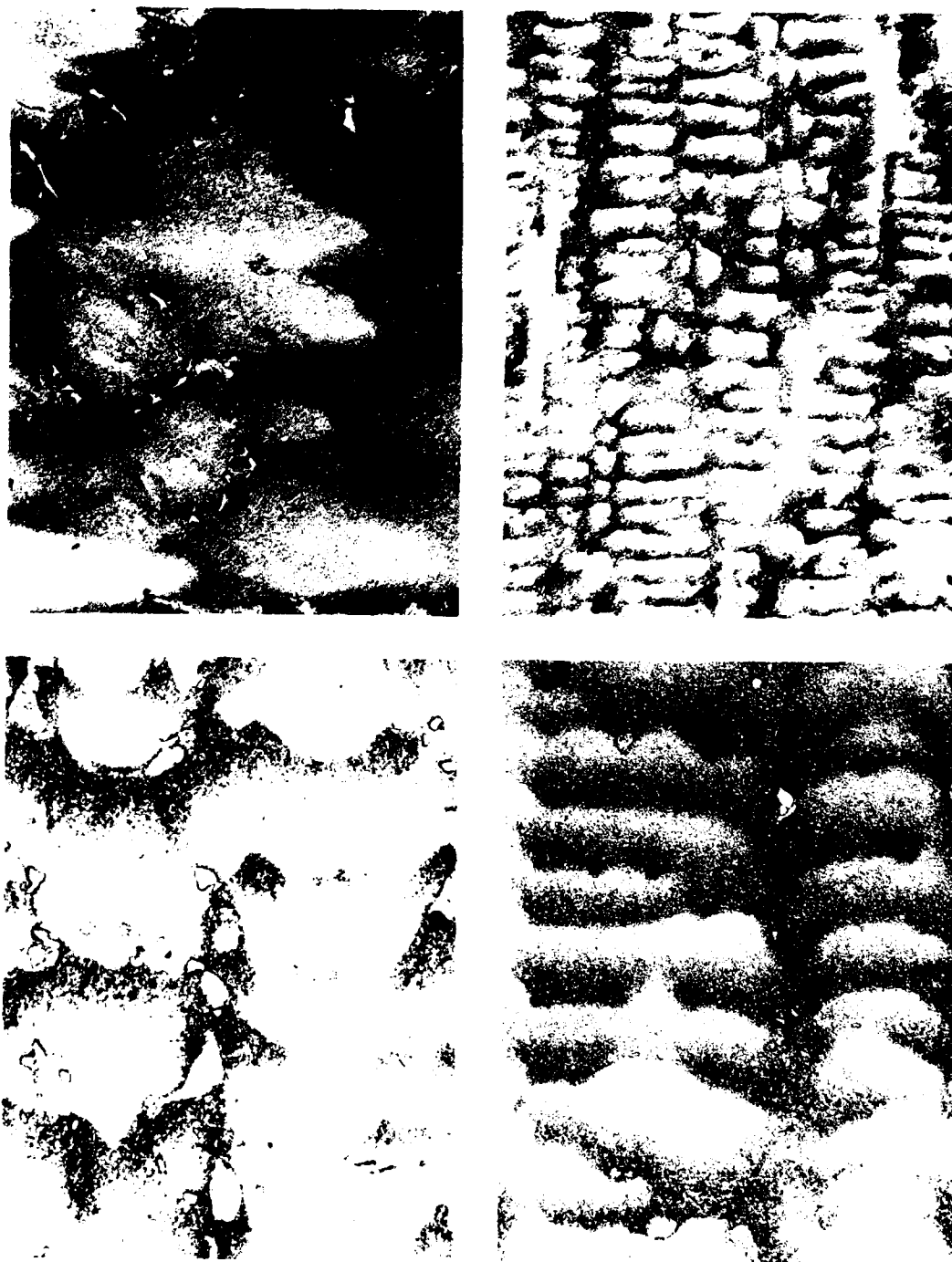


Figure 3.20: Photomicrographs of sections parallel to heat flow typical of samples analyzed to determine secondary dendrite arm spacing in unmodified Mar-M200 (50% lactic acid, 33% HCL, 17% HNO_3 , 200X). Top left: C-3B, high G, low R, high G/R. Top right: C-3T, high G, high R, high ϵ . Bottom left: C-2B, low G, low R, low ϵ . Bottom right: C-2T, low G, high R, low G/R.

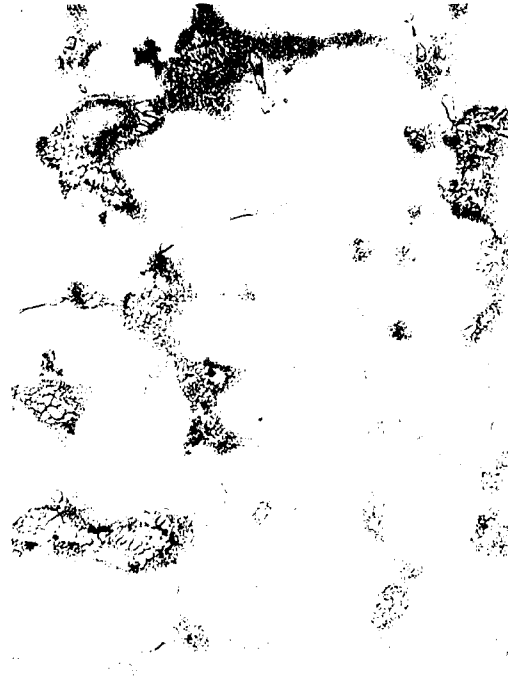
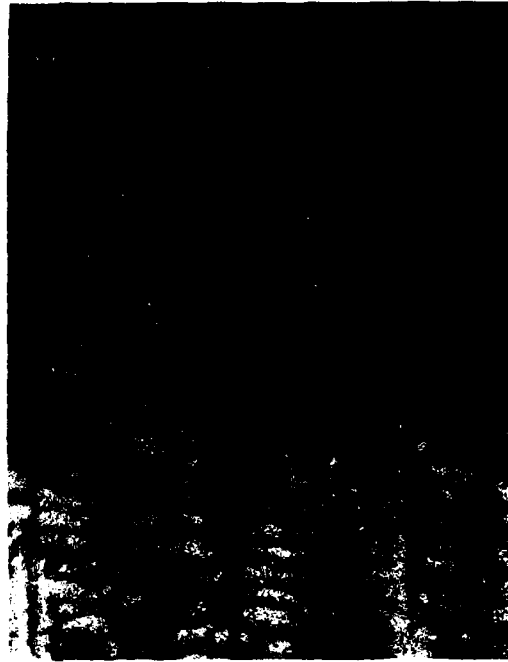


Figure 3.21: Photomicrographs of sections parallel to heat flow typical of samples analyzed to determine secondary dendrite arm spacing in Mar-M200 + 1% Hf (50% lactic acid, 33% HCL, 17% HNO₃, 200X). Top left: G-30B, high G, low R, high G/R. Top right: G-30T, high G, high R, high ϵ . Bottom left: G-28B, low G, low R, low ϵ . Bottom right: G-28T, low G, high R, low G/R.

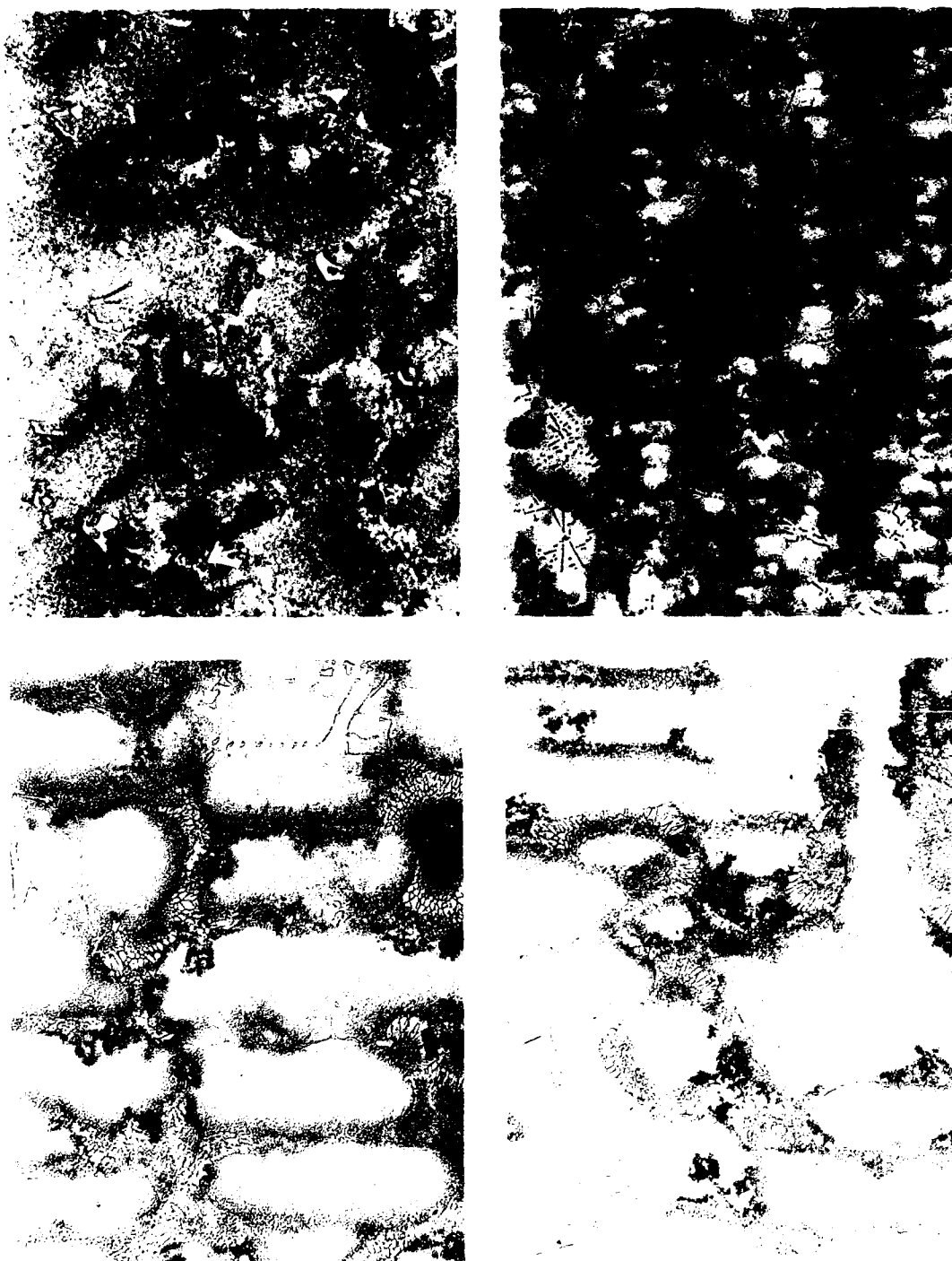


Figure 3.22: Photomicrographs of sections parallel to heat flow typical of samples analyzed to determine secondary dendrite arm spacing in Mar-M200 + 2% Hf. (50% lactic acid, 33% HCL, 17% HNO_3 , 200X). Top left: G-25B, high G, low R, high G/R. Top right: G-25T, high G, high R, high ϵ . Bottom left: G-28B, low G, low R, low ϵ . Bottom right: G-28T, low G, high R, low G/R.

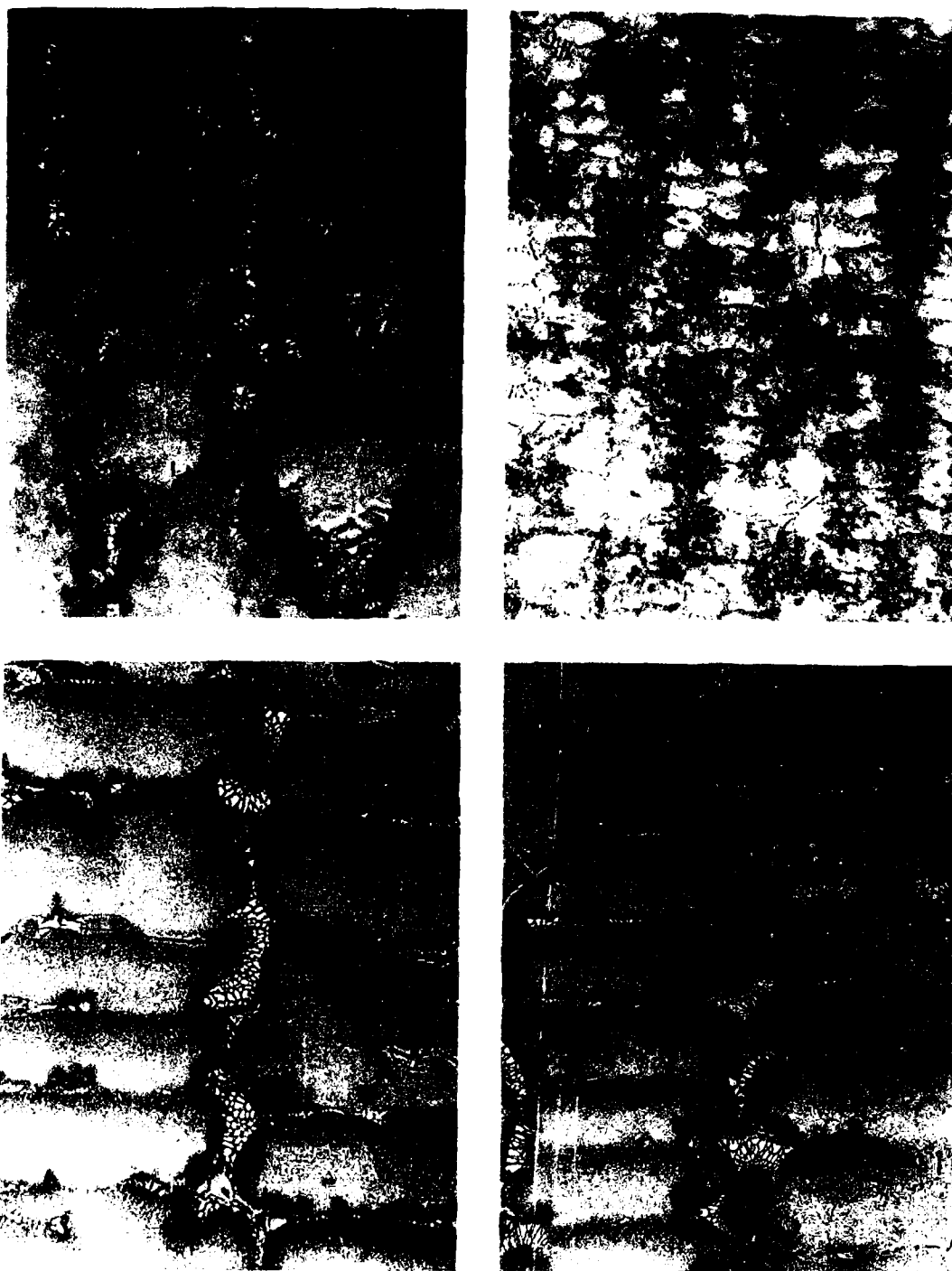


Figure 3.23: Photomicrographs of sections parallel to heat flow typical of samples analyzed to determine secondary dendrite arm spacing in Mar-M200 + 2.5% Hf. (50% lactic acid, 33% HCL, 17% HNO₃, 200X). Top left: G-18B, high G, low R, high G/R. Top right: G-18T, high G, high R, high ϵ . Bottom left: G-27B, low G, low R, low ϵ . Bottom right: G-27T, low G, high R, low G/R.

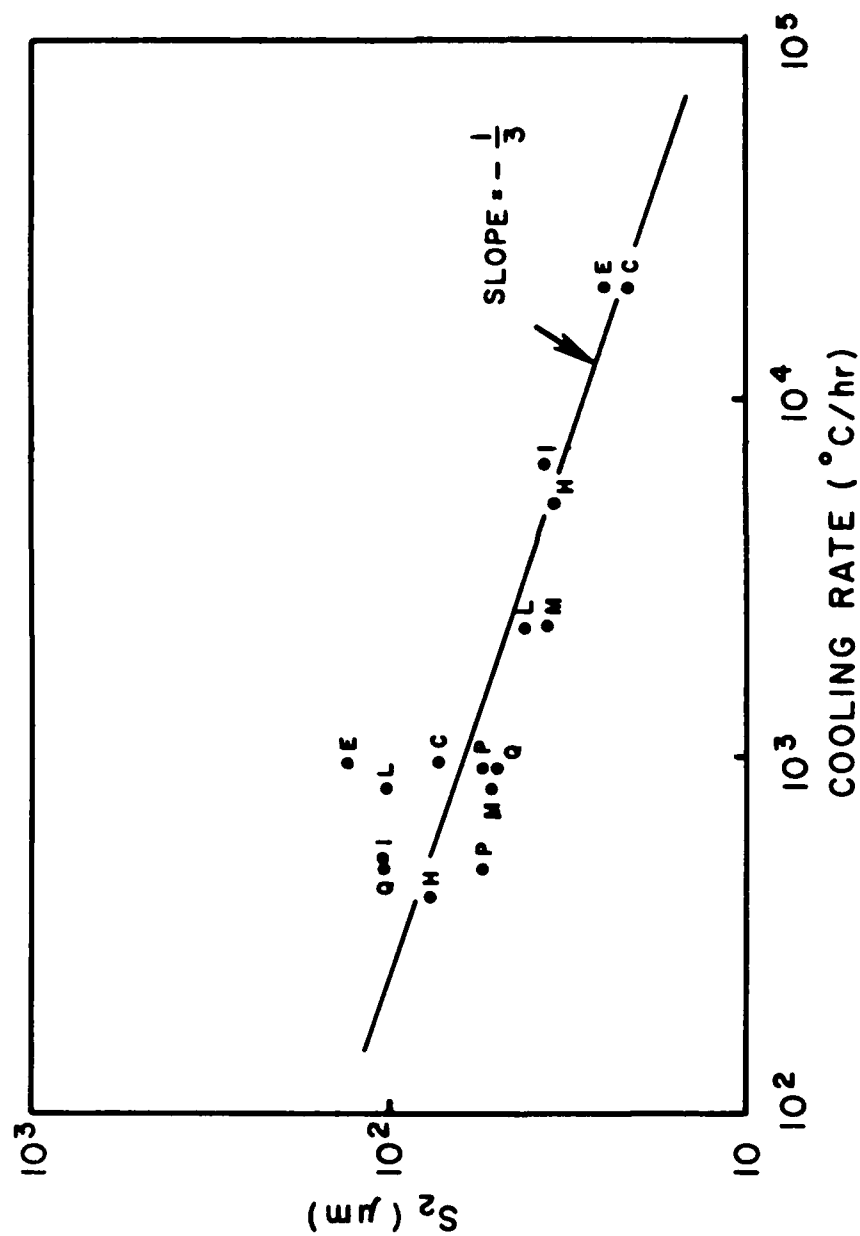


Figure 3.24a: Log of secondary dendrite arm spacing versus log of average cooling rate through the freezing range for Mar-M200 and Mar-M200 + 1% Hf alloys solidified in the LMC apparatus.

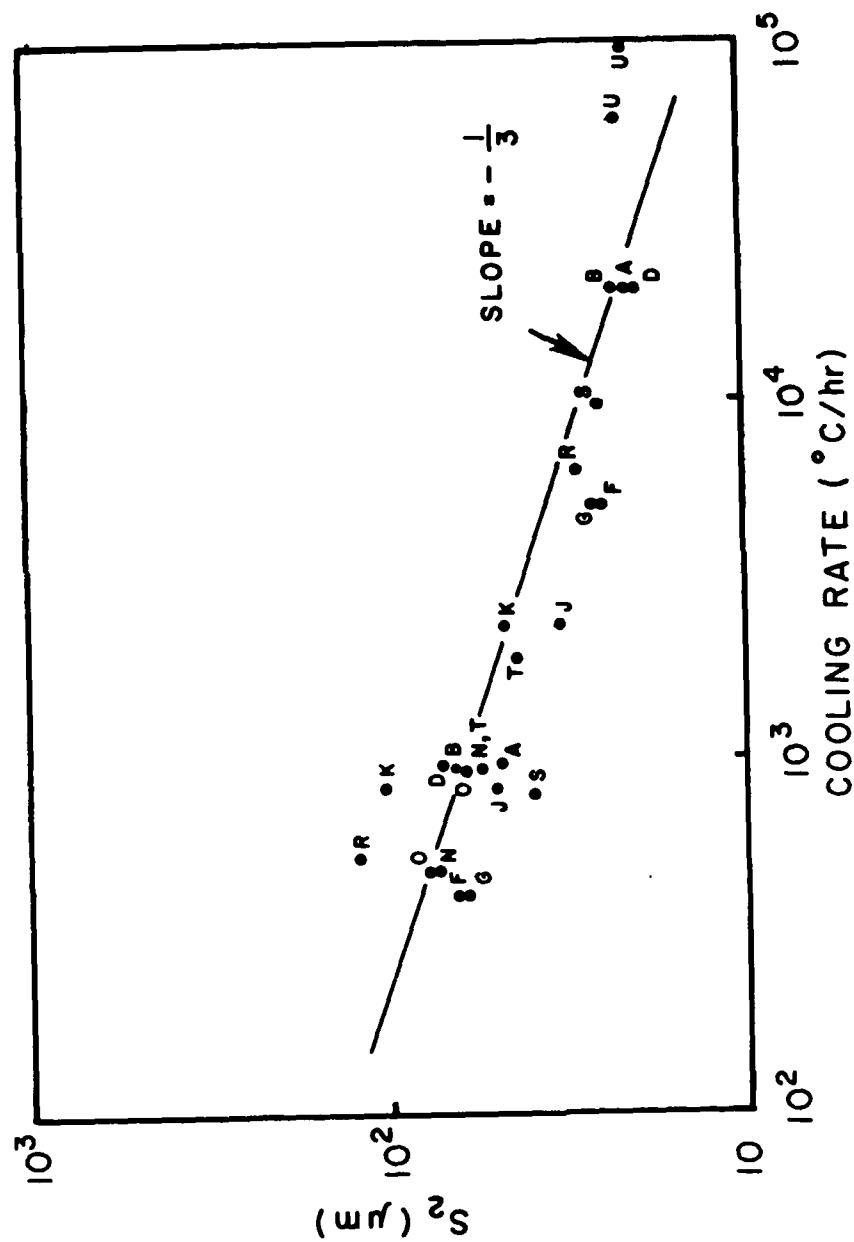


Figure 3.24b: Log of secondary dendrite arm spacing versus log of average cooling rate through the freezing range for Mar-M200 + 2% Hf and Mar-M200 + 2.5% Hf alloys solidified in the LMC apparatus.

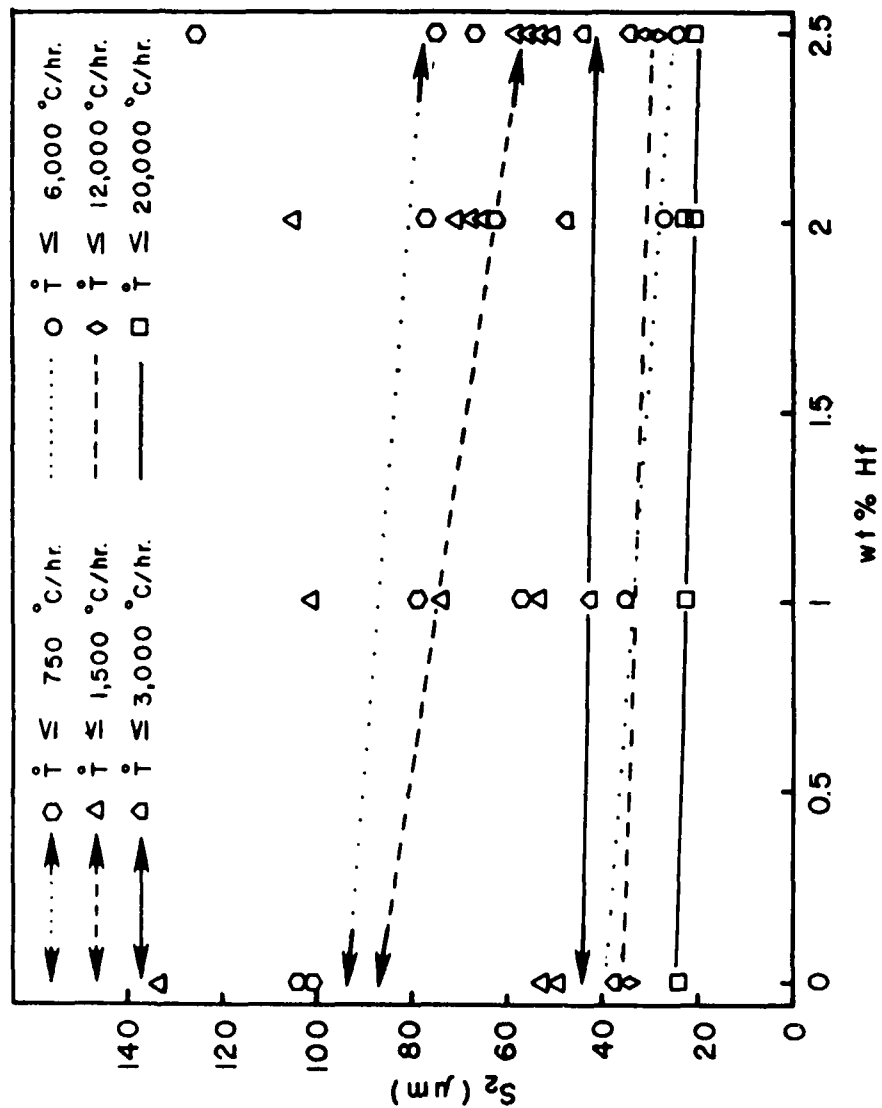


Figure 3.25: Variation of secondary dendrite are spacing with hafnium content for modified Mar-M200.

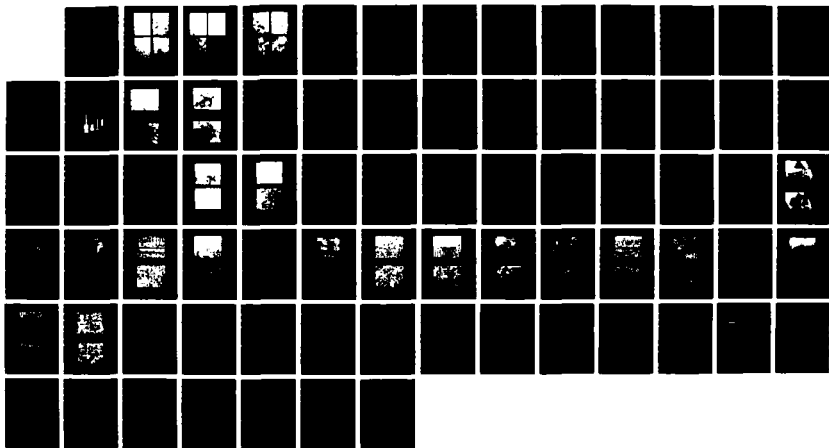


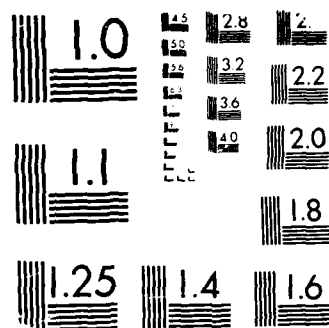
Figure 3.26: Photomicrographs selected to show appearance of eutectic constituent in unmodified Mar-M 200 alloy. Top left: lactic acid, 33% HCL, 17% HNO₃, 100X. C-3B, high G, low R, high G/R. Top right: lactic acid, 33% HCL, 17% HNO₃, 100X. C-3B, high G, high R, high G/R. Bottom left: lactic acid, 33% HCL, 17% HNO₃, 100X. C-3B, low G, low R, low G/R. Bottom right: lactic acid, 33% HCL, 17% HNO₃, 100X. C-3B, low G, low R, low G/R.

EFFECTS OF HAFNIUM ADDITIONS ON THE SOLIDIFICATION BEHAVIOR OF DIRECTIONAL. (U) PITTSBURGH UNIV PA DEPT OF METALLURGICAL AND MATERIALS ENGINE.. H D BRODY ET AL.

NL

OCT 81 SETEC-MME-81-043 AFWAL-TR-81-4123 F/G 11/6.2





MICROCOPY RESOLUTION TEST CHART
 (10X) 3111 1963-1964

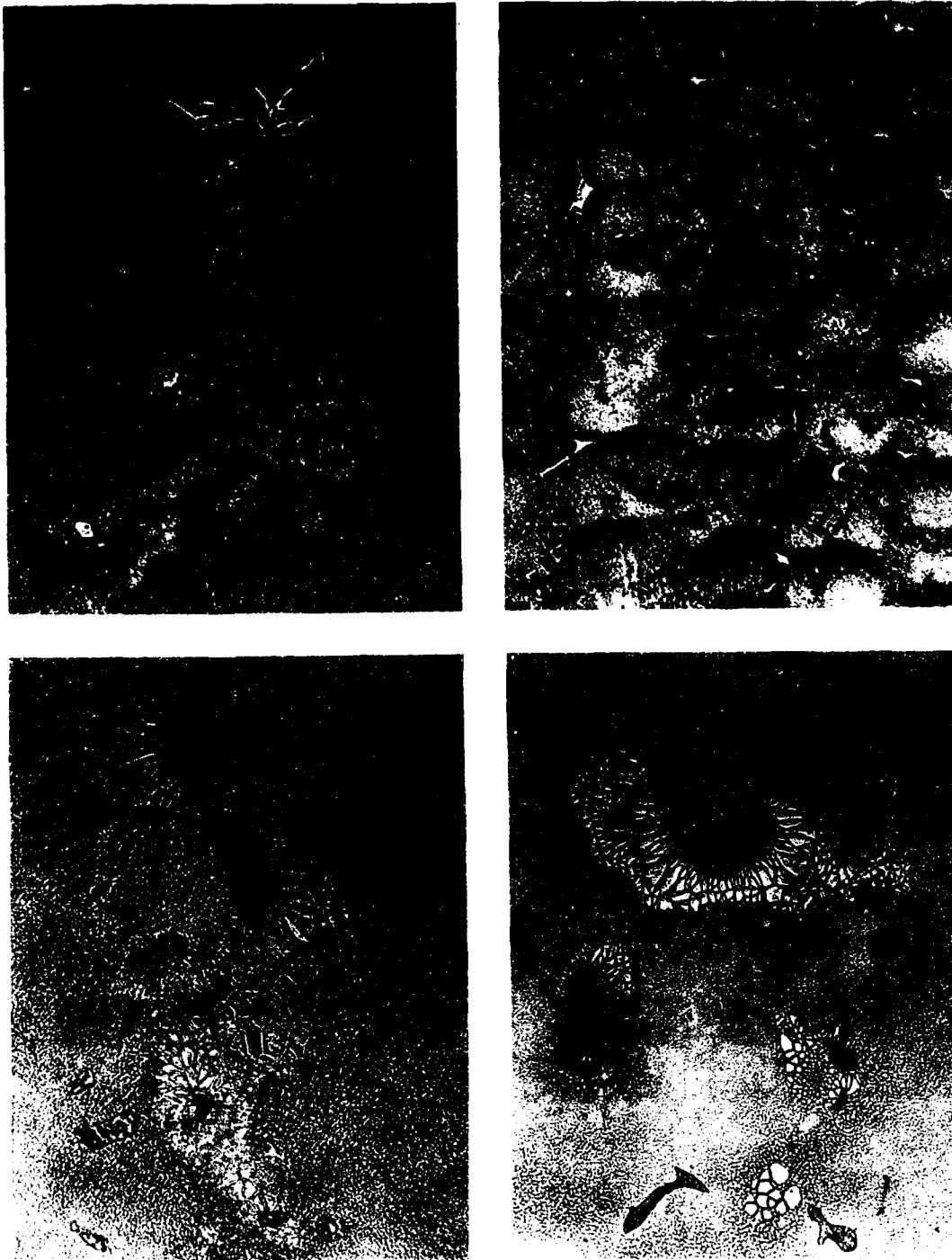


Figure 3.27: Photomicrographs selected to show appearance of eutectic constituent in unmodified Mar-M200 + 1% Hf (50% lactic acid, 33% HCL, 17% HNO₃, 500X). Top left: G-30B, high G, low R, high G/R. Top right: G-30T, high G, high R, high ϵ . Bottom left: G-29B, low G, low R, low ϵ . Bottom right: G-29T, low G, high R, low G/R.

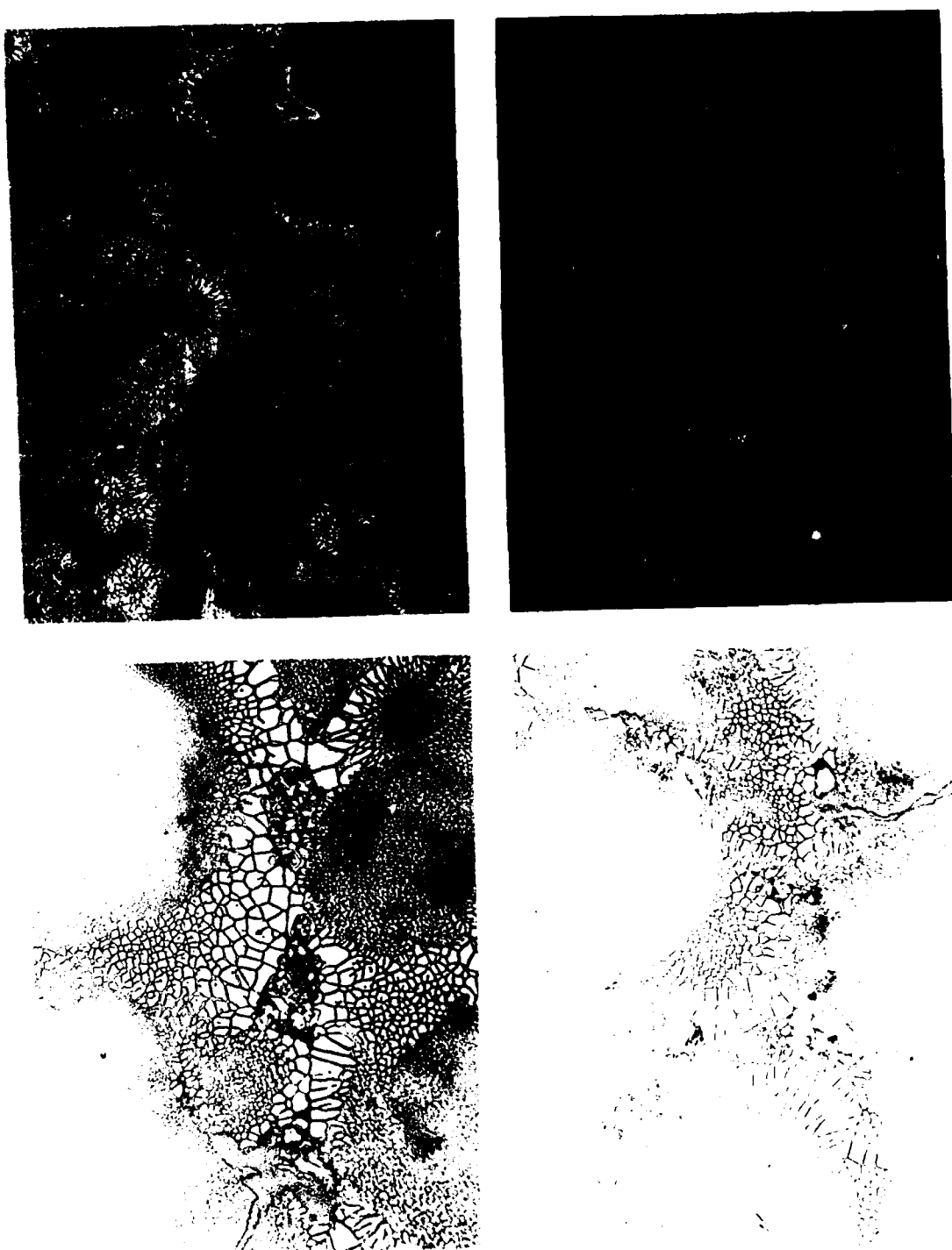


Figure 3.28: Photomicrographs selected to show appearance of eutectic constituent in unmodified Mar-M200 + 2% Hf (50% lactic acid, 33% HCL, 17% HNO_3 , 500X). Top left: G-25B, high G, low R, high G/R. Top right: G-25T, high G, high R, high ϵ . Bottom left: G-28B, low G, low R, low ϵ . Bottom right: G-28T, low G, high R, low G/R.

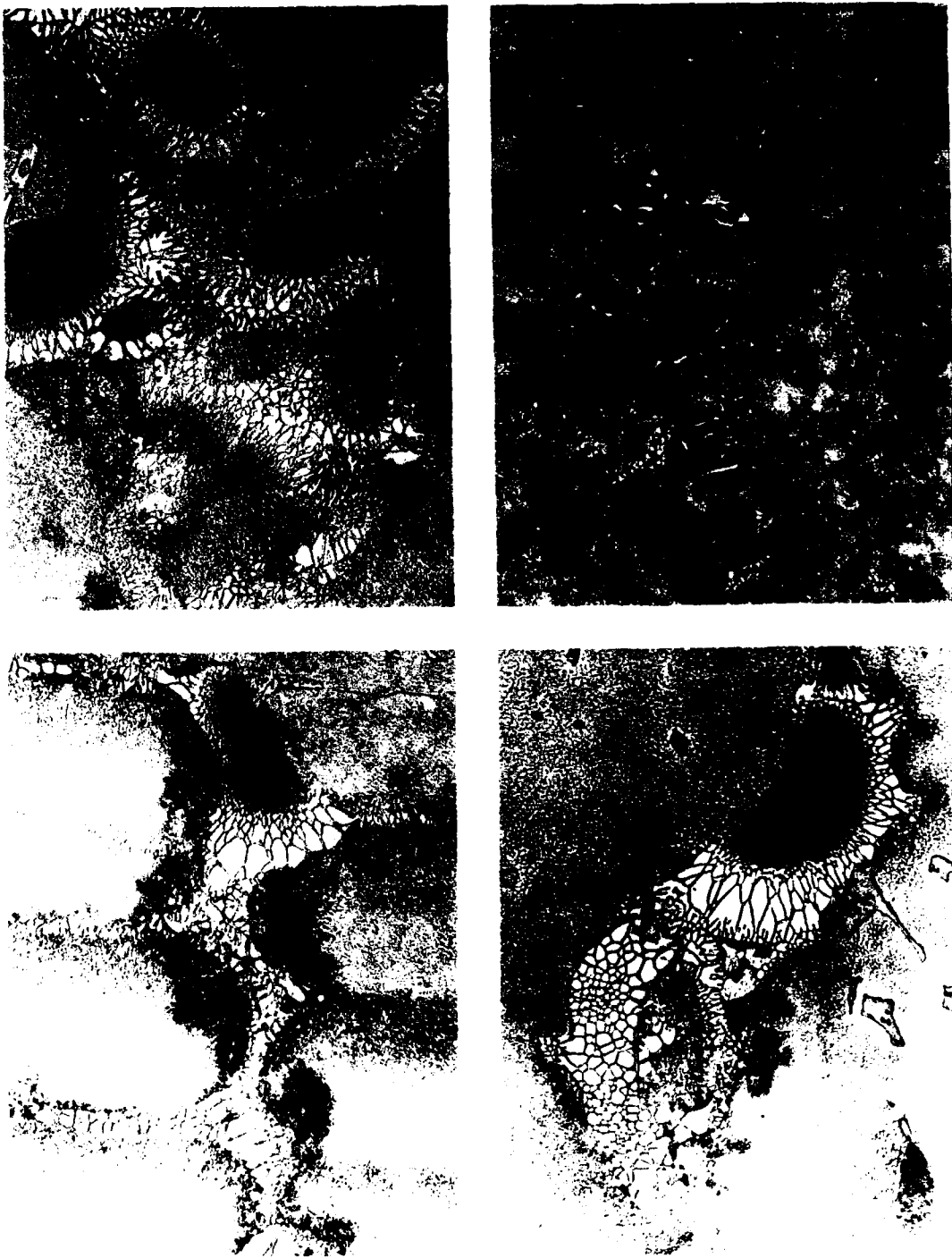


Figure 3.29: Photomicrographs selected to show appearance of eutectic constituent in unmodified Mar-M200 + 2.5% Hf (50% lactic acid, 33% HCL, 17% HNO_3 , 500X). Top left: G-18B, high G, low R, high G/R. Top right: G-18T, high G, high R, high ϵ . Bottom left: G-27B, low G, low R, low ϵ . Bottom right: G-27T, low G, high R, low G/R.

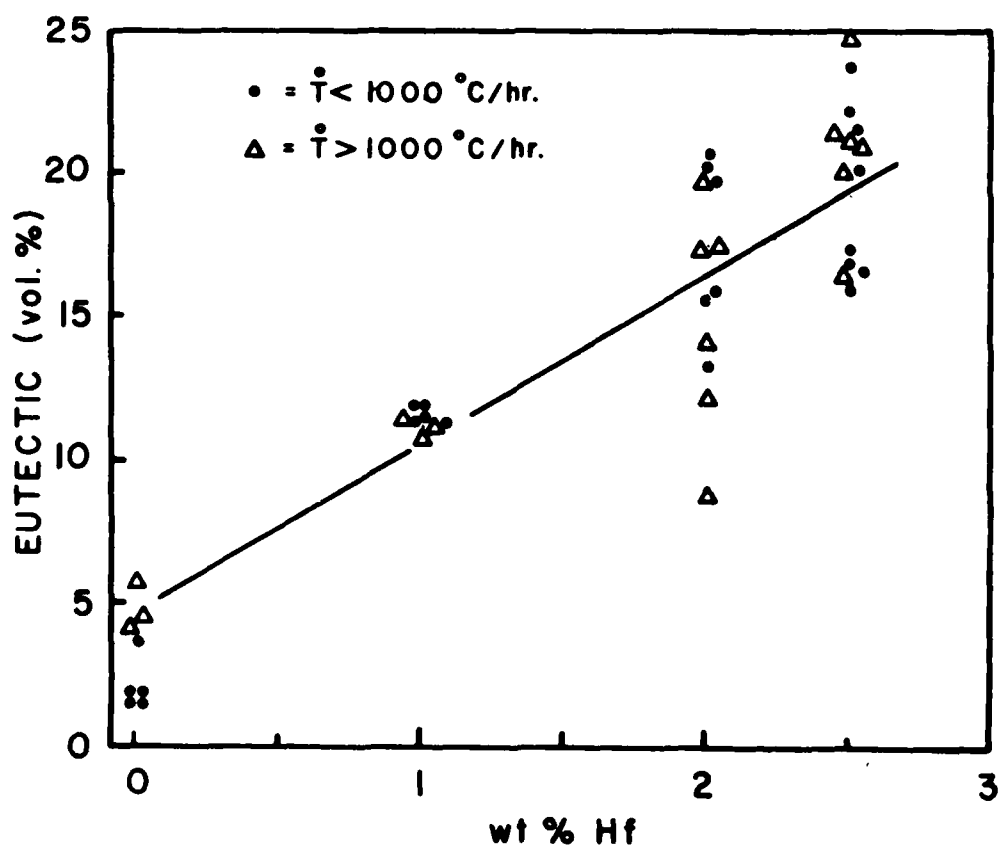


Figure 3.30: Variation of volume percent eutectic constituent with hafnium content in modified Mar-M200 alloys solidified in the LMC apparatus.

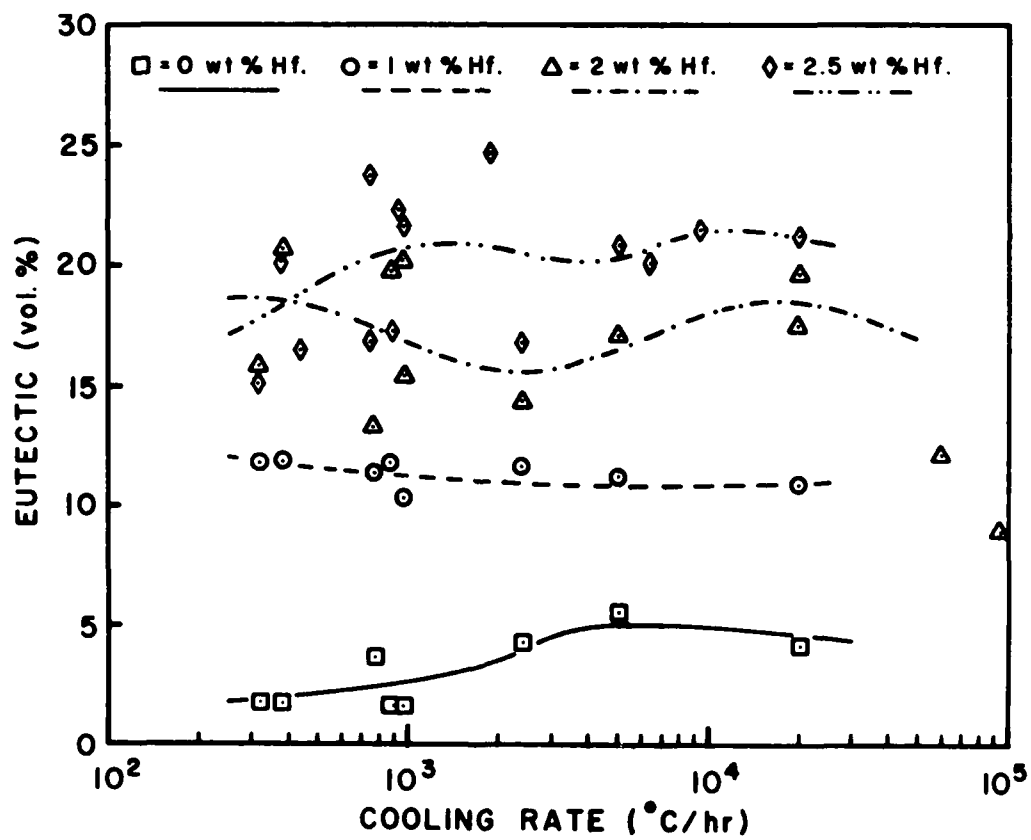


Figure 3.31: Variation of volume percent eutectic with cooling rate for Mar-M200 alloys modified with 0%, 1%, 2%, 2.5% Hf solidified in the LMC apparatus

4.0 Task III: Thin Plate Casting

4.1 Purpose

In order to study the cooling rate sensitivity of the superalloys, several thin plate chill castings(1) were made. The chill castings were solidified at cooling rates higher than those achievable in normal D.S. practice and thus represent one extreme of practice. The slowly cooled samples of Task I represent the other extreme of practice. The samples of Task II are at intermediate cooling rates, spanning normal practice. Local solidification times of the order of 0.5 seconds were possible in the thin plate chill castings. To put this in perspective with respect to cooling rates reported in other parts of the report, a local solidification time of 0.5 seconds would be equivalent to a cooling rate of $300^{\circ}\text{C}/\text{sec.}$, $18,000^{\circ}\text{C}/\text{min.}$, or $1,100,000^{\circ}\text{C}/\text{hr.}$ The cooling rate across the casting would be fairly uniform.

Analysis of the cast plates has been metallographic. The intent was to inspect for gross changes in the appearance or distribution of phases, especially for changes in the amount of eutectic. Segregation effects were determined quantitatively by SEM analyses. As in other phases of the study, hafnium content was the independent variable studied. The studies of this task were exploratory in nature; with the idea that if significant cooling rate effects were found, more definitive studies would be proposed.

4.2 Experimental Procedure

4.2.1 Chill Plate Casting

The technique developed for chill plate casting is depicted by the apparatus sketched in Figure 4.1. An assembled and an unassembled chill mold are shown in Figure 4.2. Two copper chill blocks separated by thin shims were fastened to each other and to a top plate. The shims separate the chill blocks and set the thickness of the cast plate. The top block was connected to a ten liter bottle under a partial vacuum of less than one torr. The bottom half of the outside surface of the mold was coated with a thick layer of zirconia cement. The inside surface was given a thin coat of carbon black. CO_2 sand was used to keep the metal from running past the mold into the steel and vacuum tubing. When the alloy had been melted and brought to the right superheat ($1650\text{--}1700^{\circ}\text{C}$) under vacuum (about 10^{-2} torr) in the vacuum induction melting furnace, the furnace was filled with argon up to a preselected partial pressure (650 mm). Then the chill mold, which had been positioned in the chamber of a melt sampling device (number 3 in Figure 4.1) directly above the crucible, was lowered into the molten superalloy and the valve to the vacuum bottle opened. After the mold was filled, it was raised out of the furnace and the slide valve to the melt sampling device closed. The chill mold and plate casting could be removed and additional copper molds attached, sequentially, for the casting of a series of plate samples of the same alloy.

The casting variables that could be varied were pressure difference, shim thickness (and, thus, casting thickness), and mold preheat. Alloy variables that could be controlled were alloy superheat (although a minimum preheat of 200°C was required to fill the mold) and alloy content, in particular hafnium.

4.2.2. Microstructural Examination

Samples were cut from the plate castings and prepared for microexamination by standard metallographic techniques. HCl-H₂O₂ (7:1) etchant was used for revealing dendritic structure.

The primary dendrite arm spacing, d_1 , was measured by counting the number of dendritic centers, N , per unit area, A , at magnification M and using the following equation:

$$d_1 = \frac{1}{M} \sqrt{\frac{2A}{N}} \quad (4-1)$$

The secondary dendritic arm spacing, d_2 , was measured by counting the number of secondary dendrites, n , along a line of length L , at magnification M and using the following equation:

$$d_2 = \frac{L}{M(n-1)} \quad (4-2)$$

The primary dendrite arm spacing measurements were made on the chill surface of the sample. SEM pictures were used for this purpose. The secondary dendrite arm spacing measurements were made on the transverse section of the sample. (Note: Figure 4.1c.).

The eutectic was revealed by etching with H₂O-HNO₃-HF (50:45:5) solution. Optical metallography could not resolve the structure clearly. SEM pictures were taken to measure the volume fractions of eutectic. The volume fraction was measured from at least ten SEM pictures of each sample by the point count method using a 100 point grid.

The volume fraction of carbides was measured optically by the point count method using 30 placements of a 100 point grid, with an accuracy of about 0.1 pct.

Chemical analyses for C, N and O, as determined by Pratt and Whitney Aircrat, are listed in Table 4.1 for 5/8 cm thick plates.

4.3 Results

As expected, the solidification structure of the chill cast alloys are much finer than the solidification structures studied in other phases of this work. Optical metallography revealed the nature of the carbides and dendrites. Scanning electron metallography was required to reveal the presence of eutectic.

Examples of the solidification structure of the chill cast super-alloy plates are shown in Figure 4.3. Primary dendrite spacings were measured from surface sections as in Figure 4.3a and secondary dendrite spacings were measured in sections perpendicular to the mold wall as in Fig. 4.3b. The results of dendrite arm spacing measurements are reported in Table 4.2. Differences among these samples (as functions of plate thickness and hafnium content) are small in comparison to the differences between these samples and those measured in the samples of Task I and II.

The carbides as shown in Figure 4.3b and 4.3c are a mixture of particle and script types and they are distributed almost exclusively in the interdendritic regions. The measured volume percent carbide values are listed in Table 4.3. The variations are not thought to depend on cooling rate or hafnium content. They correlate more strongly with retained carbon, Table 4.1, and the difficulty in resolving the fine carbides in the thinner samples. At these cooling rates, the size of the carbide particles is about one micron.

Scanning electron microscopy was used to reveal the eutectic structure as shown in Figure 4.3d. Table 4.4 presents the data for 0.62 cm thick chill cast plates. While the volume fraction of eutectic varies significantly with hafnium content, there is no major difference between the amount of eutectic in chill cast samples of this thickness and that measured for normal D.S. cooling rates, Task II. Thinner plates did show a decrease in eutectic constituent, but those cooling rates are far higher than commercial practice (see Chapter 7.0).

4.4 Summary

Chill cast plates have a fine solidification morphology with secondary dendrites in the 4-5 μ range, primary dendrite spacings around 10 μ , and carbide particles and eutectic pools about 1 μ . The carbides are mixed between particle and script types and always occur in the interdendritic regions. Importantly, high cooling rates do not seem to have a major effect of eutectic volume fraction. Extremely high cooling rates, with regard to normal D.S. practice, did not produce significant variability in eutectic volume fraction.

4.5 Reference

1. T.F. Bower and M.C. Flemings, "Formation of the Chill Zone in Ingot Solidification," Trans. AIME (1967) 239, 216-220.

Table 4.1: Interstitial Analysis of 20/32 cm. Chill Plate Castings.

MAR-M200 Plus	C ⁺ (%)	N (ppm)	O (ppm)
0%Hf	0.041	20	65
1.0%Hf	0.062	<10	30.5*
2.0%Hf	0.12	14.5*	42.5*
2.5%Hf	0.094	15.5*	104*

⁺ Carbon loss was attributed to the high superheat required to draw samples.

* Average of duplicate tests. Nitrogen variability ± 0.5 ppm. Oxygen variability ± 19 ppm.

Table 4.2: Dendrite Spacings in Chill Castings

Alloy MAR-M200 Plus	Plate Thickness			
	Primary/Secondary (microns)			
	0.63 cm	0.47 cm	0.31 cm	0.16 cm
0% Hf	9.2/6.8	10.2/6.5	9.2/5.2	9.5/4.1
1% Hf	8.5/6.7	8.2/6.4	8.5/4.8	9.2/4.0
2% Hf	11.2/6.2	10.1/5.8	9.5/5.8	9.6/4.3
2½% Hf	9.3/6.8	8.3/6.0	9.1/4.8	9.5/3.4

Table 4.3: Volume Percent Carbides in Chill Castings

Alloy MAR-M200 Plus	Plate Thickness			
	Transverse/Surface			
	0.63 cm	0.47 cm	0.31 cm	0.16 cm
0% Hf	0.4/0.3	0.4/0.3	0.3/0.2	0.2/0.2
1% Hf	0.5/0.3	0.3/0.3	0.2/0.2	0.2/0.2
2% Hf	1.0/0.7	0.9/0.5	1.1/0.5	0.6/0.5
2½% Hf	0.5/0.4	0.4/0.4	0.5/0.5	0.3/0.4

Table 4.4: Volume Percent Eutectic in Chill Castings

Alloy MAR-M200 Plus	Plate Thickness (cm.)	Volume % Eutectic
0%	0.63	7.2
1%	0.63	16.2
2%	0.63	17.3
2½%	0.63	18.5

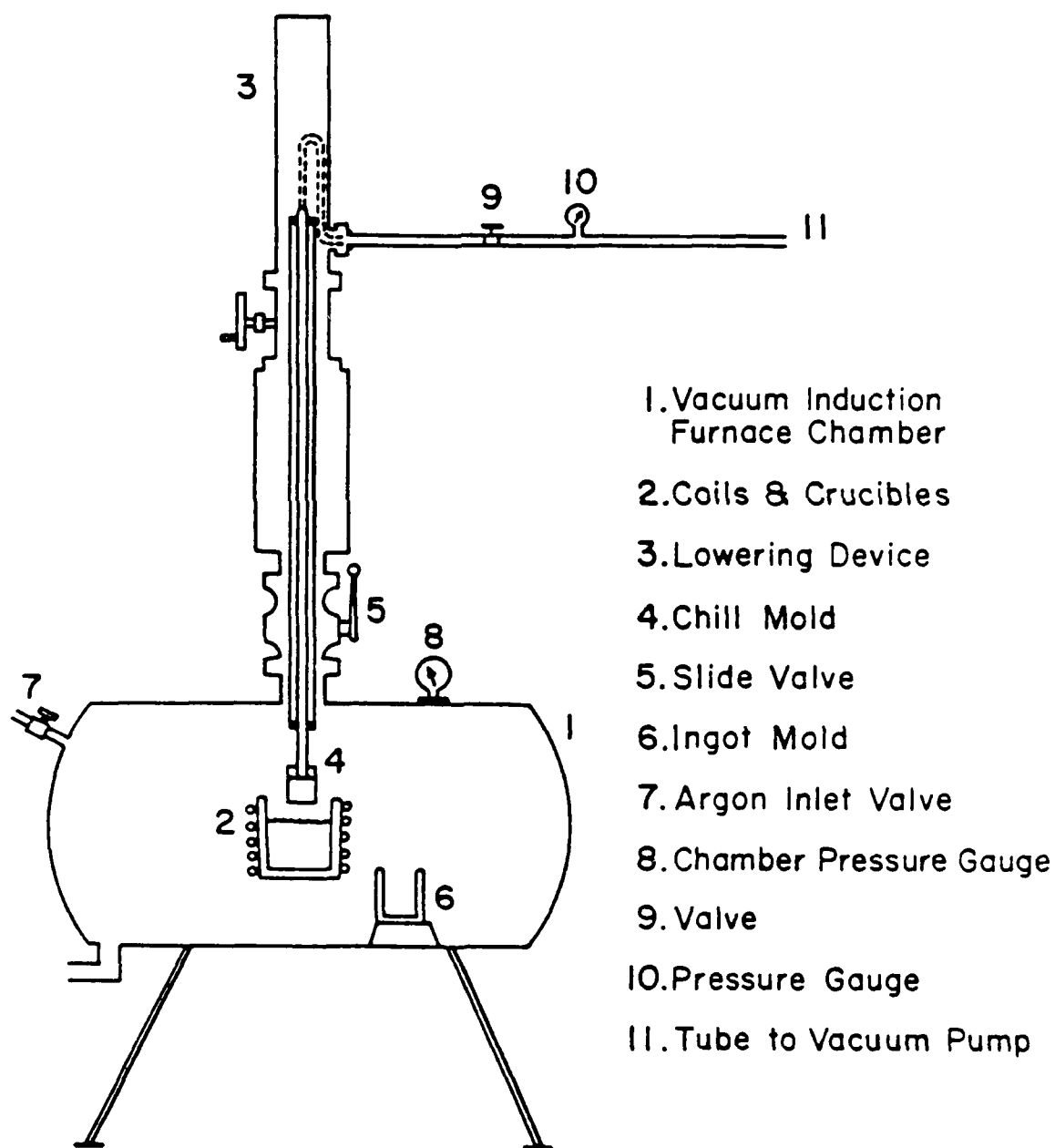


Figure 4.1: (a) Apparatus for chill plate casting; schematic.

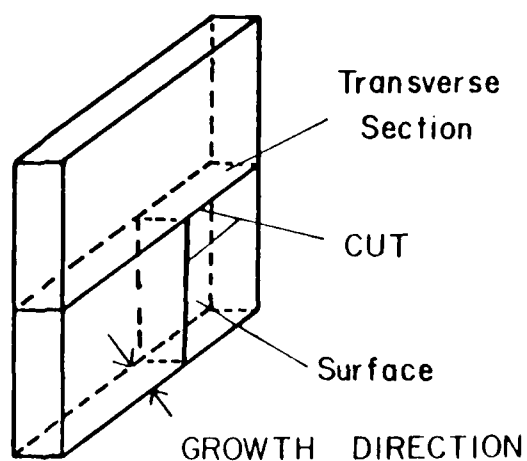
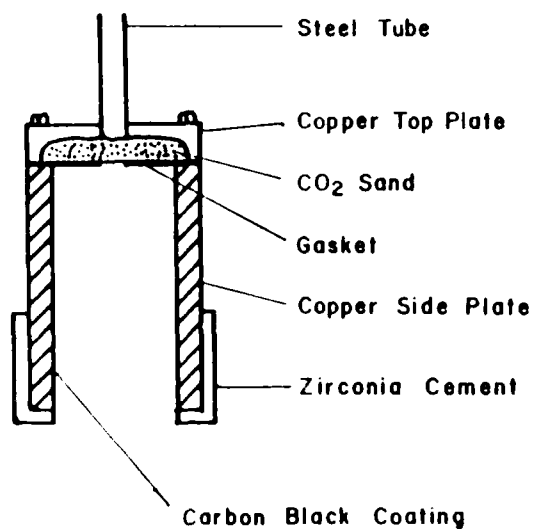
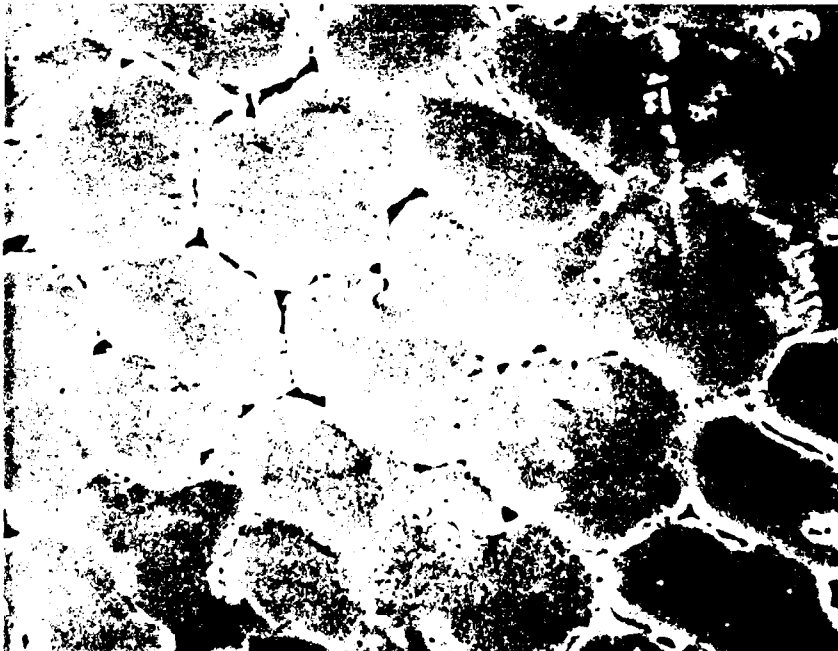


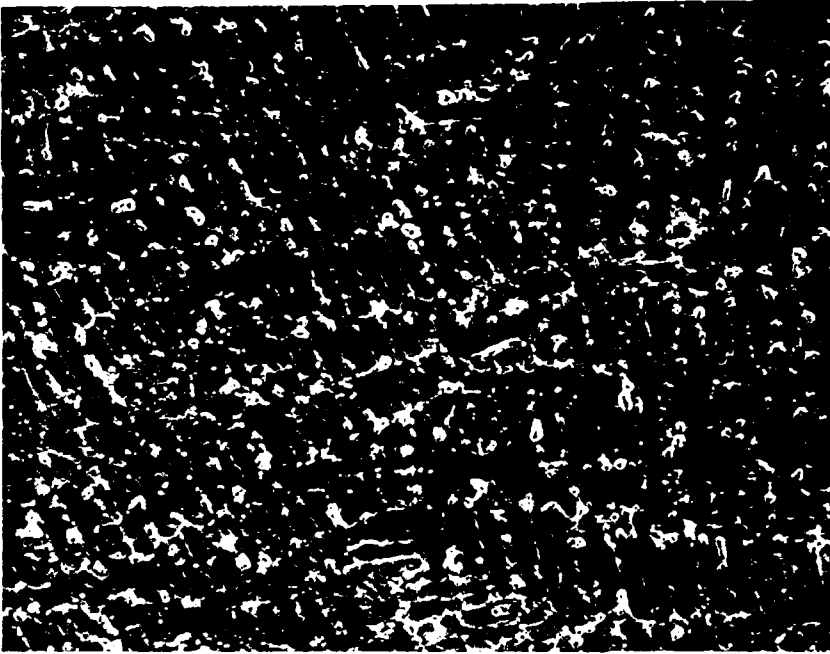
Figure 4.1 (b): Top: Sectional view of the chill mold, schematic. Bottom: Schematic diagram of a thin plate casting illustrating the procedure for sectioning of samples for microexamination.



Figure 4.2: Mold for chill plate casting. Thermocouple is inserted in this mold for freezing time measurement. An assembled mold is shown on the left and an unassembled mold in the middle. A chill cast plate is shown at right (reduced in scale about 63%).



(a)



(b)

Figure 4.3: Scanning electron micrographs of chill plate castings: (a) Mar-M200 + 2.5% Hf (800x) typical of surface sections used for primary dendrite arm spacing measurements and (b) Mar-M200 + 1.9% Hf (1600x) typical of transverse sections used for secondary dendrite arm spacing measurements.



(c)



(d)

Figure 4.3 (continued): Scanning electron micrographs of chill plate castings: (c) Mar-M200 + 1.9 % Hf (4000x) illustrating script carbide morphology and (d) Mar-M200 + 1.0% Hf (1800x) illustrating morphology of eutectic pools.

5.0 Task IV: Macrosegregation Studies

5.1 Background and Approach

The main source of macrosegregation in dendritic freezing of alloys is the bulk flow of solute enriched (or depleted) liquid. The bulk flow results from the combination of the need to feed solidification shrinkage and from convection due to temperature and solute induced density gradients in the liquid(1). An alloy susceptible to macrosegregation from this mechanism would exhibit macrosegregation effects in regions where geometry or cooling conditions change. In this task, the propensity of nickel base superalloys to exhibit macrosegregation from the flow of liquid to feed shrinkage was screened by a simple test. The screening test was applied to MAR-M200 with varying amounts of hafnium; and the microstructural and chemical variations that resulted were observed.

A simple technique to study the effects of changes in feed metal flow rate that result from changes in the geometry of the mold is to directionally solidify the alloy to be studied in a mold with an abrupt reduction in cross section. Such a mold configuration is shown schematically in Figure 5.1. If the alloy were prone to macrosegregation by this mechanism, it would show negative macrosegregation* at the position of the change in cross section, position B in Figure 5.1. At the same height but at position E, where fluid flow becomes parallel to the isotherms, the alloy should show positive macrosegregation. A region of positive macrosegregation adjacent to the chill would be confirmation of the tendency of the alloy to form macrosegregation as a result of bulk fluid flow processes.

5.2 Experimental Procedure

5.2.1 Casting Technique

Cylindrical ingots with a 9/1 reduction in cross section were directionally solidified by the withdrawal (H.R.S.) process. Melting was in a laboratory vacuum induction furnace. The investment mold was heated by a graphite resistance element. The overall experimental set up is sketched in Figure 5.2.

The charge to the vacuum induction melting furnace was prealloyed ingot. Commercial alumina crucibles were used for melting; the temperature of the melt was monitored by an optical, two color pyrometer (with

*Negative macrosegregation is a local depletion of the elements with $k_i < 1$ that tend to concentrate in the liquid, e.g. Ti, and a local enrichment of the elements with $k_i > 1$ that tend to concentrate in the solid phase, e.g. W. Positive macrosegregation would be a local enrichment of elements with $k_i < 1$ and a local depletion of elements with $k_i > 1$.

an accuracy of $\pm 10^{\circ}\text{C}$). The melts were stabilized at superheats of 110°C (above the liquidus temperature of the particular alloy) before pouring.

The molds were heated using a graphite resistance element and an alumina heat shield as sketched in Figure 5.2. The mold was preheated to 1485°C in the top section using power supply settings of about 10V and 175A. The temperature was continuously monitored during preheat and during solidification. Melting was initiated after the mold temperature stabilized.

The wax patterns were designed as in the sketch of Figure 5.3. The molds were made by Pratt and Whitney Aircraft of an alumina based investment mix. A flange was added to the bottom of each mold so that it could be attached to the chill.

The chill assembly consisted of a circular copper chill plate and a water cooled stainless steel rod that supplied water to the chill plate through concentric channels. The top surface of the chill was grooved to aid in heat transfer.

After the charge was melted the mold cover was lifted, the melt poured, the mold cover replaced, and the mold withdrawn at a rate of 15 cm/hr. The same procedure was employed for all alloys.

5.2.2 Analyses

The ingots were sand blasted and macroetched to check for columnar grain structure. After macroexamination they were sectioned for microexamination as illustrated in Figure 5.3.

Chemical analysis of each plane of cut was determined by quantitative x-ray fluorescent analysis* after metallographically polishing the surfaces.

5.3 Results

Etching of the ingots for macroscopic metallographic examination indicated columnar grains that continued through the region of the reduction in cross section. It is implied that heat flow remained substantially unidirectional and the isotherms remained planar at the change in cross section.

The concentration of Ti, W, Co, and Hf are plotted as functions of distance from the chill surface along the centerline in Figure 5.4. Considering macrosegregation at the change in cross section:

*Spectrochemical Laboratories of Franklin Lake, N.J.

- (1) Hf and Ti, elements with $k < 1$, are depleted at the change in cross section.
- (2) W and Co, elements with $k > 1$, are enriched at the change in cross section.
- (3) The absolute and relative segregation of hafnium are the most significant.
- (4) The relative and absolute segregation of cobalt are the least significant.
- (5) As the hafnium content increases, the extent of segregation of other alloying elements increases.

Similar results have been observed by Piwonka et al(2).

The effects of macrosegregation on the microstructure can be seen by comparing the photomicrographs shown in Figures 5.5 and 5.6. Figures 5.5a and 5.6a represent areas in regions without segregation. Figures 5.5b and 5.6b are from areas of negative segregation. The negative segregation results in a substantial reduction in the eutectic constituent for the alloy with 2.5% Hf. The change in eutectic fraction is much less noticeable in the MAR-M200 without Hf. Figures 5.7 summarizes per cent eutectic for the directionally solidified ingots measured at the positions shown in Figure 5.3b.

The segregation pattern at the chill is not as apparent as at the change in cross section. For the most part, the samples show positive macrosegregation at the chill surface. In the regions comparable to position E of Figure 5.1, no segregation was observed. Since there is porosity in this region, it is probable the lack of segregation is due to the lack of feeding.

5.4 Summary

As the result of this simple screening test, it has been demonstrated that these nickel base superalloys are susceptible to macrosegregation due to geometric effects. By analogy macrosegregation would result from changes in cooling conditions. Hafnium segregates to the greatest extent. Tungsten and titanium also show substantial segregation. The hafnium level has a strong influence to increasing amplitude of segregation of the other elements. Macrosegregation leads to variations in the solidification microstructure, notably the eutectic fraction.

5.5 References

1. M.C. Flemings, "Solidification Processing," Chapter 7, (New York: McGraw-Hill, 1974).
2. T.S. Piwonka and L. Graham, TRW, personal communication.

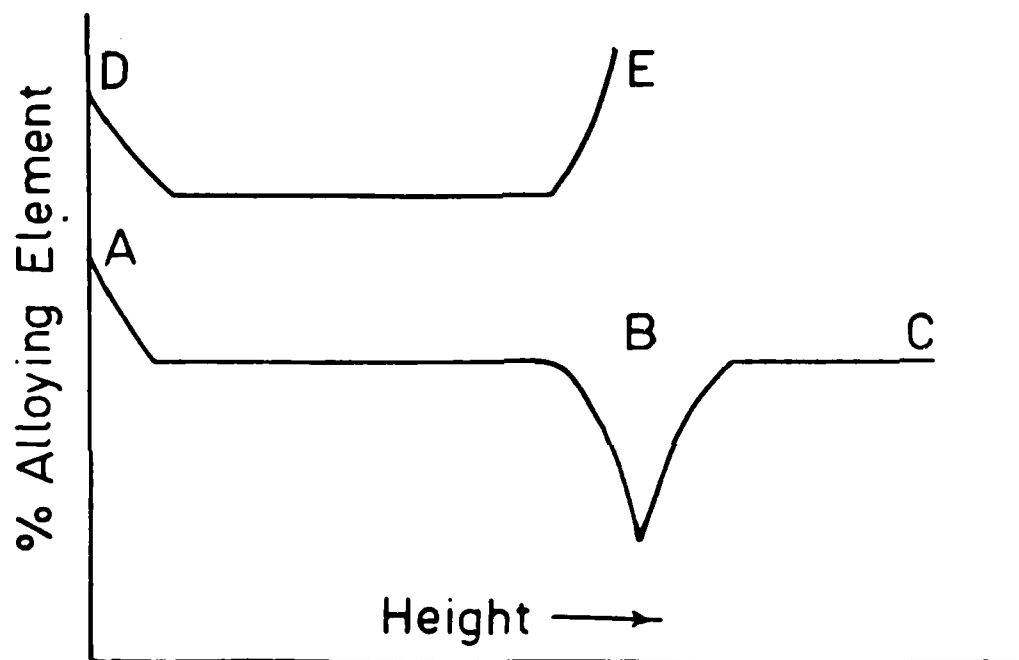
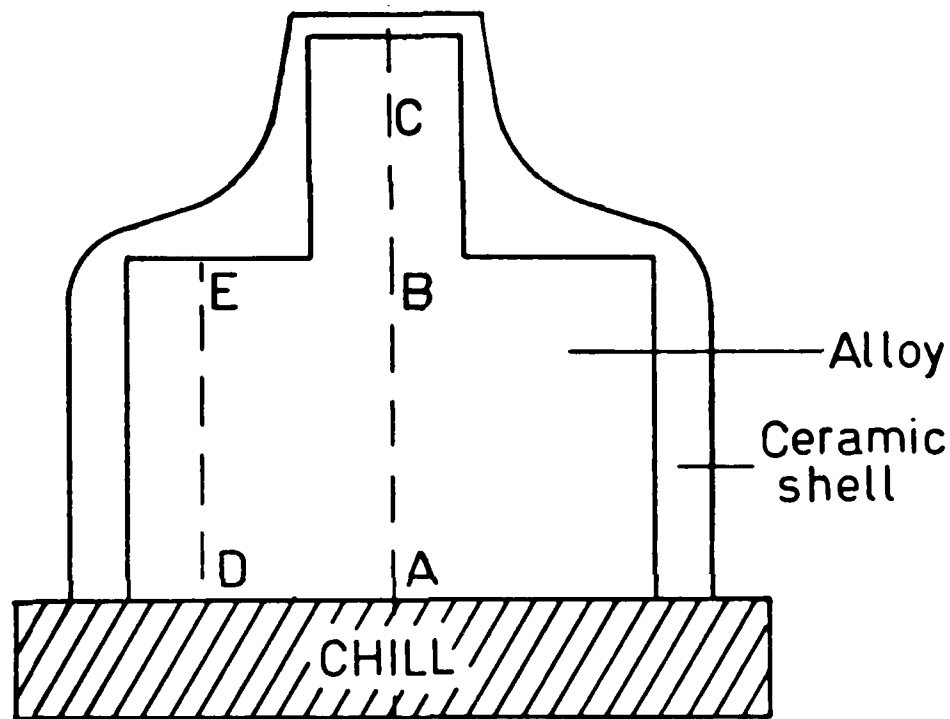
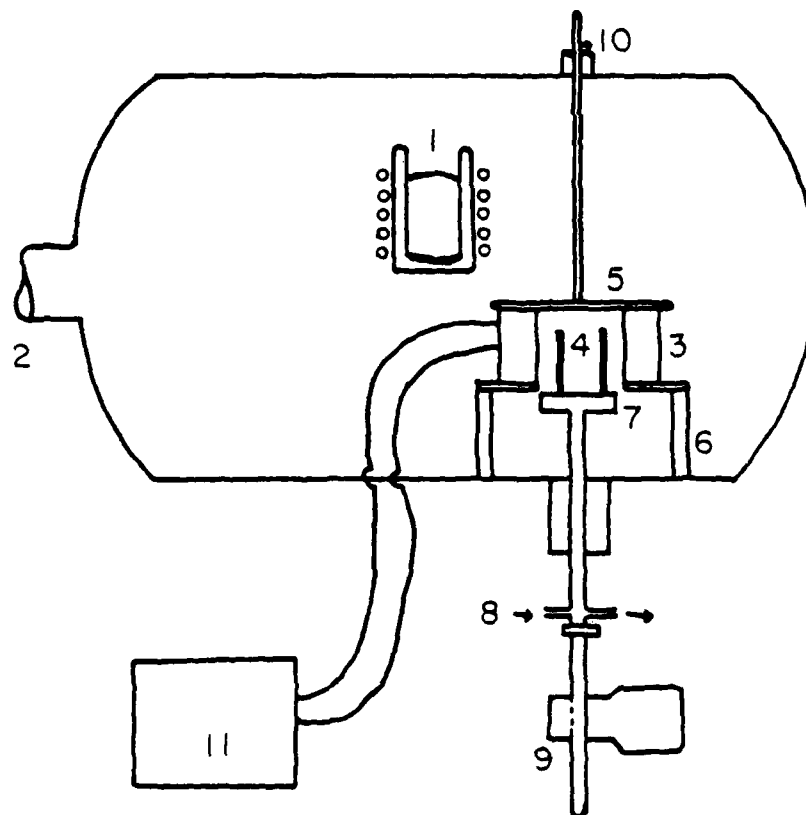


Figure 5.1: Schematic representation of change in cross section mold (top) to evaluate macrosegregation tendencies of an alloy and indication of the macrosegregation profiles (bottom) expected along lines ABC and DE for alloys showing macrosegregation as the result of flow of enriched liquid to feed shrinkage.



- 1 INDUCTION FURNACE
- 2 ATTACHMENT TO VACUUM PUMP
- 3 MOLD HEATING FURNACE
- 4 MOLD
- 5 MOLD COVER
- 6 SUPPORT
- 7 CHILL
- 8 COOLING WATER INLET & OUTLET
- 9 MOLD WITHDRAWAL SYSTEM
- 10 MOLD COVER LIFTING SYSTEM
- 11 AUXILIARY POWER SUPPLY UNIT

(a)

Figure 5.2: Apparatus for directional solidification casting;
(a) overall view, schematic

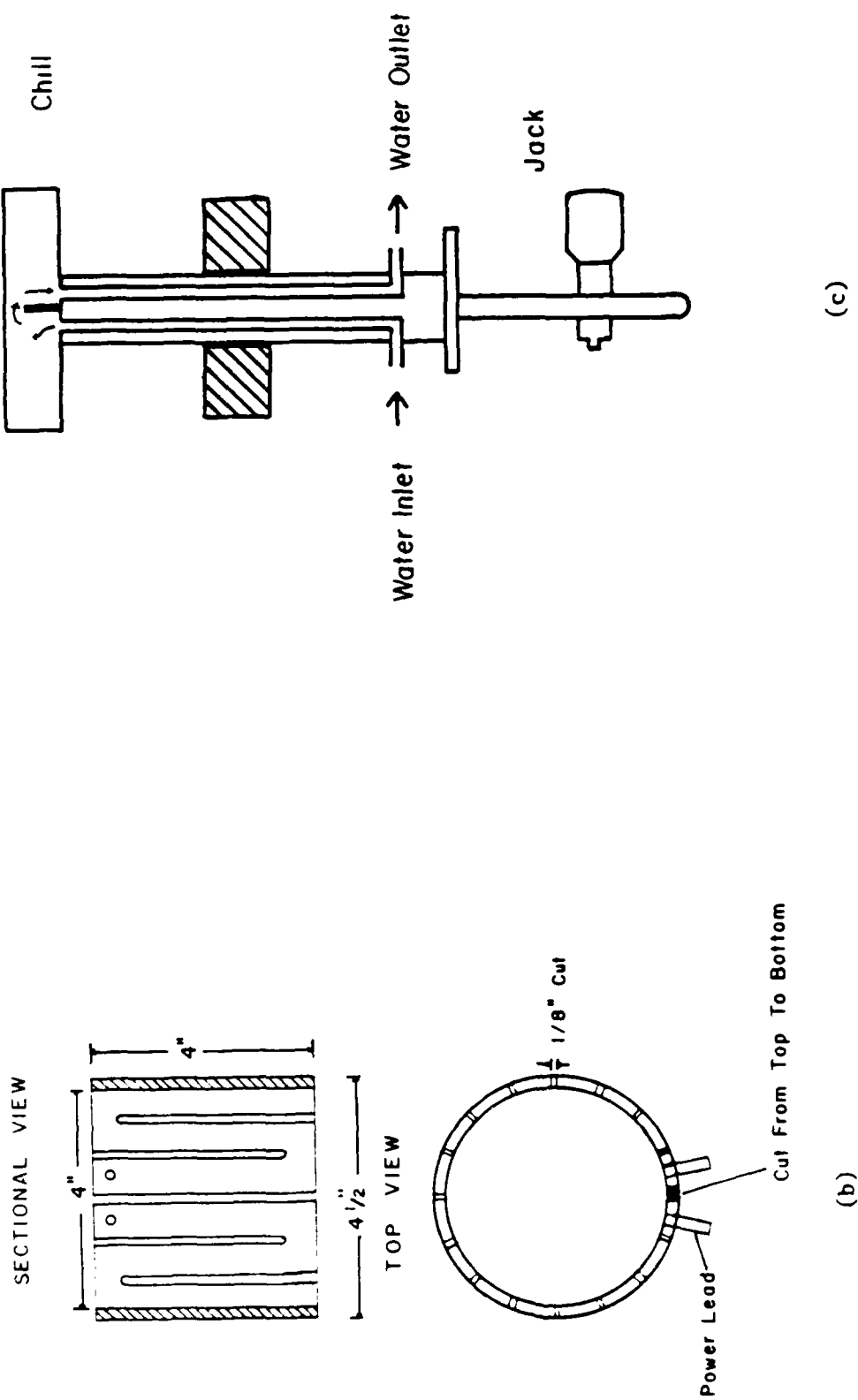
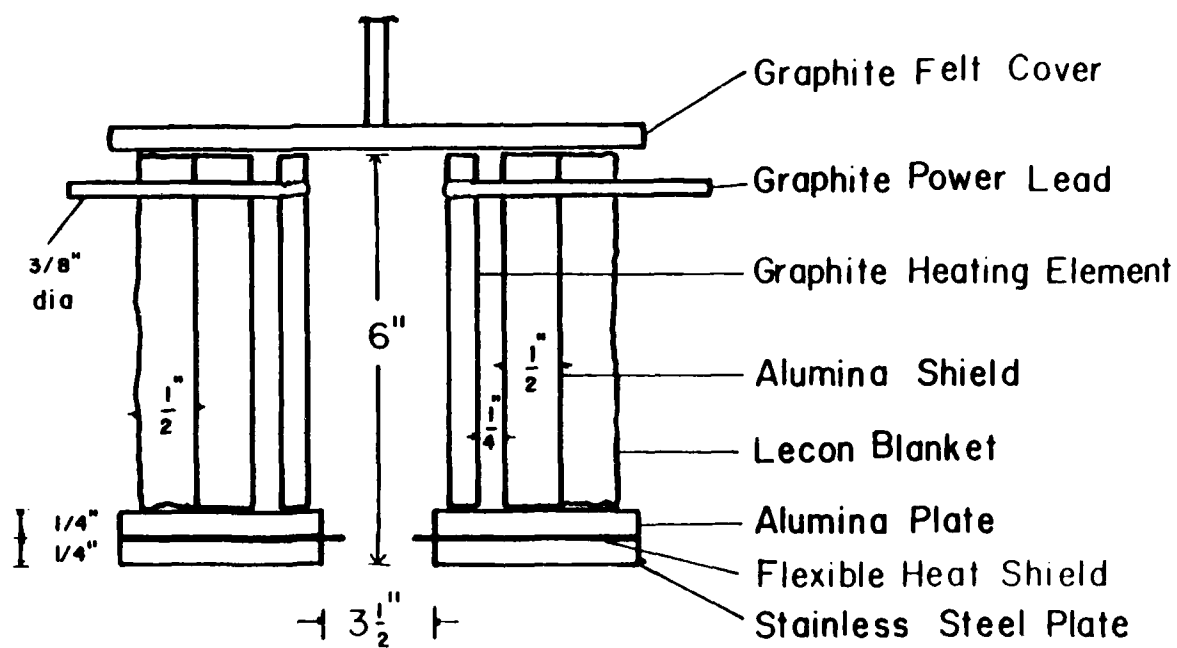
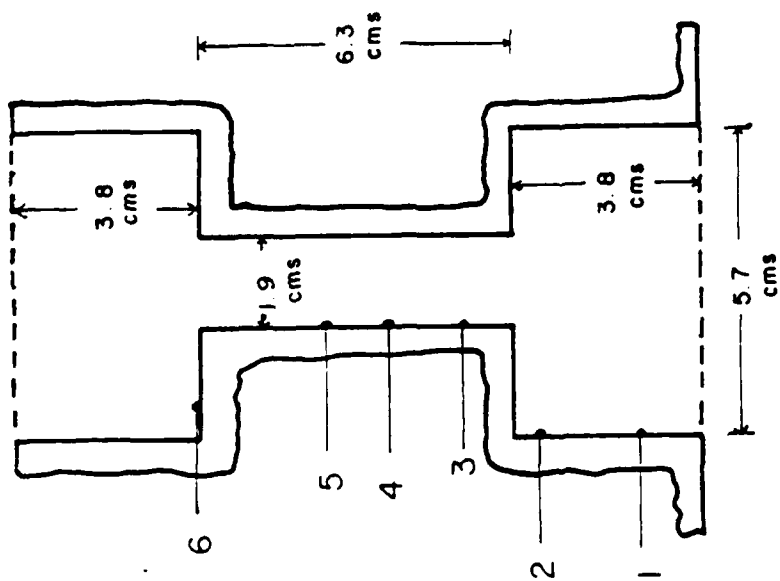


Figure 5.2 (continued): (b) Schematic of the graphite heating element used in the mold heating furnace, and (c) schematic of water-cooled copper chill and withdrawl system.



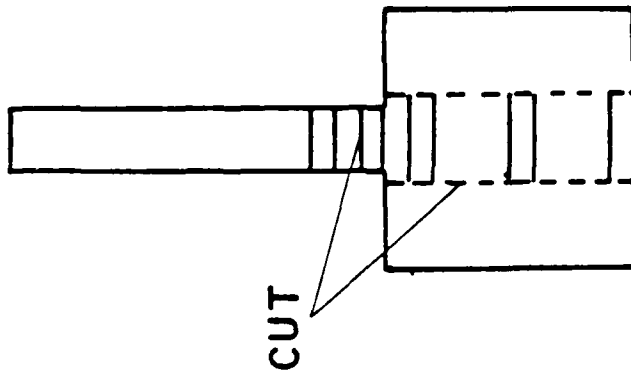
(d)

Figure 5.2 (continued): (d) Mold heating furnace, schematic.



1-6 Thermocouples

(a)



(b)

Figure 5.3: (a) Diagram of investment mold showing the thermocouple positions, and (b) diagram illustrating the procedure for cutting surfaces for x-ray and metallographic analyses.

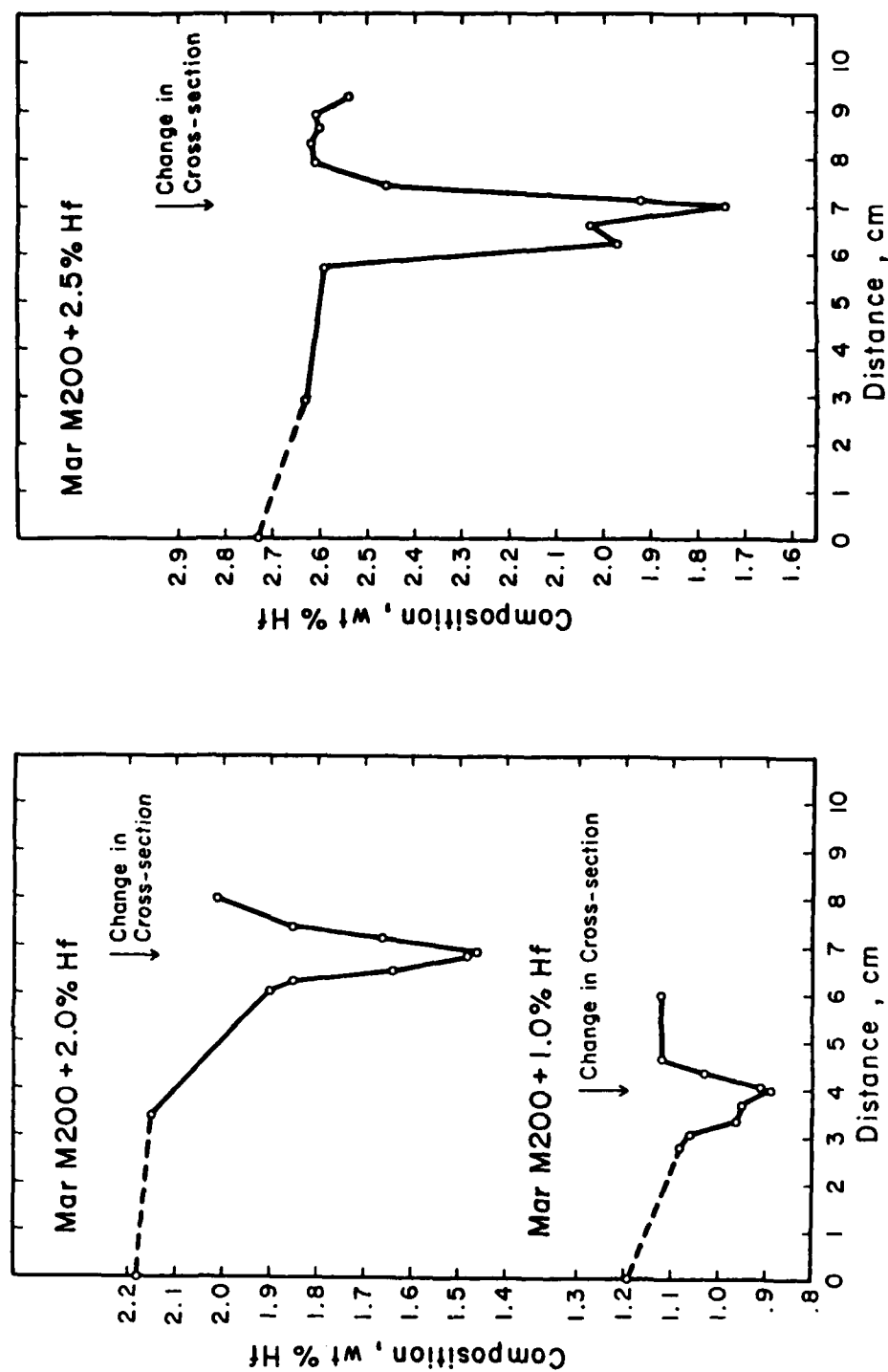


Figure 5.4a: Variation of hafnium content with distance from the chill in unidirectionally solidified ingots with an abrupt change in cross section for Mar-M200 alloys modified with 1.0%, 2.0%, and 2.5% Hf.

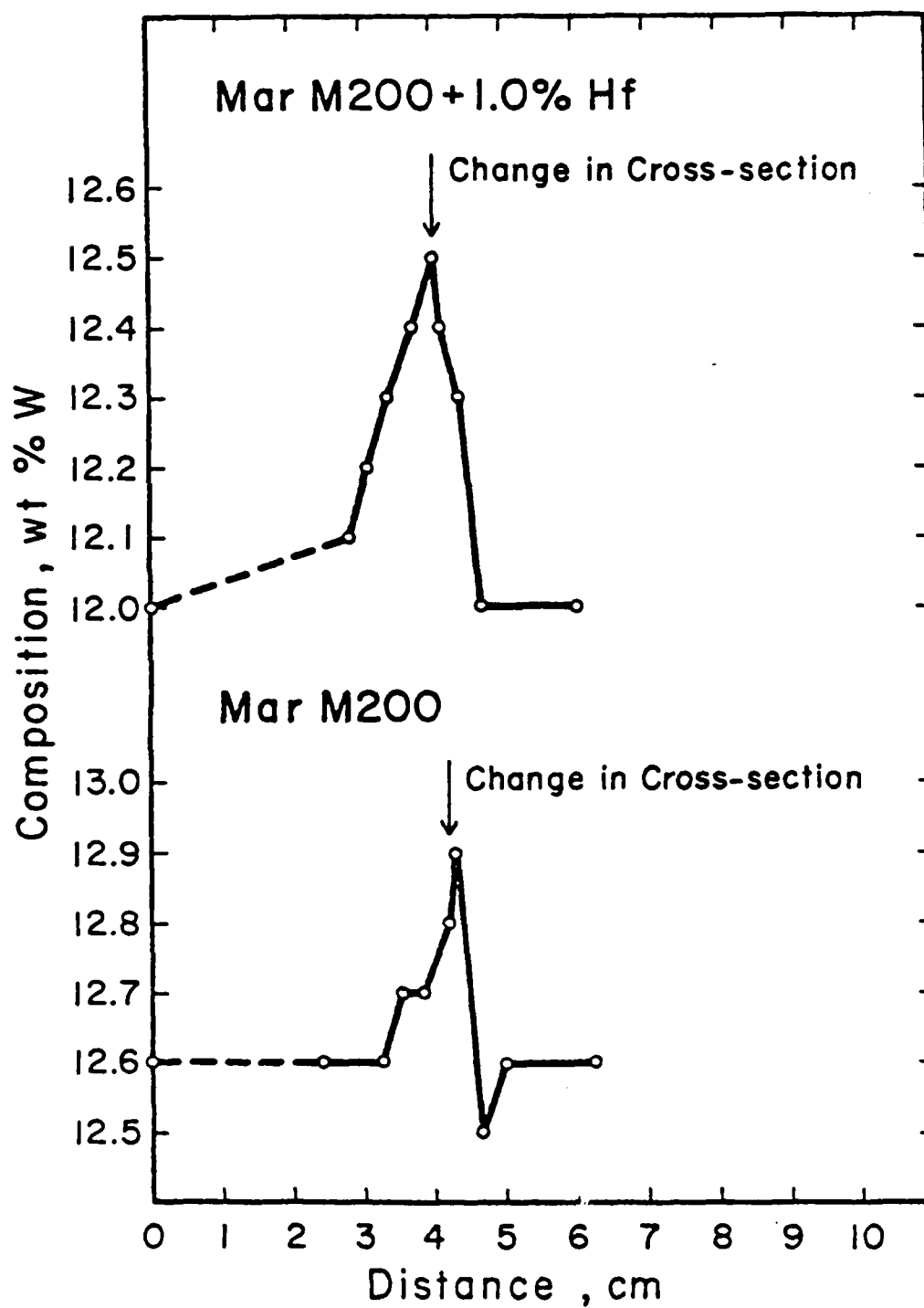


Figure 5.4b: Variation of tungsten content with distance from the chill for unidirectionally solidified ingots with an abrupt change in cross section for Mar-M200 and Mar-M200 + 1% Hf alloys.

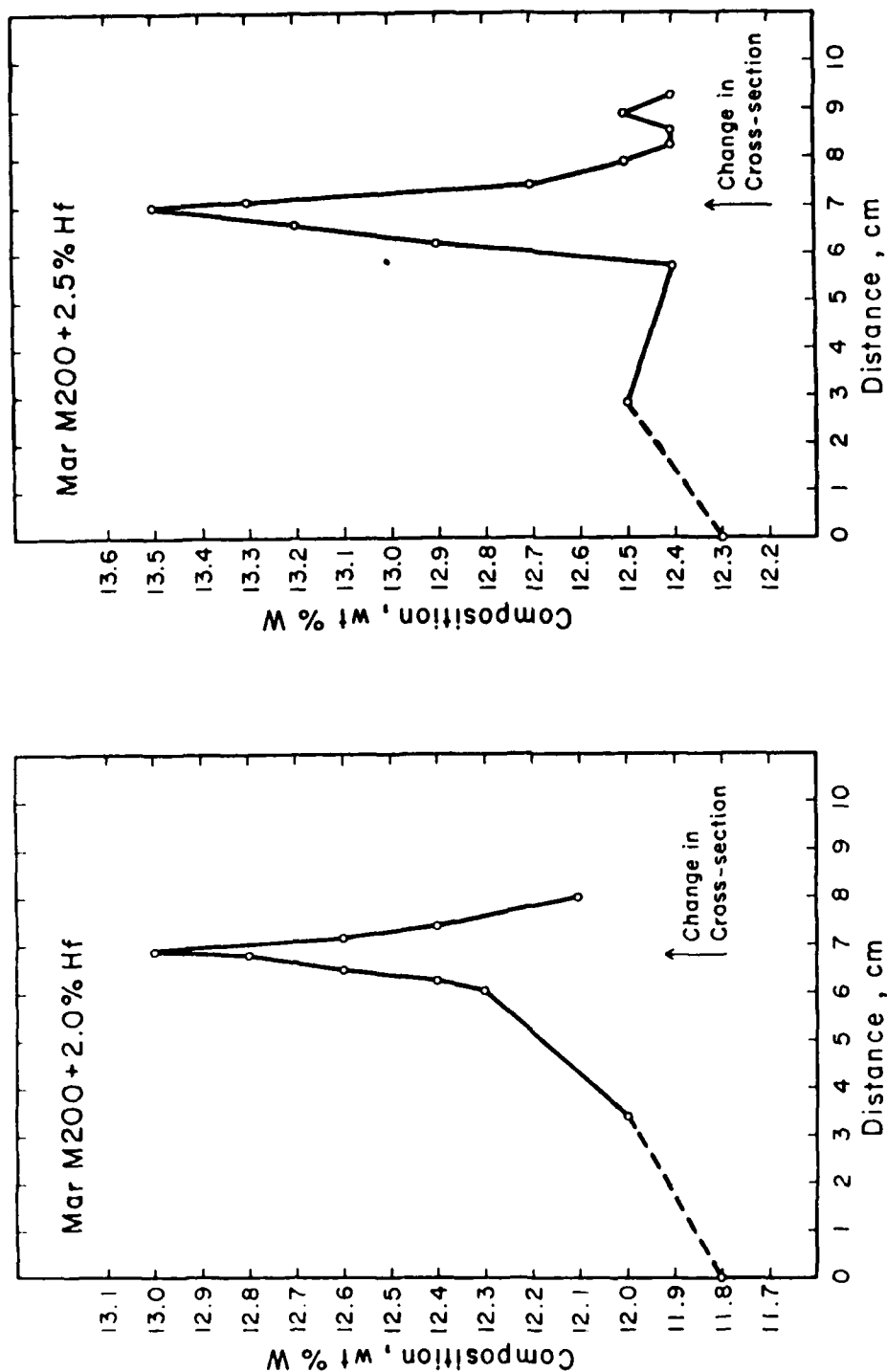


Figure 5.4b (continued): Variation of tungsten content with distance from the chill for unidirectionally solidified ingots with an abrupt change in cross section for Mar-M200 + 2% Hf and Mar-M200 + 2.5% Hf alloys.

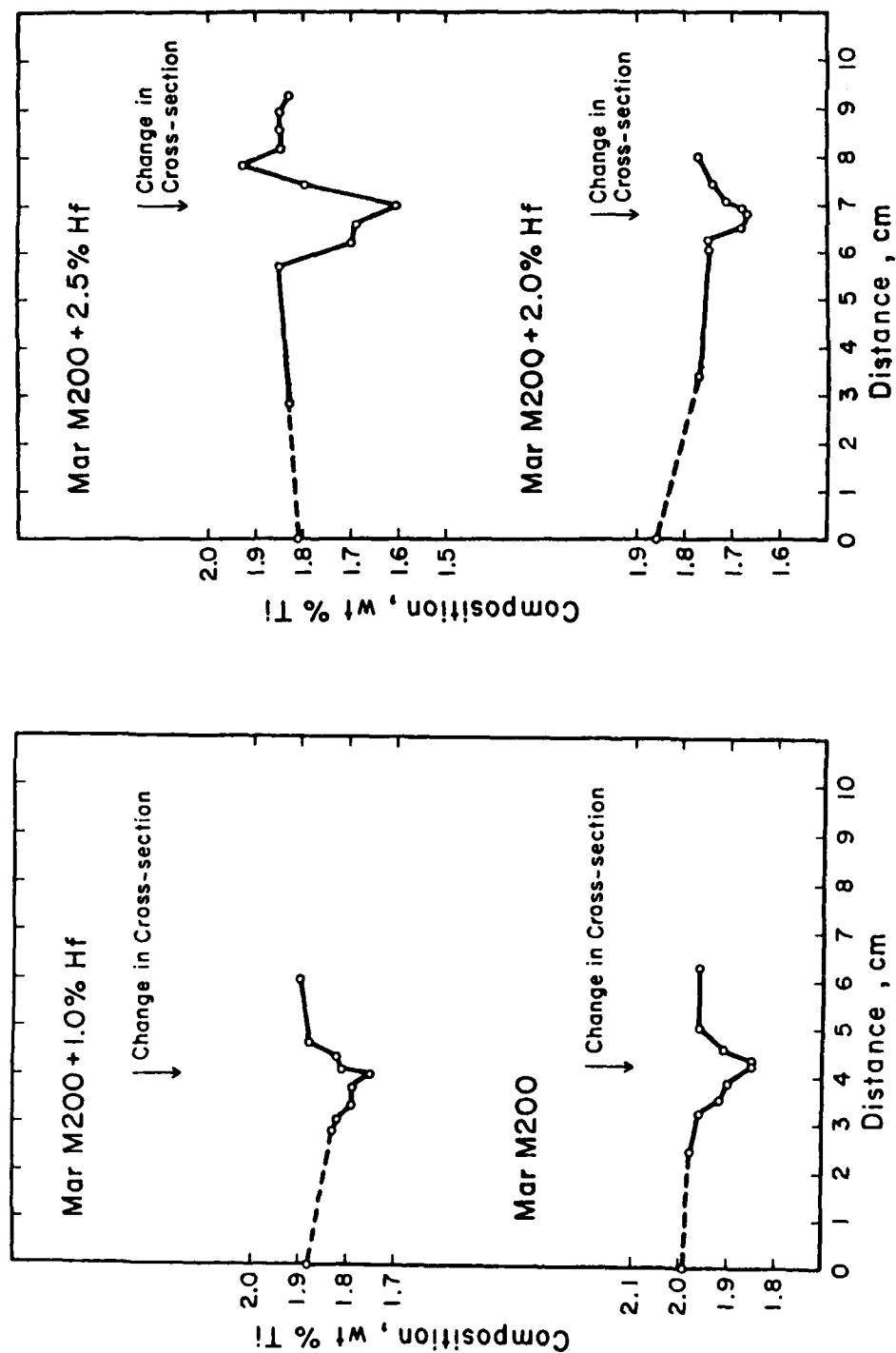


Figure 5.4c: Variation of titanium content with distance from the chill for unidirectionally solidified ingots with an abrupt change in cross section for Mar-M200 alloys modified with 0%, 1%, 2% and 2.5% Hf.

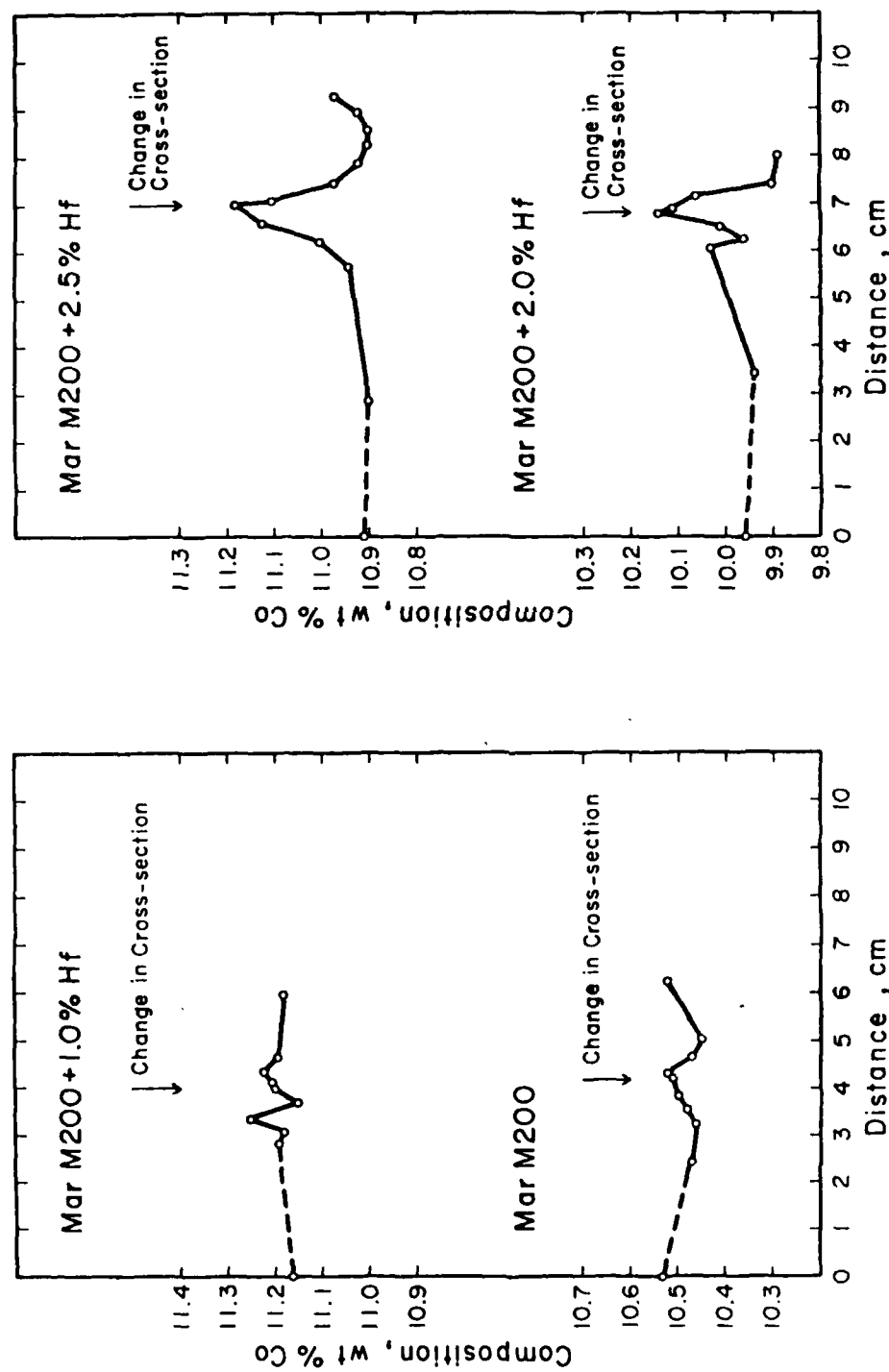


Figure 5.4d: Variation of cobalt content with distance from the chill for unidirectionally solidified ingots with an abrupt change in cross section for Mar-M200 alloys with 0%, 1%, 2%, and 2.5% Hf.

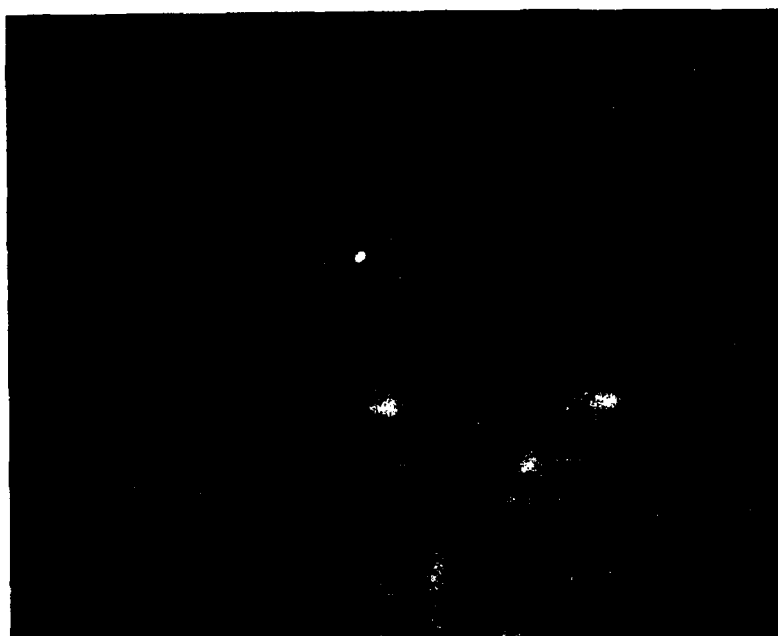


Figure 5.5: Optical micrographs illustrating the variation in the amount of eutectic (white pools) in Mar-M200 alloy at a nominal location (top) and at the abrupt change in cross-section (bottom) in the D.S. casting, 200X



Figure 5.6: Optical micrographs illustrating the variation in the amount of eutectic (pools) in Mar-M200 + 2% Hf alloy at a nominal location (top) and at the abrupt change in cross-section (bottom) in the D.S. casting, 200X

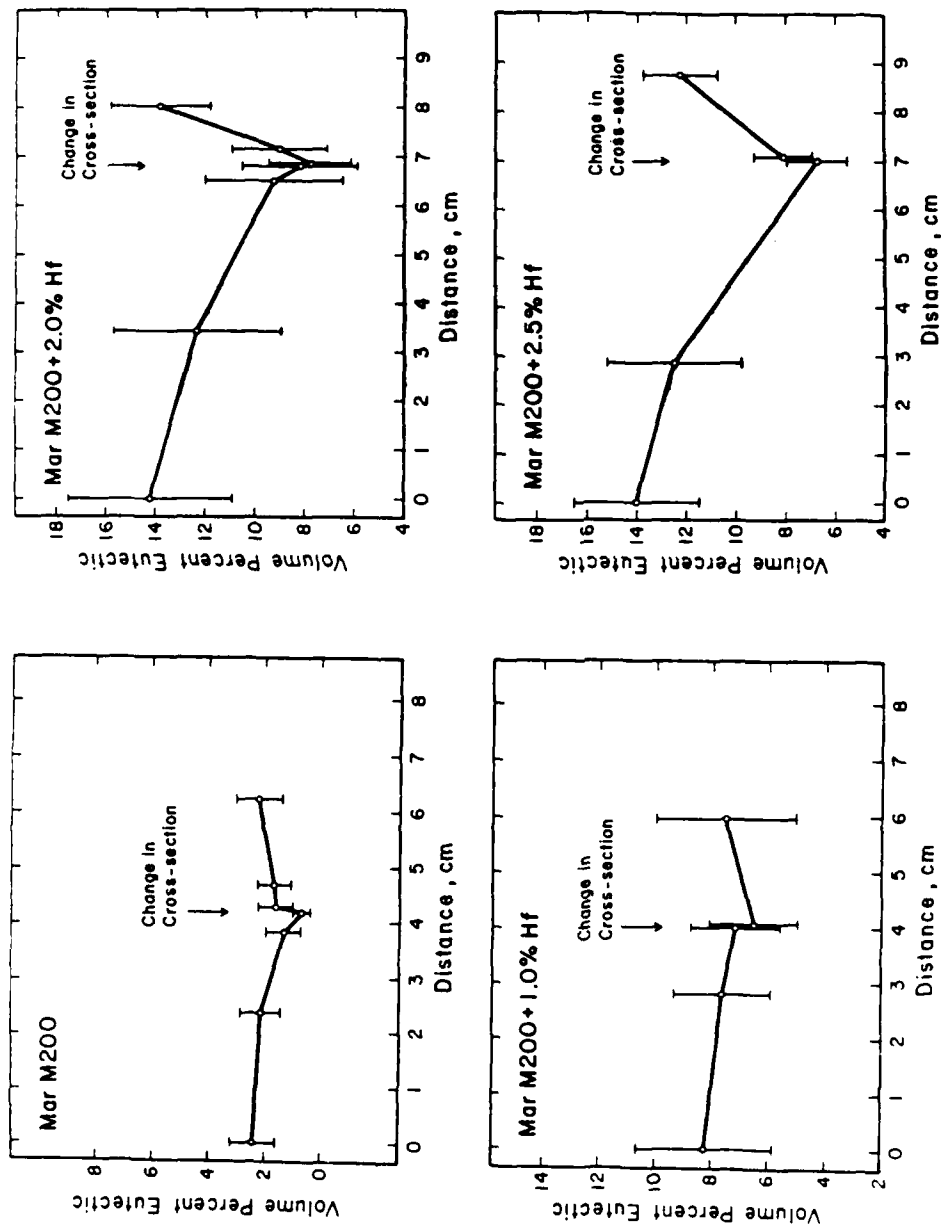


Figure 5.7: Variation of volume percent eutectic with the distance from the chill in unidirectionally solidified ingots with an abrupt change in cross section for Mar-M200 modified with 0%, 1%, 2%, and 2.5% Hf.

6.0 Task V: Analyses of Airfoil Shape D. S. Castings

6.1 Purpose

Tasks I-IV described in the previous sections have been aimed at obtaining fundamental information on the relation between solidification microstructure and casting variables. Particular emphasis has been placed on analysis of primary and secondary dendrite arm spacing, carbide morphology and size, and eutectic volume fraction. Emphasis on casting parameters has been on cooling rate, thermal gradient, and growth rate effects and on factors that would cause macrosegregation due to fluid flow effects (abrupt changes in geometry and abrupt changes in growth rate). The objective of these fundamental studies was to allow a better assessment of cause and effect occurrences and observations in complex hardware including airfoil shapes. Task V deals with examining the microstructure of some commercially cast airfoil shape D. S. castings to evaluate the microstructure in order to complement the fundamental information within a limited range of current commercial practice.

6.2 Approach

Complex airfoils of PWA 1422 (hafnium modified MAR-M200) were obtained in the as-cast condition from three vendors in two geometries as indicated in Table 6.1. The microstructural analysis was consistently done according to the scheme in Figure 6.1. The specimen preparation procedures were identical to those given in Section 3.2.2 for Task II. The airfoils are shown in Figure 6.2 in the as-etched condition.

6.3 Results

Carbide and dendrite photomicrographs are presented for each of the four combinations of vendor and airfoil in Figures 6.3 through 6.10. The carbides and then the dendrites are shown for each vendor/blade combination as a unit for the convenience of the reader. All carbide photos are 500X.

6.3.1 Carbides

Vendors A and B can be associated with blocky MC carbides; while vendor C always appears with script carbides. The distinction is quite clear. The blocky carbides are medium to coarse, while the script carbides are fine to medium.

6.3.2 Dendrite Morphology

In terms of dendritic features the results are slightly more subtle, but vendor C has clearly produced the finest primaries and secondaries, while vendor A is associated with the coarsest features. The range of secondary spacings is 30-80 μ m. More detailed results are shown

in Table 6.2. It can be seen that the dendritic structures coarsen as growth proceeds from root to airfoil in all cases. (This observation is consistent with root down casting).

The sharpness of dendrite images was observed to be best for grains growing along the cube direction. Poor results are obtained when interfacial curvature is present, possibly due to dendrite migration along transverse thermal gradients(1). (This was especially noticeable at low Hf levels in bars solidified in the LMC apparatus.) Interfacial curvature is more common in shaped parts than in uniform cross sections. Note the secondary branching in the case of Vendor C at the top airfoil location (Figure 6.6c). This tendency can be associated with sudden changes in cross section, sudden increases in withdrawal rate, low axial thermal gradient and/or poor baffling.

Residual stress probably also plays a role in determining the fuzziness of dendrite images. Stress is introduced by differential thermal contraction in cored castings, cutting and polishing. Stress relief can occur at low cooling rates. Polishing stresses are minimized by alternately polishing and etching.

The primary dendrites appear best at intermediate cooling rate. This is probably due to the exposure to a high enough cooling rate to minimize interdiffusion of the microsegregation wave but low enough to allow some recovery and avoid excessive interfacial curvature.

6.3.3 Eutectic Volume Fraction

The volume fraction of eutectic constituent was measured at selected locations in the airfoil shapes: (a) root, (b) transition region through the platform, (c) lower airfoil, and (d) upper airfoil. The eutectic volume fraction measurements are reasonably accurate in that point counting was used with a systematic grid of 100 points randomly applied at 15 locations. These 1500 points should lead to a standard deviation(2) of approximately 2.6% of the amount present. For example, a measurement of 18 vol.% would be equivalent to $18 \pm 0.5\%$.

The results of volume percent eutectic measurements are presented in Table 6.3. For the first blade from both vendors A and C, the root measurements are close to average, the transition and upper airfoil measurements are higher than average and the lower airfoil measurements are lower than average. For vendor A the average for the first blade is 17.6% eutectic with a range of 9.2%. The range is 52% of the average. For vendor C the average eutectic volume for the first blade is 11.1% with a range of 7.5%. The range is 68% of the average. For the second blade from vendors A and B the pattern of eutectic variation is not consistent and the range of variability is considerably narrower, 27% and 19%.

Most of the measurements are within the expected range of 10-20 vol.%. The second blade does not change drastically in cross section from root to lower airfoil, and one would not expect macrosegregation

due to feeding or shrinkage. The first blade, however, shows a larger decrease in section size from root to airfoil, and there is definitely a drop in volume percent eutectic in the lower airfoil and, presumably, a decrease in the composition of some elements, notably Hf and Ti, and an increase in the composition of some elements, notably W.

6.4 Discussion

More detailed discussion of these results in comparison to the results of fundamental studies is presented in the next section. It appears, however, that features of solidification microstructure in the airfoil shapes are comparable to those produced in the bars, plates, and ingots cast under controlled conditions. Detailed comparisons would require experimental measurement or modeling of the complex hardware shapes. It is clear, however, that vendor C used the highest cooling rates and vendor A the lowest, based on carbide and dendrite morphologies. It is more important to carefully control growth conditions for the first blade, irrespective of vendors, and to monitor castings for microstructural variation due to macrosegregation.

6.5 References

1. D.J. Allen and J.D. Hunt, "Melting During Solidification," Met. Trans., 7A, No. 5 (1976) 767-770.
2. J.E. Hilliard and J.W. Cahn, "An Evaluation of Procedures in Quantitative Metallography for Volume-Fraction Analysis", Trans. TMS-AIME, 221 (1961) 344-352.

Table 6.1: Airfoil Analysis Matrix for Turbine Blades

Vendor	First Blade	Second Blade
A	6.3, 6.4	6.7, 6.8
B	----	6.9, 6.10
C	6.5, 6.6	----

Notes: The selection allows for a comparison of both blades from the same vendor (A) and two vendors for the same blade (A and C for first blade, A and B for second blade). Numbers indicate figures containing photomicrographs for the vendor/blade combination.

Table 6.2: Cast Airfoil Dendrite Spacings

		First Blade		Second Blade	
		S_1	S_2	S_1	S_2
Vendor A	Root	220 μ m	--	--
	Trans.	302	77	250	53
	AF	326	--	--
Vendor B	Root	N.A.	N.A.	248	--
	Trans.	N.A.	N.A.	266	47
	AF	N.A.	N.A.	289	--
Vendor C	Root	--	N.A.	N.A.
	Trans.	200	40	N.A.	N.A.
	AF	--	N.A.	N.A.

Code: N.A. - Not Acquired
 -- - Not Measured Due to Sectioning Scheme
 - Not Measured Due to Interface Curvature

Table 6.3: Volume Fraction Eutectic in Airfoil Shapes

Vendor/ Blade	A/ First	A/ Second	B/ Second	C/ First
Root	16.1	15.9	21.6	10.5
Transition	22.6	18.7	20.9	12.3
Lower Airfoil	13.4	14.4	21.4	7.0
Upper Airfoil	18.3	15.0	17.6	14.5
Average	17.6	16.0	20.4	11.1
Range	9.2	4.3	4.0	7.5

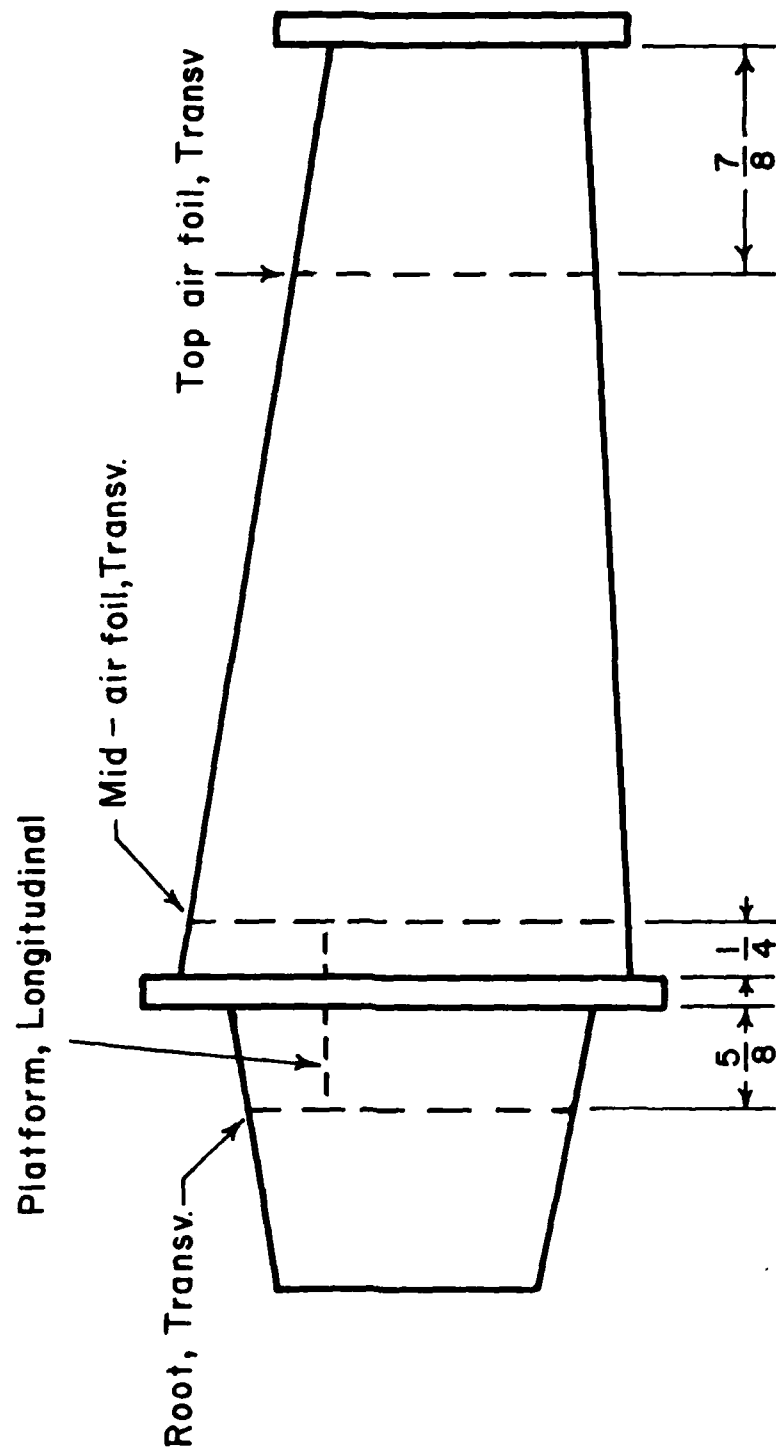
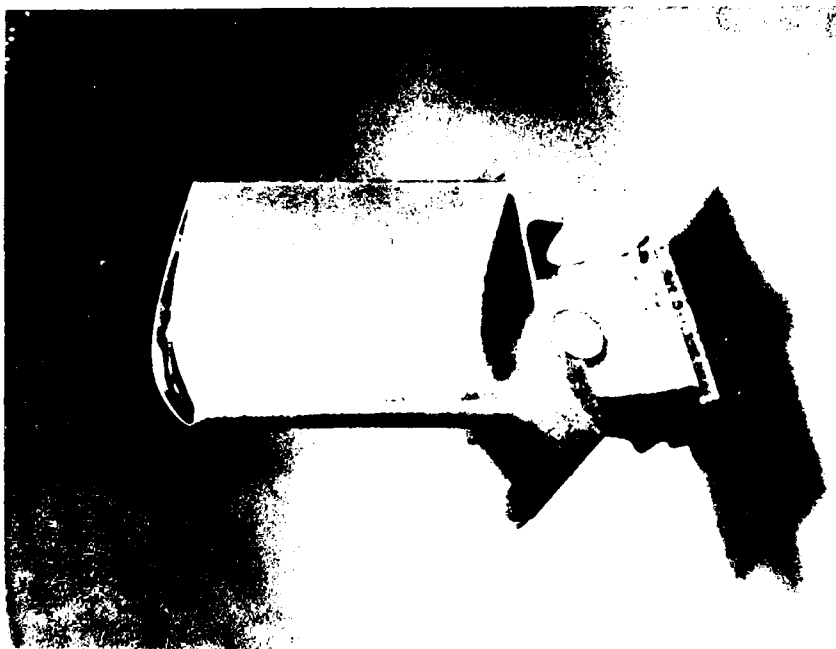
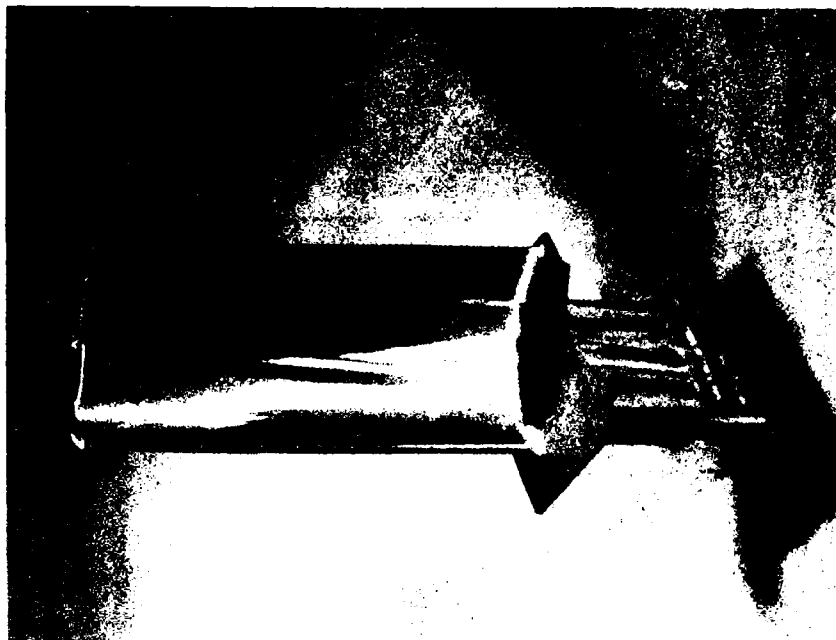


Figure 6.1: Schematic drawing of microstructural section layout for all turbine blades.
All dimensions are in inches.



First Turbine Blade
Blade height = 8 cm.



Second Turbine Blade
Blade height = 10.3 cm.

Figure 6.2: Macro-etched turbine airfoils. Directionally solidified blades have been sand-blasted and etched to show grain structure.



Figure 6.3a: Longitudinal view of platform region. Unetched.
Vendor A, first turbine blade, 500X.



Figure 6.3b: Transverse view in root section. Vendor A,
first turbine blade, 500X.



Figure 6.3c: Transverse view near airfoil top. Vendor A, first turbine blade, 500X.

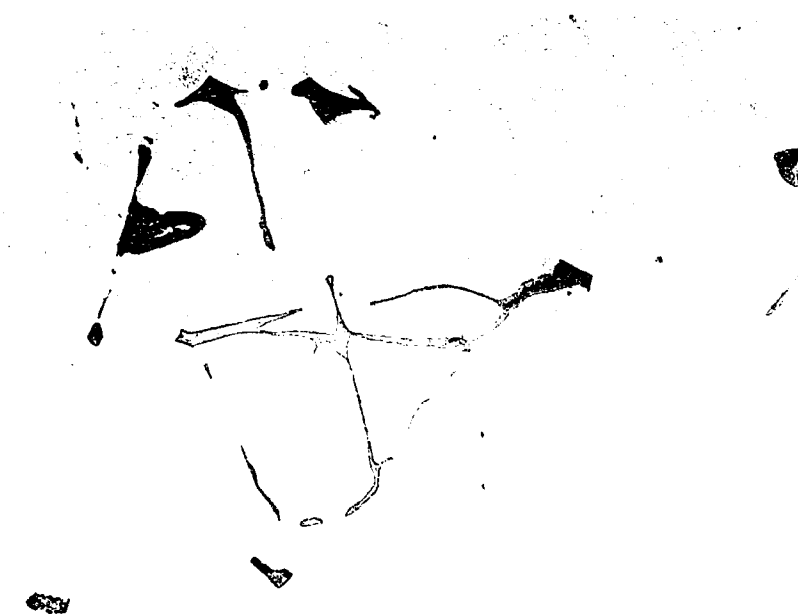


Figure 6.3d: Transverse view at mid-airfoil. Vendor A, first turbine blade, 500X.



Figure 6.4a: Longitudinal view near platform, full etch.
Vendor A, first turbine blade, 100X.



Figure 6.4b: Transverse view in root section. Vendor A,
first blade, 100X.

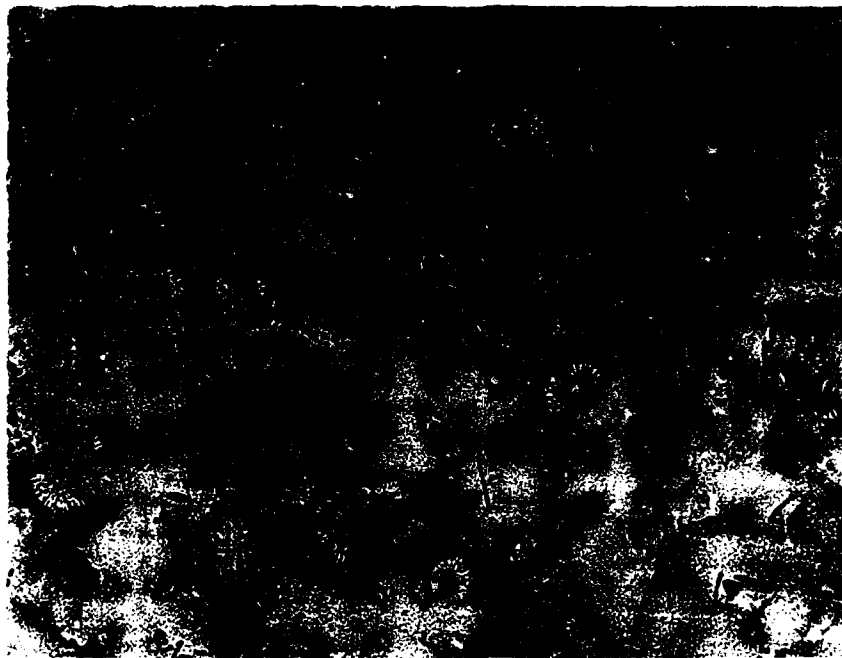


Figure 6.4c: Transverse view at top of airfoil. Vendor A, first blade, 100X.

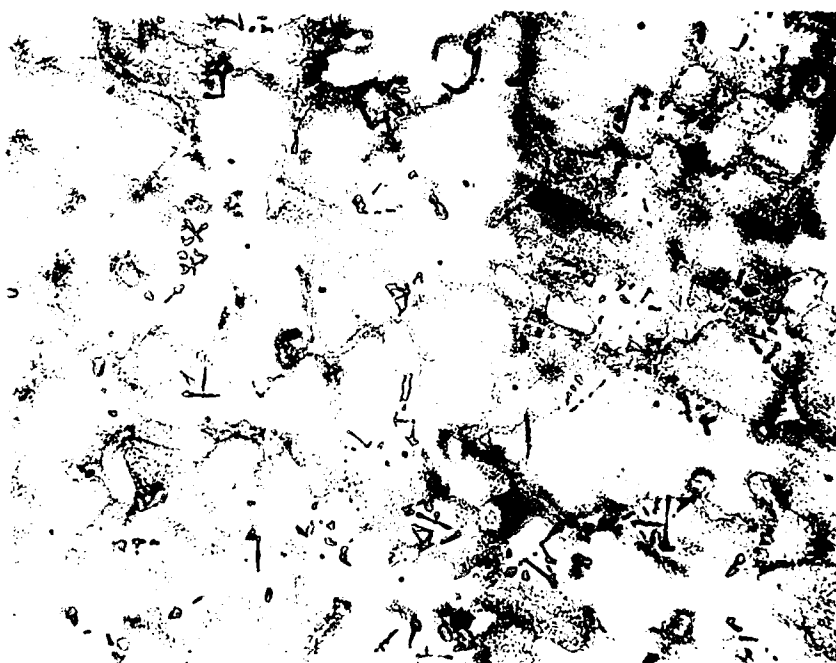


Figure 6.4d: Transverse view at mid-airfoil. Vendor A, first blade, 100X.

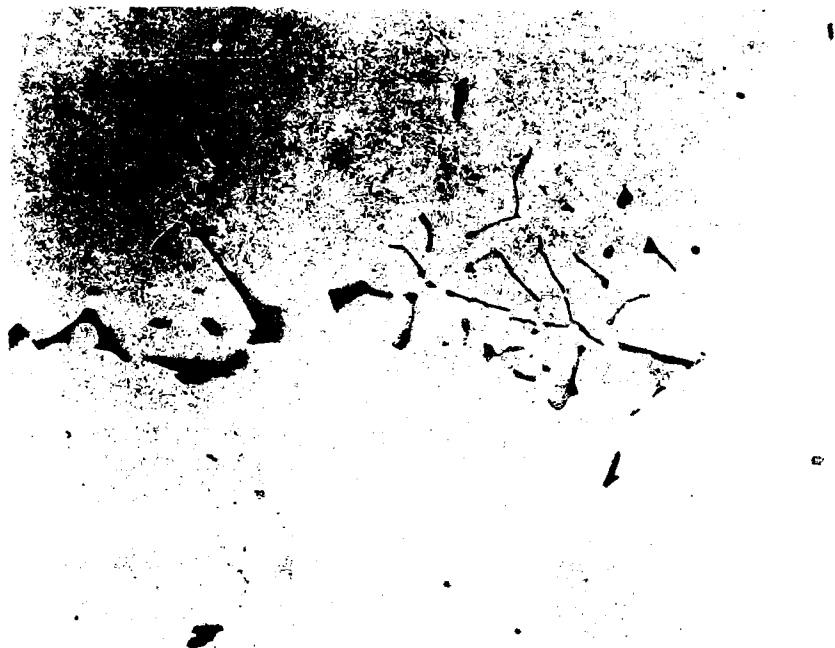


Figure 6.5a: Longitudinal view near platform, unetched.
Vendor C, first blade, 500X.

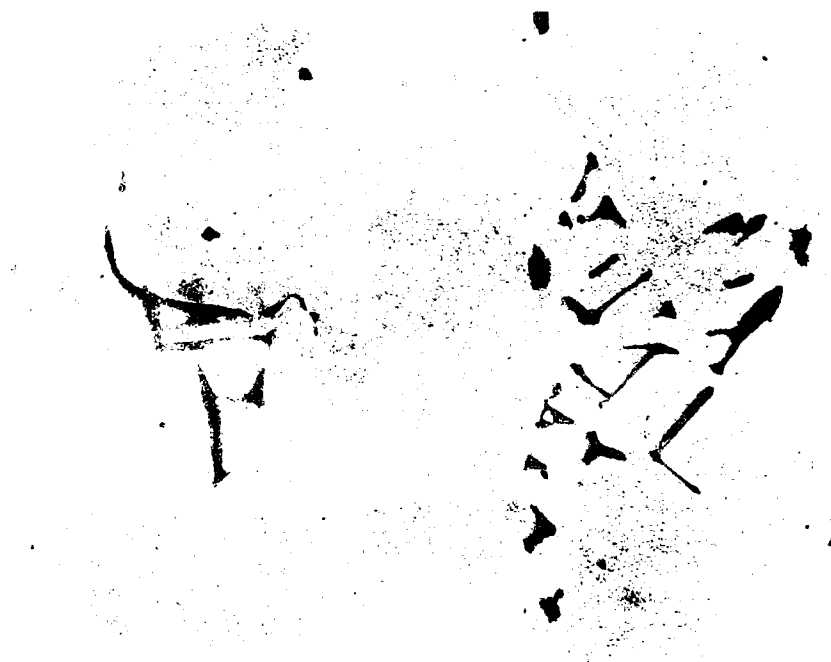


Figure 6.5b: Transverse view through root. Vendor C,
first blade, 500X.



Figure 6.5c: Transverse view near airfoil top. Vendor C, first blade, 500X.



Figure 6.5d: Transverse view at mid-airfoil. Vendor C, first blade, 500X.



Figure 6.6a: Longitudinal view through platform area, etched.
Vendor C, first blade, 100X.

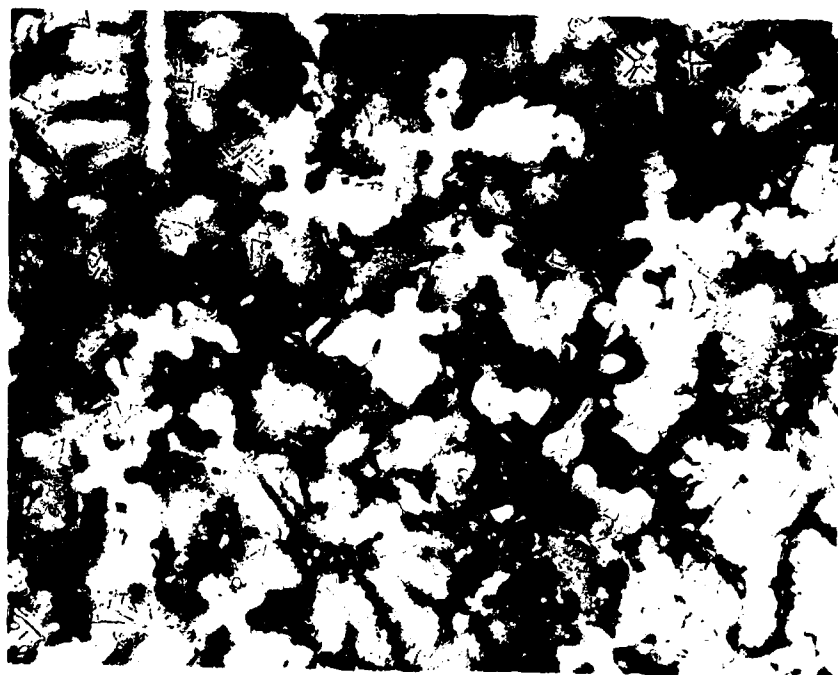


Figure 6.6b: Transverse view through root section.
Vendor C, first blade, 100X.

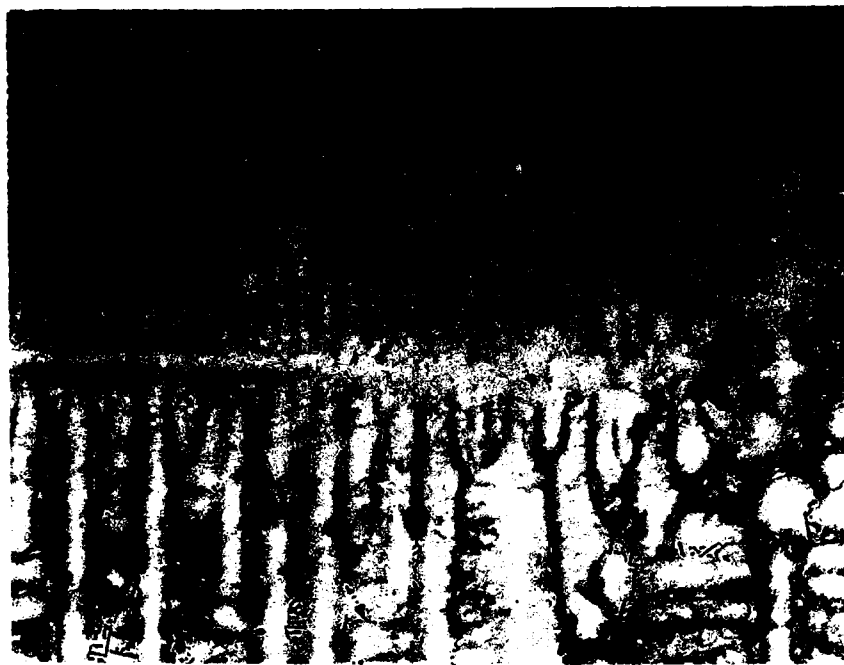


Figure 6.6c: Transverse view near top of airfoil. Vendor C, first blade, 100X.

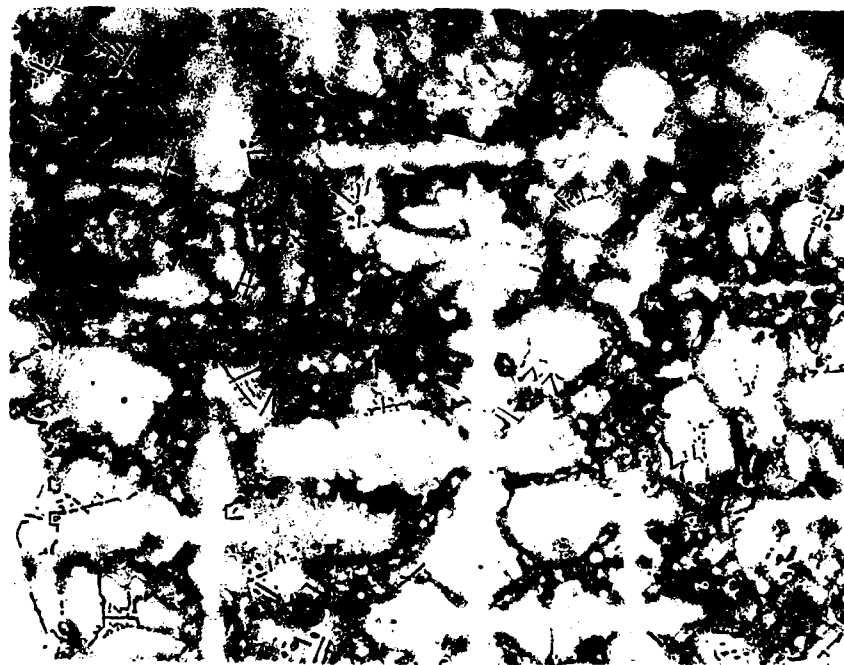


Figure 6.6d: Transverse view at mid-foil. Vendor C, first blade, 100X



Figure 6.7a: Longitudinal view near platform, unetched.
Vendor A, second turbine blade, 500X.



Figure 6.7b: Transverse view in root section. Vendor A,
second blade, 500X.



Figure 6.7c: Transverse view of airfoil top. Vendor A, second blade, 500X.



Figure 6.7d: Transverse view at mid-airfoil. Vendor A, second blade, 500X.



Figure 6.8a: Longitudinal view through platform, etched.
Vendor A, second blade, 100X.



Figure 6.8b: Transverse view through root. Vendor A,
second blade, 100X.

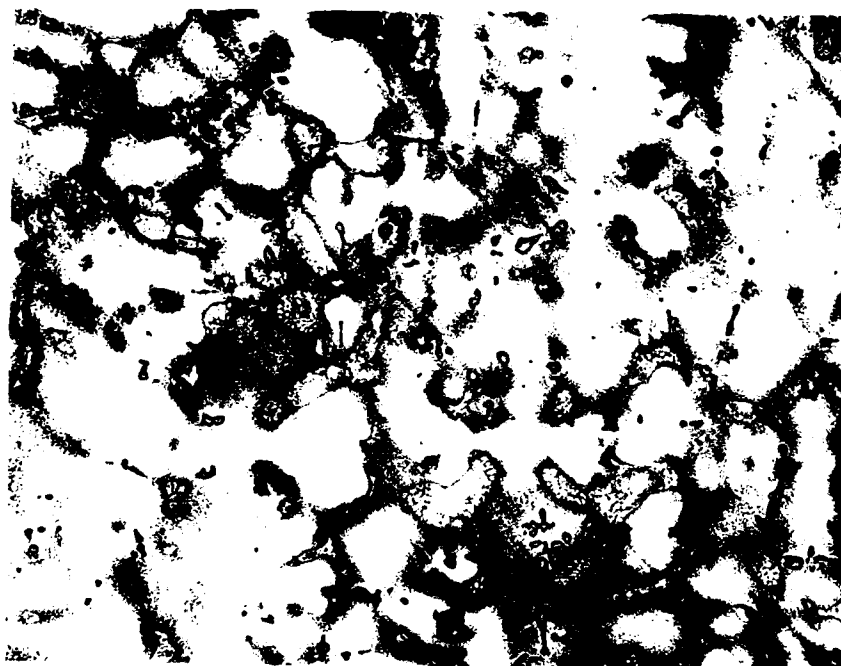


Figure 6.8c: Transverse view, top of airfoil. Vendor A, second blade, 100X.

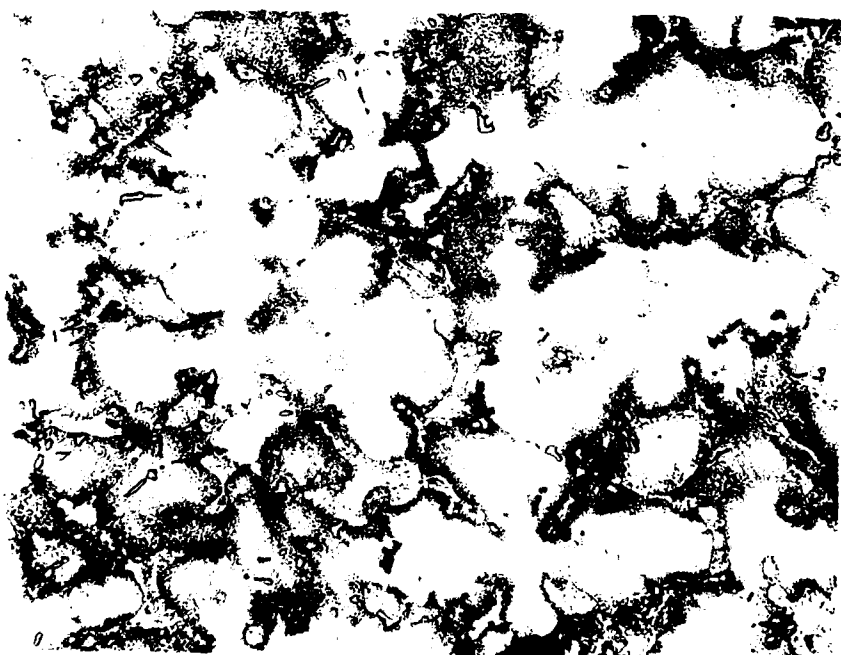


Figure 6.8d: Transverse view at mid-airfoil. Vendor A, second blade, 100X

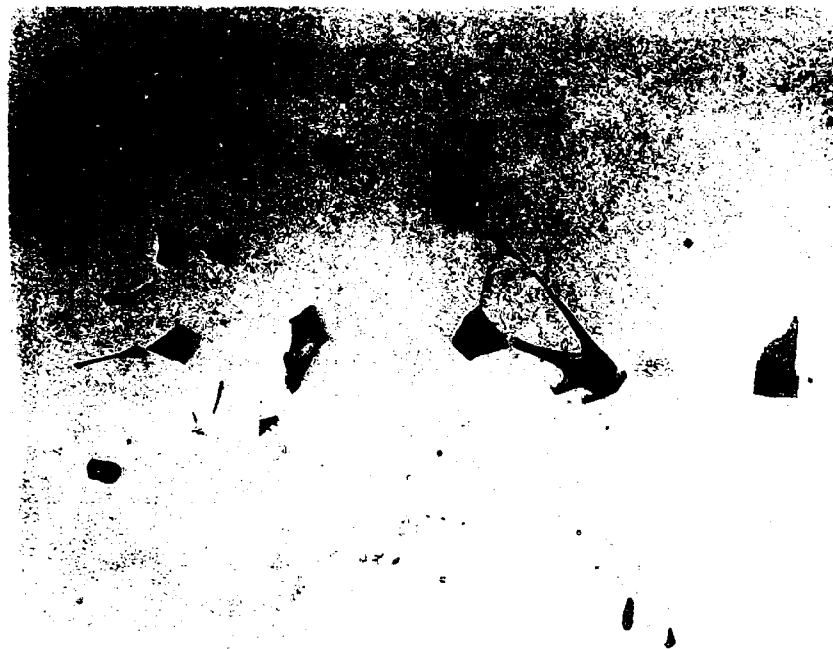


Figure 6.9a: Longitudinal view near platform, unetched.
Vendor B, second blade, 500X.



Figure 6.9b: Transverse view through root. Vendor B,
second blade, 500X.

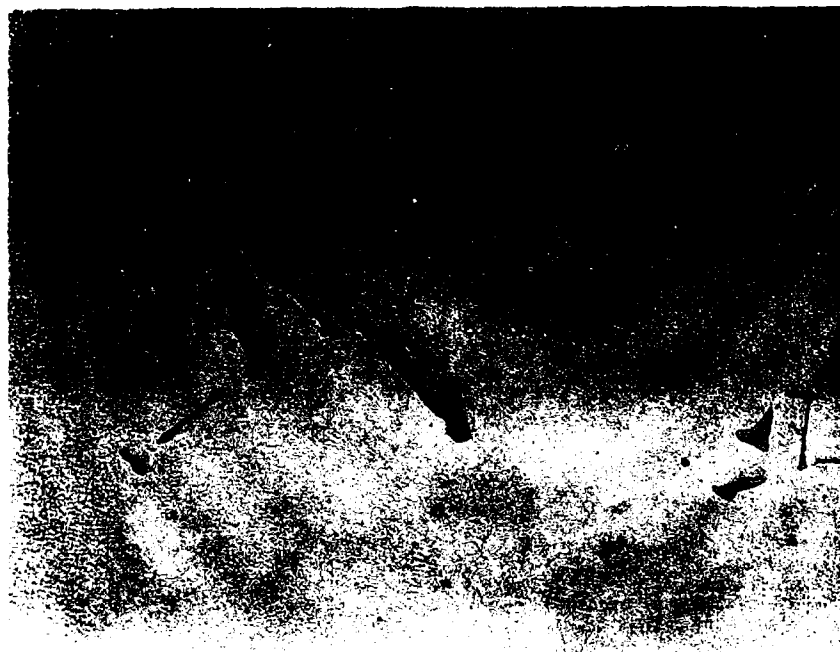


Figure 6.9c: Transverse view near top of airfoil. Vendor B, second blade, 500X.

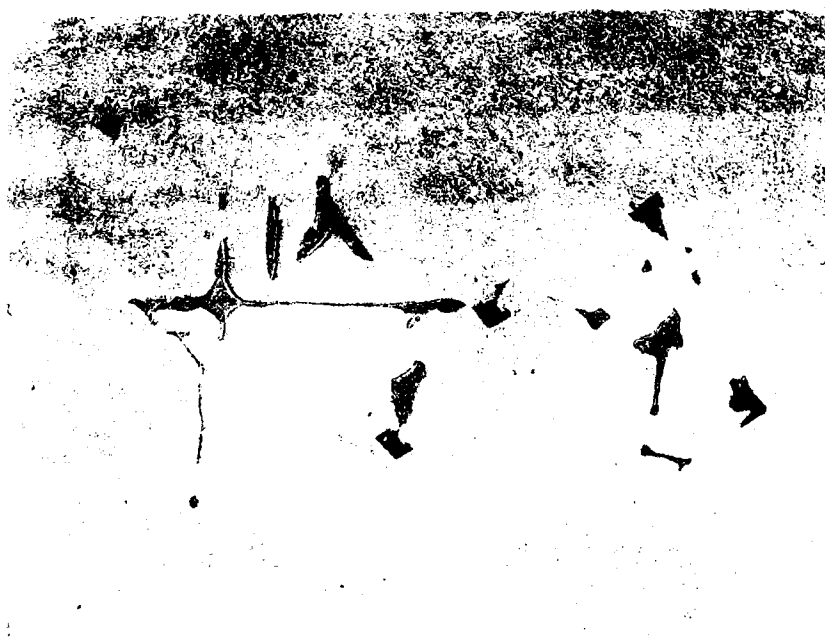


Figure 6.9d: Transverse view at mid-airfoil. Vendor B, second blade, 500X.



Figure 6.10a: Longitudinal view near platform, etched.
Vendor B, second blade, 100X.

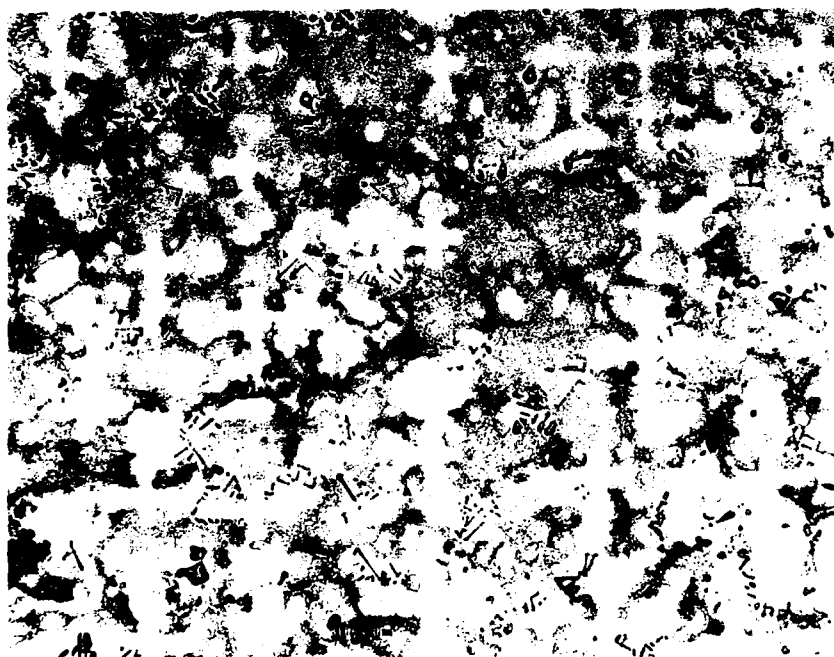


Figure 6.10b: Transverse view through root. Vendor B,
second blade, 100X.



Figure 6.10c: Transverse view near top of airfoil. Vendor B, second blade, 100X.

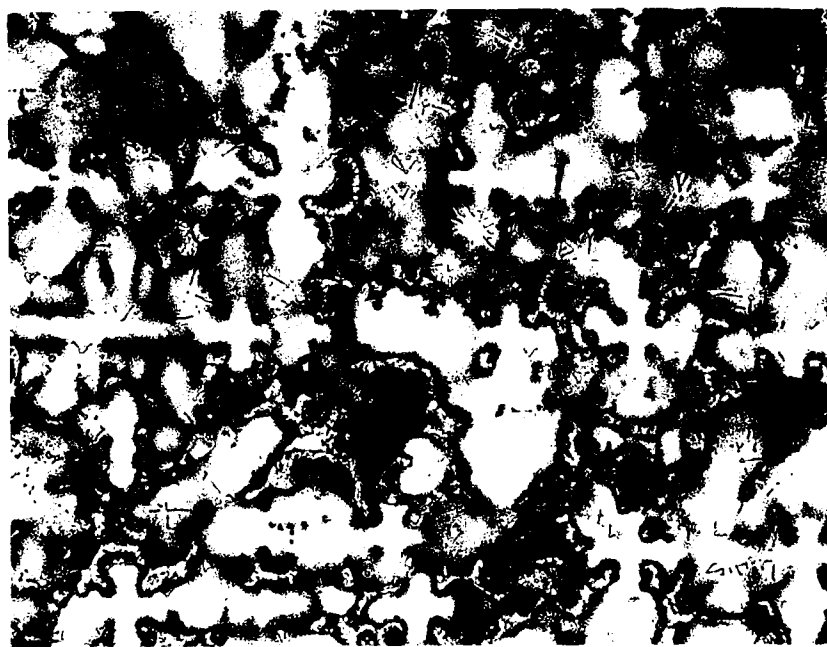


Figure 6.10d: Transverse view at mid-airfoil. Vendor B, second blade, 100X.

7.0 General Discussion and Recommendations

7.1 General

The main objective of this program has been to understand the basis for microstructural variability in directionally solidified hardware cast from hafnium modified MAR-M200 alloy. Particular attention has been paid to evaluating the influence of cooling rate on microsegregation and the influence of interdendritic fluid flow on macrosegregation. The fundamental microstructural parameters studied were volume fraction eutectic, carbide size and shape, and dendrite spacing. The casting parameters varied were cooling rate, thermal gradient, growth rate, transients in cooling rate, and transients in geometry. The only alloy parameter varied was hafnium content.

The main factor that leads to microstructural variability in D. S. castings of hafnium modified MAR-M200 is macrosegregation resulting from transients in interdendritic fluid flow brought about by abrupt changes in geometry and/or thermal conditions.

Beyond this finding, in response to the main objective of the program, substantial delineation and documentation was obtained on the relation between solidification microstructure and casting conditions. These results are presented in detail in Sections 2.0-6.0 and are summarized here. The microstructural results are correlated with the normal range of commercial casting operating parameters in several figures within this section. These figures may be considered process-structure maps. (Noting the often documented relations between structure and properties - not investigated in this program, it is suggested the relations could be expanded from process-structure maps to process-properties maps.) Based on the process-structure maps recommendations are made for targetting current D.S. casting operating parameters and for placing emphasis in future process developments for hafnium modified nickel base alloys.

The axes selected for process-structure maps are log thermal gradient ($^{\circ}\text{C}/\text{cm}$) versus log growth rate (cm/hr) as in Figure 7.1. Obviously, processing conditions near the top of the map represent higher thermal gradients and conditions near the right of the map represent higher growth rates. Processing conditions that fall along a line of slope positive one represent a constant ratio of thermal gradient to growth rate. As example, lines (dash-dot) of constant G/R are drawn for ratios of 100, 10, and $1^{\circ}\text{C hr}/\text{cm}^2$. Processing conditions that fall along a line of slope of negative one represent a constant cooling rate. This can be seen by referring to the approximate relation between cooling rate, thermal gradient, and growth rate (note equation 1-2) which is repeated below.

$$\varepsilon = G \cdot R \quad (7-1)$$

and which may be rewritten in terms of logarithms

$$\log G = \log \epsilon - \log R \quad (7-2)$$

Lines of slope -1 close to the origin would represent slower cooling rates. Lines of slope -1 far from the origin would represent high cooling rates. As example, lines (dashed) are drawn for cooling rates of 40, 400, 4,000 and 40,000 °C/hr. As a frame of reference, the processing conditions within the cross hatched box represent the range of operation of current commercial practice for directional solidification of complex hardware.

The casting parameters employed in the experimental work of this program are compared to the normal range of commercial D.S. operation in Figure 7.2. Five boxes are drawn on the same axes used in Figure 7.1, i.e., $\log G$ vs. $\log R$. The lowest box represents the range of thermal conditions in the interrupted solidification and differential thermal analysis experiments (Task I). The largest box represents the range of thermal conditions for controlled unidirectional solidification of rods in the liquid metal cooling apparatus (Task II). The box most distant from the origin represents the range of solidification conditions in the thin plate chill castings (Task III). The small intermediate box represents the range of thermal conditions in the casting with an abrupt change in cross section directionally solidified to observe macrosegregation effects (Task IV). The remaining box indicates, as in Figure 7.1, the range of operation of current commercial practice for directional solidification of complex hardware.

The laboratory results, as intended, cover a much broader range of operating conditions than present commercial practice. This was useful in determining limits of behavior of these superalloys in D.S. practice. Also, the results over this extended range afford guidelines for emphases in process development if the range of commercial practice is to be expanded.

7.2 Processing - Microstructure Relations

7.2.1 Carbide Morphology

The observations of carbide morphology in the controlled unidirectionally solidified rods (note Figures 3.7-3.12) indicate that MC carbides form from the melt with a script (dendritic) morphology for low G/R ratios and with a blocky, faceted morphology for higher G/R ratios. The boundary between script and blocky carbides was arbitrarily drawn for $G/R = 10^\circ\text{C hr/cm}^2$ in Figure 3.12. However, the spread of the data points would support a boundary between script and blocky carbides to be within the band $4^\circ\text{C hr/cm}^2 < G/R < 12^\circ\text{C hr/cm}^2$. Considering the appearance of both particulate or blocky and script carbides in both the chill plate castings (Task III) and directionally solidified macrosegregation tests (Task IV), it is more likely that the boundary is in the lower end of the range.

Observation of the interrupted solidification samples (Task I) leads to an additional mechanism for blocky carbide formation. Script carbides form directly from the melt and then, due to their high surface to volume ratio, begin to coarsen into more compact forms. Blocky carbides that form in this way have a more open structure than those that form a blocky morphology directly from the melt. This coarsening process would occur at low cooling rates at G/R ratios that are below the value required to form blocky carbides directly from the melt.

The interrupted solidification studies indicate for these particular nickel base alloys the γ dendrites begin to form prior to the first formation of carbides. The MC carbides form within the first 40-50 percent solid. Observation of samples from other tasks are consistent with these observations. However, in the interrupted solidification experiments there was some undercooling (delay in nucleation) of the carbides, a phenomenon that would not be typical of directionally solidified alloys.*

In complex castings, substrates for growth of carbides would be readily available and the MC carbide would begin to form at a lower percent solid. Blocky and particulate carbides, once formed are pushed by the thickening γ dendrite arms into the last regions to freeze, the interdendritic regions. Script carbides are less likely to be pushed and may be found near dendrite centers.

Based on these somewhat arbitrary criteria, the process structure map for carbide morphology near the commercial range of practice is shown in Figure 7.3. From the standpoint of reported experience on the relation between carbide morphology and properties, fine blocky MC carbides are most desirable; and coarse script carbides are least desirable. It would appear that Vendors A and B (Section 6.0) operated their D.S. process in region II forming coarse blocky carbides. Vendor C operated near the arbitrary border between regions III and IV forming moderately coarse script carbides. It would be more desirable to target process development so that new casting operations would operate in region I forming fine blocky carbides.

7.2.2 Dendrite Arm Spacing

The secondary dendrite arm spacing of the unidirectionally solidified rods (Task II) were plotted versus cooling rate on a log-log axes in Figure 3.24. The data fit a line of slope 1/3 as reproduced in Figure 7.4. Within the normal range of commercial casting operation, Figure 7.4 and the expression that follows,

$$S_2 (\mu\text{m}) = 625 \epsilon^{-1/3} (^\circ\text{C/hr}) \quad (7-3a)$$

$$\log S_2 = 2.896 - 1/3 \log \epsilon \quad (7-3b)$$

$$\epsilon = (625/S_2)^3 \quad (7-3c)$$

*Particulate carbides in the chill plate castings may be the result of even greater undercooling, however, this has not been verified directly.

may be used to estimate the relation between secondary dendrite arm spacing and cooling rate in MAR-M200 and hafnium modified MAR-M200 alloys.

The line plotted in Figure 7.4 may be converted to secondary dendrite arm spacing versus local solidification time as in Figure 7.5. The band about the line represents both the spread of the data and the uncertainty in the conversion from local cooling rate to local solidification time. It is believed that local solidification time has a more direct influence on measured secondary dendrite arm spacings than does cooling rate(1). The data from the slowly cooled D.T.A. and interrupted solidification experiments (Task I) are included in Figure 7.5 as triangular points. The data from the non-directionally and slowly cooled samples (square points in Figure 7.5) overlap with the data collected on the unidirectionally solidified samples.

Data on the secondary dendrite arm spacings for the chill cast samples (Task III) have been included on the plot in an approximate fashion. Difficulty arises since neither cooling rates nor local solidification times were measured directly. We have approximated the freezing times of the chill plate castings by assuming the heat removal rate from the alloy to the mold is controlled by interface resistance and that the heat transfer coefficients experienced in these experiments with Ni-base superalloys were the same as with the aluminum alloys used by Bower and Flemings(2). Then, the ratio of freezing times for plates of the same thickness would be

$$\frac{t_f^{Ni}}{t_f^{Al}} = \frac{\rho^{Ni} H_f^{Ni} (T_L^{Al} - T_o)}{\rho^{Al} H_f^{Al} (T_L^{Ni} - T_o)} \quad (7-4)$$

$$= \frac{(8.9)(7.4)(600)}{(2.7)(95)(1400)} = 1.1$$

where ρ is density, H_f is heat of fusion, T_L is liquidus temperature, and T_o is chill plate temperature. The estimate of equation (7-4) indicates freezing times would be about the same for nickel and aluminum chill plate castings of the same thickness. The freezing times of Bower and Flemings(2) were used. The data does not fall on the extrapolation of the line obtained for more slowly cooled samples. This discrepancy may be because we have underestimated the cooling rates of the chill plate castings or because the actual relation between secondary dendrite arm spacing and local solidification time has a power dependence greater than 0.33. For comparison a line of slope 0.35 is drawn in Figure 7.5 and is seen to fit all the data at least as well as the original line of slope 0.33.

Next consider the airfoil castings examined for Task V. The primary and secondary dendrite arm spacings are given for selected locations for each vendor/blade combination in Table 6.2. Using equation

(7-3) the secondary dendrite arm spacings were used to estimate local cooling rates and the estimates are inserted under ϵ_2 in Table 7.1. Similarly, the relation between primary dendrite arm spacing and local cooling rate (note Figure 3.17) may be written

$$\epsilon = (2565/S_1)^3 \quad (7-5)$$

Using equation (7-5) cooling rates based on primary dendrite arm spacings were estimated and inserted in Table 7.1 under ϵ_1 . The agreement between cooling rates estimated from secondaries and primaries is only fair. Secondary dendrite arm spacings probably provide the more reliable estimate. Note, however, the overall decrease in cooling rate in going from root to airfoil, corresponding with the use of root-down part orientation during casting.

The cooling rates for these blades are plotted in Figure 7.6. This data confirms the regions of thermal operation for the three vendors as first estimated from carbide morphology.

The ratios of primary dendrite arm spacing to secondary arm spacing, locally, falls in a band from 3-5. Data from unidirectionally solidified bars and airfoil castings are plotted in Figure 7.7. The wide variation in this ratio may be due to dependence of secondary arms primarily on local solidification time, which is the combined product of G and R , while the primary spacings depend, individually on G and R with different power dependencies.

7.2.3 Percent of Eutectic Constituent

The samples produced in each phase of the project showed a wide range of eutectic constituent, which is consistent with the microstructural variability observed in commercial airfoils that was a main motive for this work. Of course, the eutectic constituent is expected to depend on hafnium content. However, referring back to Figure 3.30 where eutectic percent is plotted versus hafnium content, there is a wide variation especially at higher hafnium contents. This variation may be explained, based on the results of Task IV, as macrosegregation. The rods (Task II) were solidified first at one rate and then at a second rate. Acceleration or deceleration of the freezing isotherms has an influence similar to a change in cross section(3). Similarly, from the results of Task IV the effect of macrosegregation will be greater for higher hafnium contents. Reanalyzing the data of Figure 3.30 in light of the influence of macrosegregation, Figure 7.8 plots the percent eutectic constituent expected as a function of hafnium content in the range of current commercial practice.

Cooling rate, in addition to hafnium content and macrosegregation effects, will effect eutectic content. Note that for the same hafnium content the slowly cooled samples (Task II) and the chill cast samples (Task III) generally contained less eutectic constituent than the unidirectionally solidified rods(4). These data are typified by Figure

7.9. At slow cooling rates additional diffusion in the solid reduces microsegregation and, thus, results in a decrease in eutectic constituent. At higher cooling rates, undercooling due to delayed nucleation and/or curvature at dendrite tips leads to the incorporation of more solute in the primary dendrites and, thus, less eutectic constituent.

In the normal range of commercial practice cooling rate, in itself, is not expected to have an influence on the amount of eutectic constituent. However, abrupt changes in cooling rate or cross section will lead to macrosegregation and a resultant variation in amount of eutectic constituent. If macrosegregation is avoided 1.25-1.5% Hf should be sufficient to provide 8-10% eutectic constituent ($\gamma + \gamma'$) in the matrix.

It is noted that alloys that freeze over a wide range, as do the nickel base superalloys studied here, and that form a small amount of eutectic constituent have a high tendency for hot tearing(1). Thus, it would be expected, as observed in practice, that unmodified MAR-M200 would have a higher tendency for hot tearing than the hafnium modified alloys.

7.3 Recommendations

The studies of this project bear on the relation between thermal parameters during casting and casting microstructure (including segregation) in MAR-M200 with and without Hf modification. In order to make recommendations on processing, assumptions must be made on the relation between microstructure and properties. The following relations are assumed but not demonstrated:

(a) Fine dendrites are desired to give short diffusion distances for the homogenization of the dendrites. This would lead to greater and more uniform γ' precipitation, which would result in better creep resistance.

(b) Fine, blocky carbides are most desirable and coarse, script carbides are least desirable. The carbides are necessary to pin grain boundaries against high temperature sliding but also act as stress raisers in thermal fatigue. Script carbides, having sharper contours, are more detrimental stress raisers.

(c) A uniform distribution $\gamma' + \gamma$ eutectic microconstituent is desirable and the volume percent of eutectic should be about 9-12%. Too low a level of γ' will lead to poor transverse ductility in service and to a high tendency for hot tearing during casting. Too high a level of $\gamma + \gamma'$ eutectic would be detrimental to creep resistance.

(d) Macrosegregation as the result of freckling, healing of hot tears, or flow of solute enriched liquid to feed solidification shrinkage is not desirable as it will cause local regions of weakness.

In order to produce fine dendrites and fine carbides, high cooling rates are desired, thus the product of G and R should be maximized. In line with other requirements the objective for development would be to develop processing methods capable of high thermal gradients.

In order to form primarily blocky carbides the ratio G/R should be kept above 4°C hr/cm^2 . Thus, an attempt to increase growth rates should be balanced by an increase in thermal gradient.

In order to form 8-12% $\gamma + \gamma'$ eutectic, about 1.25-1.5% hafnium should be used to modify the MAR-M200 and macrosegregation should be avoided. Abrupt changes in growth rate should be avoided. Abrupt changes in geometry should be compensated for by insuring proper thermal conditions and directionality as the freezing isotherms pass the region of change in cross section. Freckling should be avoided by proper selection of thermal parameters(5).

Region I in Figure 7.3 would be the preferred region of operation for D.S. casting processes and Region II would be the second selection. Based, in addition, on the desire to avoid freckle formation, the thermal parameters in Table 7.2 are given as (a) minimums desired for current practice and (b) targets for process development.

7.4 References

1. M.C. Flemings, Solidification Processing, Chapter 5 (New York: McGraw Hill, 1974).
2. T.F. Bower and M.C. Flemings, "Formation of Chill Zone in Ingot Solidification," Trans. TMS-AIME, 239 (1967) 216-220.
3. G.E. Nereo and M.C. Flemings, "Macrosegregation, Part I," Trans. TMS-AIME, 242 (1968) 41-49.
4. R. Sellamuthu, "Analysis and Measurement of Segregation in Directionally Solidified Nickel Base Superalloy," Ph.D. Thesis, Metallurgical Engineering, University of Pittsburgh, 1979.
5. S.M. Copley, A.F. Giamei, S.M. Johnson, and M.G. Hornbecker, "The Origin of Freckles in Unidirectionally Solidified Castings," Met. Trans., 1 (1970) 2193-2204.

Table 7.1 Cast Airfoil Cooling Rates

		FIRST BLADE		SECOND BLADE	
		$(\frac{\epsilon_1}{^\circ\text{C/hr}})$	$(\frac{\epsilon_2}{^\circ\text{C/hr}})$	$(\frac{\epsilon_1}{^\circ\text{C/hr}})$	$(\frac{\epsilon_2}{^\circ\text{C/hr}})$
Vendor A	Root	1580	- -	- -	-
	Trans.	610	534	1080	1640
	A.F.	490	- -	- -	- -
Vendor B	Root	- -	- -	1140	-
	Trans.	- -	- -	900	2350
	A.F.	- -	- -	700	- -
Vendor C	Trans.	2110	3810	- -	- -

* ϵ_1 computed based on measurement of primary dendrite arm spacing and equation (7-5). ϵ_2 computed based on measurement of secondary dendrite arm spacing and equation (7-3).

Table 7.2 Minimum and Target Thermal Parameters for
Industrial Directional Solidification Practice

<u>Type</u>	<u>R(cm/hr)</u>	<u>G($^{\circ}$C/cm)</u>	<u>$\epsilon(^{\circ}$C/hr)</u>
Minimum	17	70	1400
Target	30	120	3600

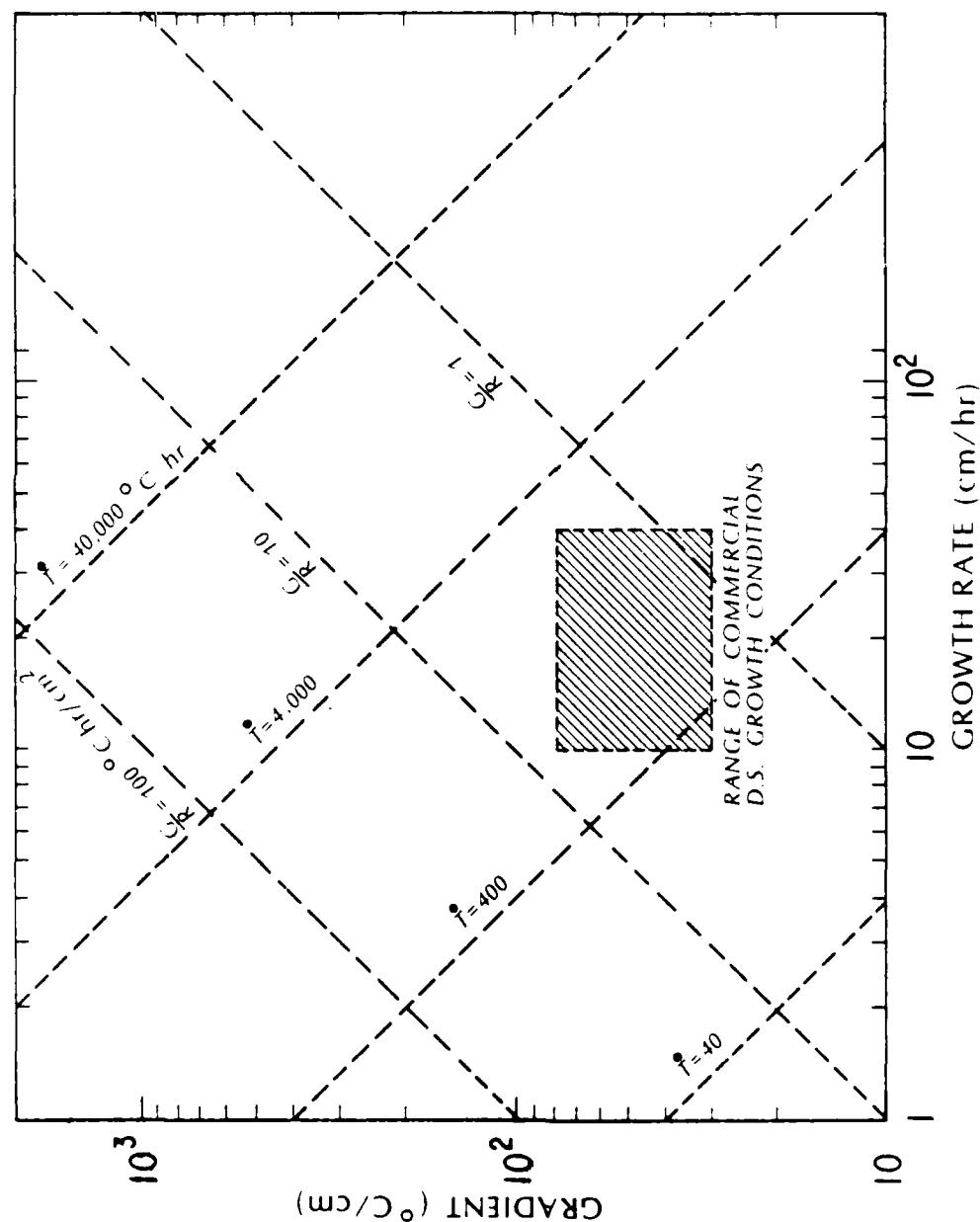


Figure 7.1: Process-structure map illustrating the loci of constant ratio of thermal gradient to growth rate (G/R) and constant cooling rate ($T=\epsilon$). The shaded area represents the range of current commercial directional solidification practice.

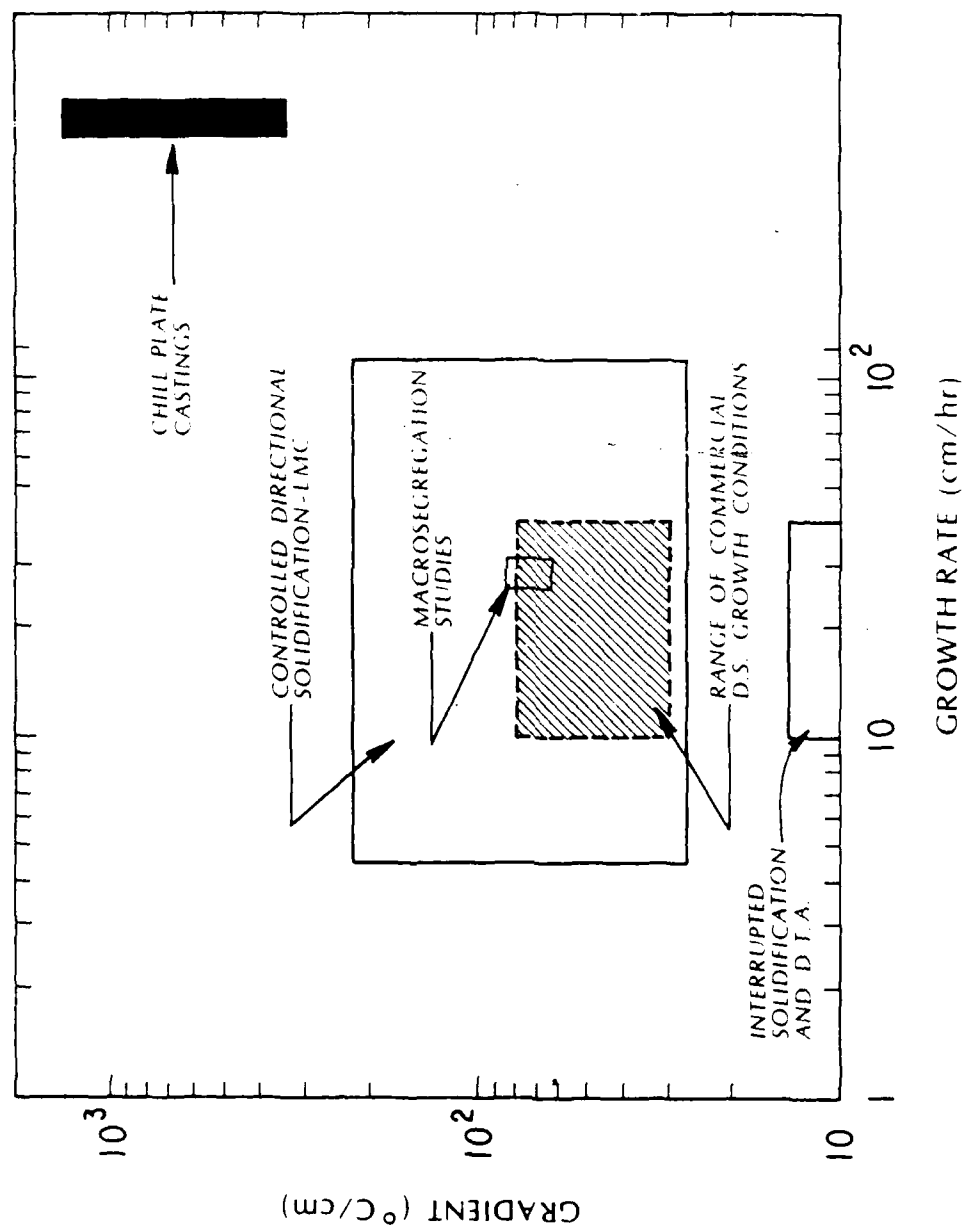


Figure 7.2: Process-structure map illustrating the thermal parameters associated with the four types of experiments employed in this study.

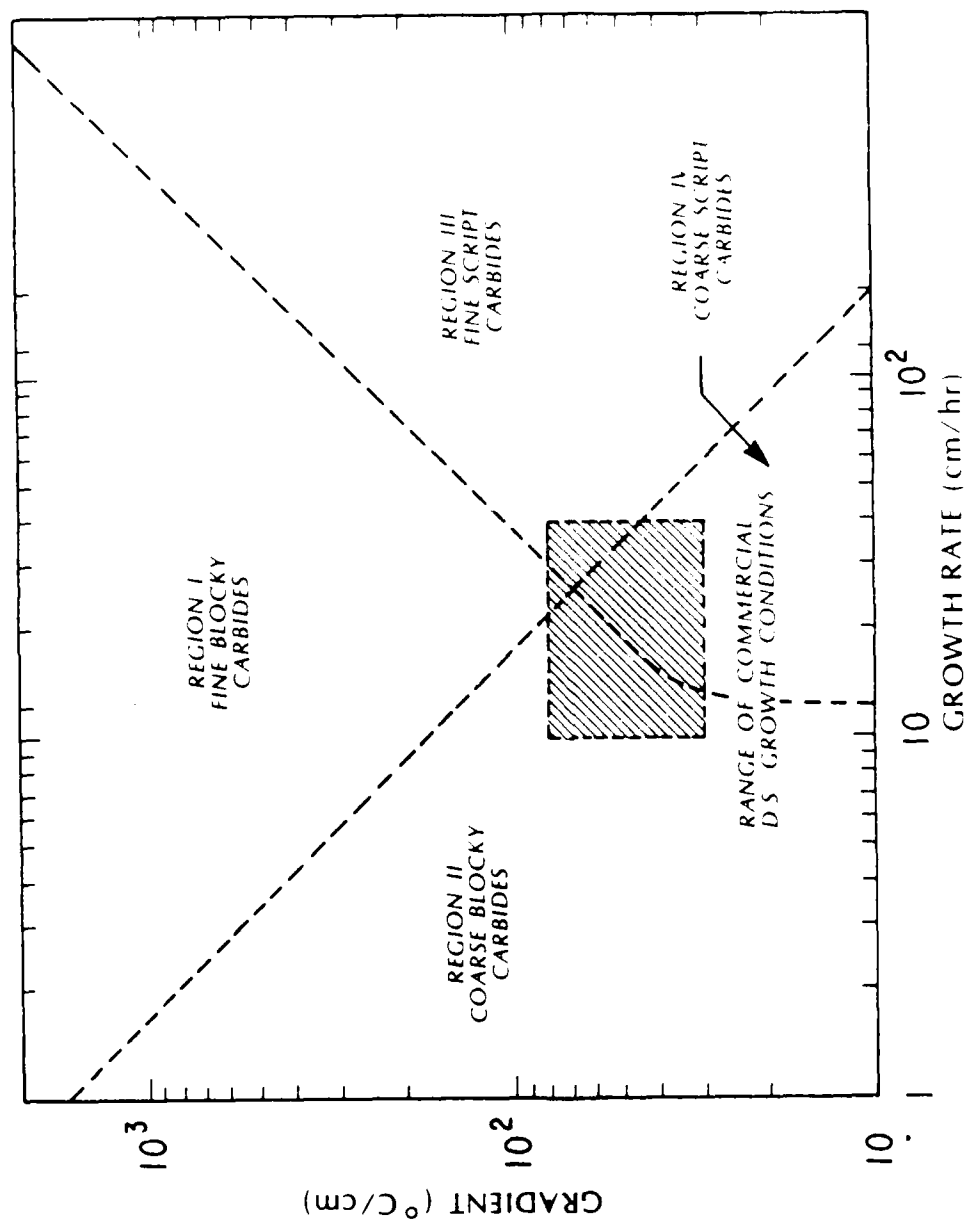


Figure 7.3: Process-structure map illustrating relation between thermal processing parameters and morphology of carbides formed during freezing.

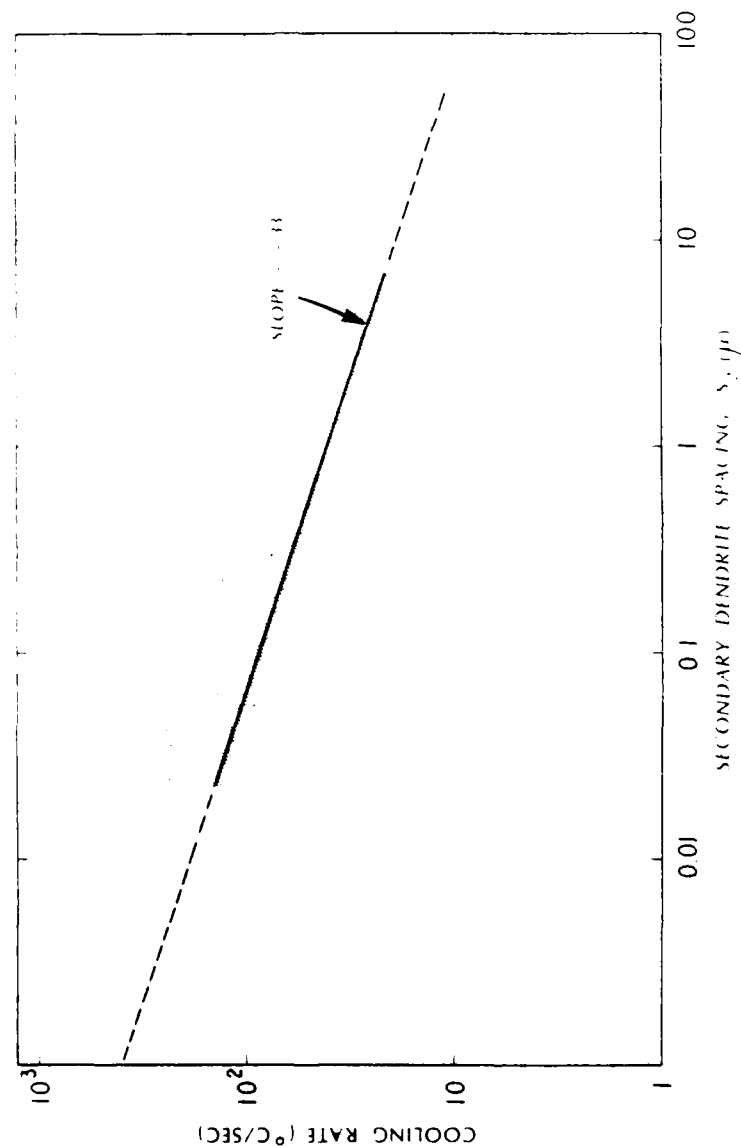


Figure 7.4: Log of secondary dendrite arm spacing versus log of cooling rate for unidirectionally solidified Mar-M200 and hafnium modified Mar-M200 nickel base superalloy.

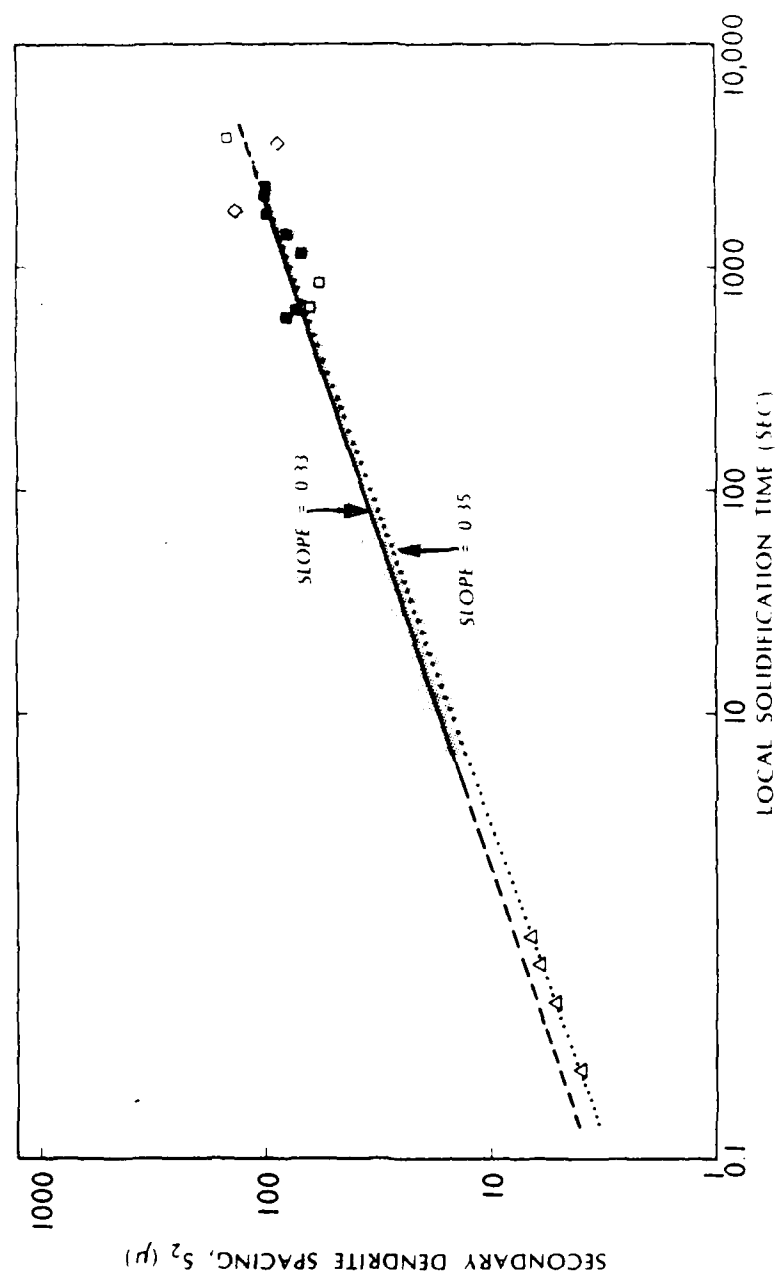


Figure 7.5: Log of secondary dendrite arm spacing versus log of local solidification time for Mar-M200 and hafnium modified Mar-M200 nickel base alloy.

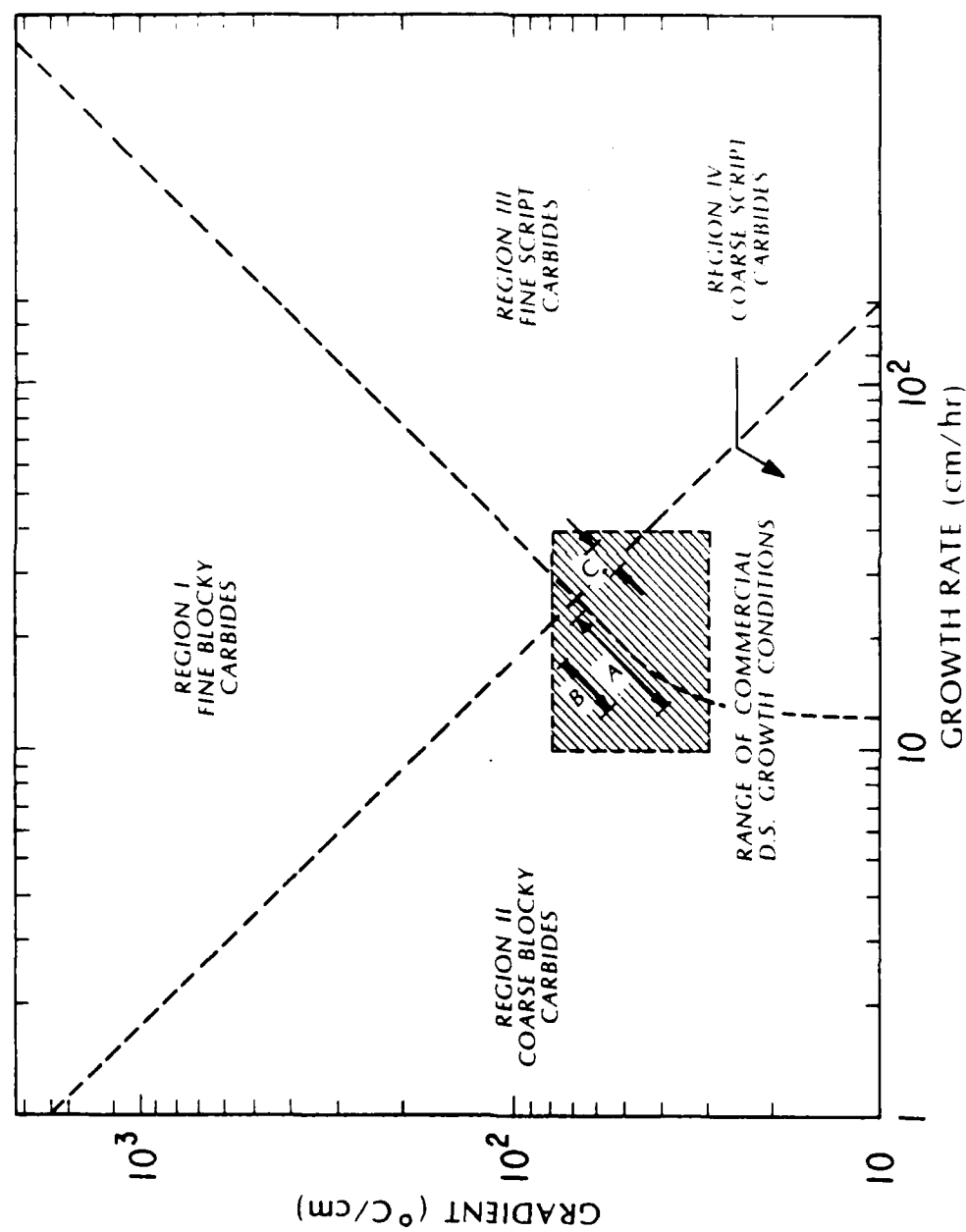


Figure 7.6: Process-property map illustrating the range of thermal parameters employed by vendors A, B, and C in processing airfoil castings examined in this study.

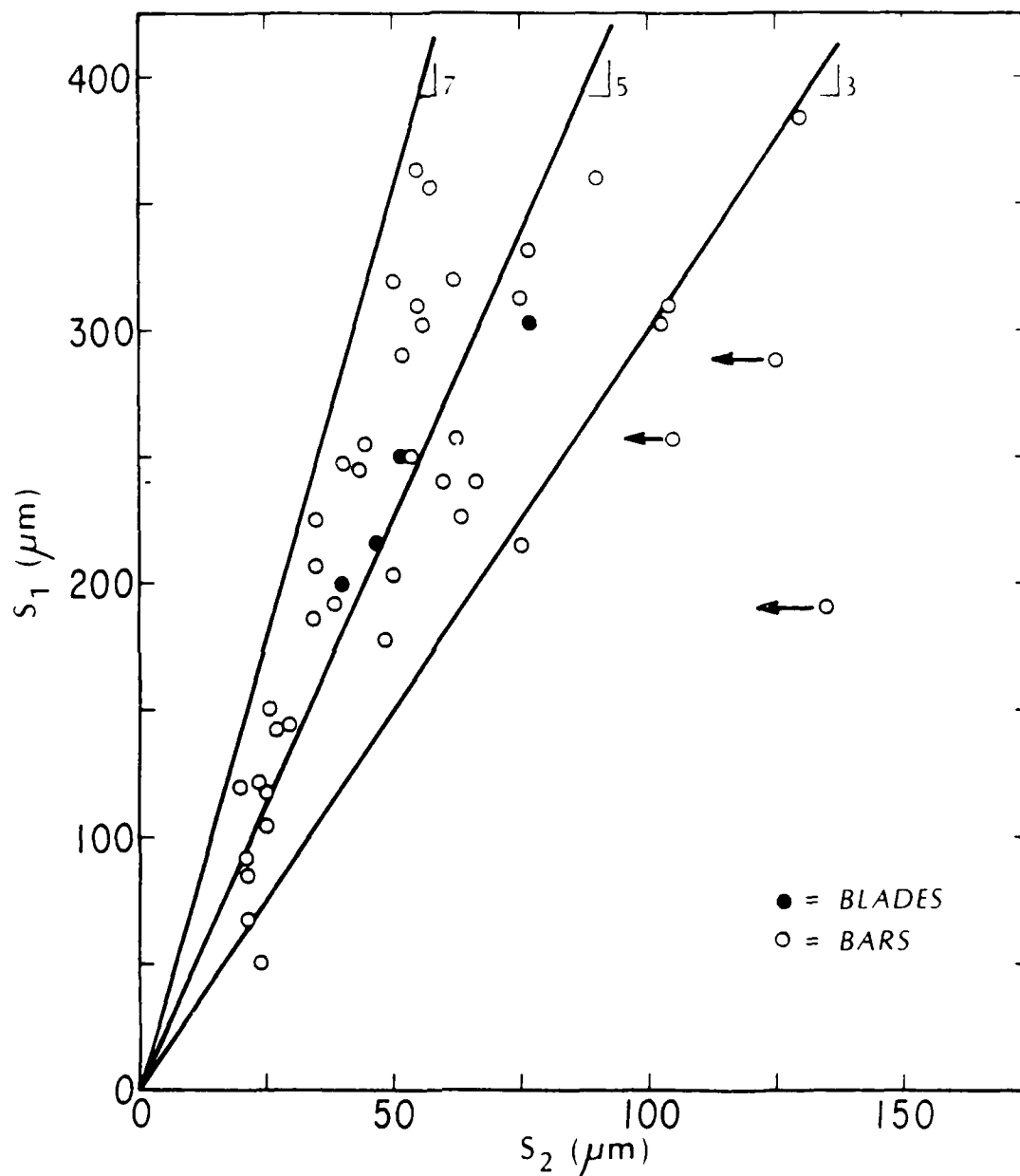


Figure 7.7: Relation between primary and secondary dendrite spacings for directionally solidified MAR-M200 with and without hafnium additions. Open circles are data from laboratory samples (Task II) and closed circles are data from air-foil castings.

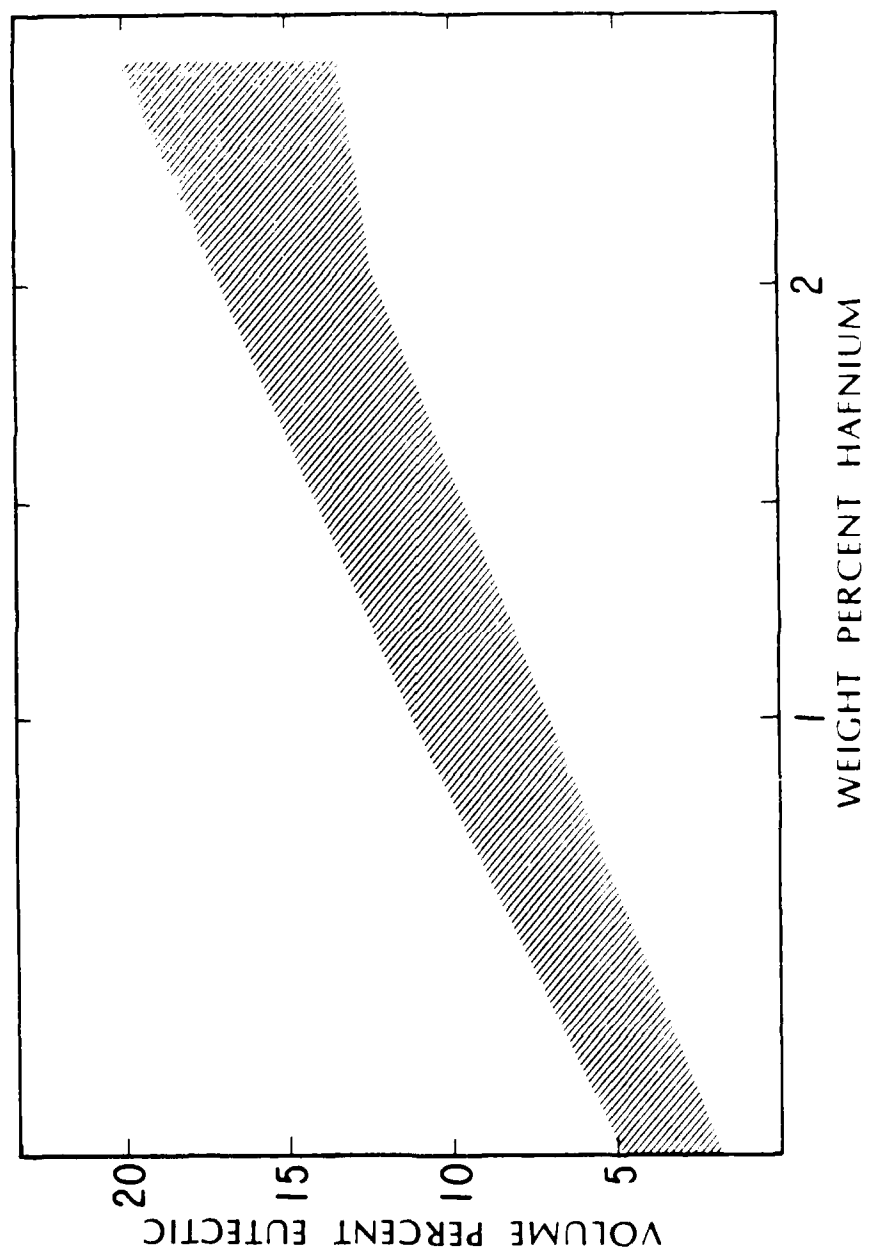


Figure 7.8: Volume percent eutectic versus percent hafnium addition to Mar-M200 measured in the range of normal commercial D.S. casting practice and in the absence of macro-segregation.

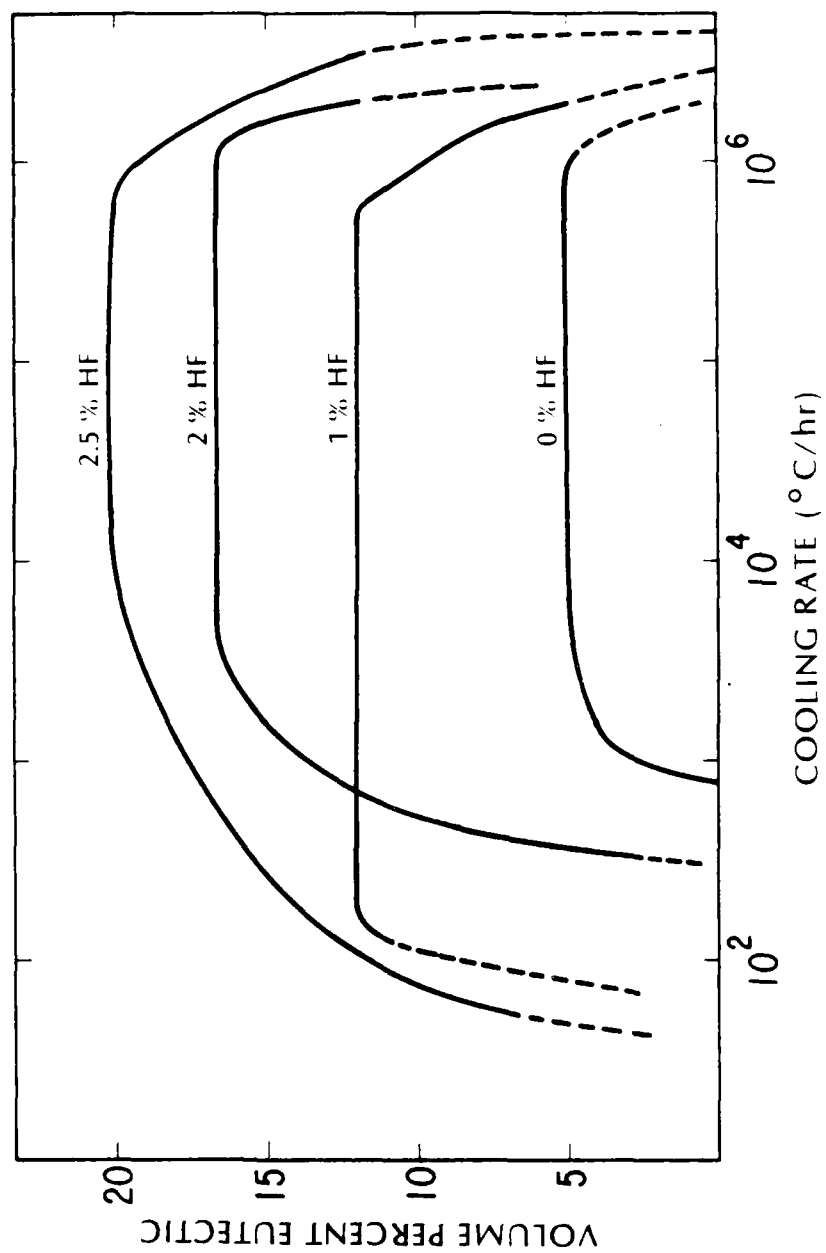


Figure 7.9: Volume percent eutectic versus log cooling rate in the absence of macrosegregation, for Mar-200 alloy + 0, 1, 2, and 2.5% Hf.

END

DATE

FILMED

DTIC

July 88